The Pennsylvania State University
The Graduate School

EMERGENT QUANTIZATION IN INTERACTING THOULESS PUMPS

A Dissertation in
Physics
by
Marius Jürgensen

Submitted in Partial Fulfillment
of the Requirements
for the Degree of

Doctor of Philosophy

May 2024

The dissertation of Marius Jürgensen was reviewed and approved by the following:

Mikael C. Rechtsman
Downsbrough Early Career Development Professor of Physics
Dissertation Advisor
Chair of Committee

Chaoxing Liu
Professor of Physics

Jorge Sofo
Professor of Physics
Professor of Materials Science and Engineering

Xingjie Ni
Associate Professor of Electrical Engineering

Mauricio Terrones
Evan Pugh University Professor
Professor of Chemistry and Materials Science and Engineering
George A. and Margaret M. Downsbrough Department Head

Abstract

Topology has revolutionized our understanding of physics: physical observables are fully defined – up to natural constants – by topological invariants and thus independent of the exact details of the device. As a general wave phenomena, topological protection has found its way into many fields of physics, including photonics, that could profit tremendously from topologically protected transport of photons given that photons are the main information carriers in today's communication infrastructure and projected to be an integral part of next-generation on-chip computation and quantum information devices. While non-interacting/linear topological photonics has been well understood, less is known in the presence of inter-particle interactions. In optics and at high optical power, interactions between photons are mediated by an underlying medium and described in the mean-field limit via Kerr nonlinearities, with spectacular consequences, amongst others: generation of entangled photon pairs, frequency combs, and solitons, the latter being self-forming, localized nonlinear eigenstates.

This dissertation pioneers the field of topologically quantized transport in interacting/nonlinear Thouless pumps – 1+1 dimensional reduced versions of the integer quantum Hall effect, where one wavevector dimension is replaced with a periodic modulation as a synthetic dimension. We show theoretically and experimentally that nonlinearity can act to quantize transport via soliton formation in Thouless pumps and the emergence of a rich plateaux structure with integer as well as fractionally quantized transport, despite a non-uniform band projection required for linear Thouless pumps. Quantization occurs as the soliton solutions at the beginning and end of each cycle are identical – apart from translation invariance. By expanding the discrete nonlinear Schrödinger equation into Wannier states, we show analytically that the center of mass of a low-power soliton, and therefore its trajectory, tracks the position of Wannier states, that are dictated by the Chern number. Using evanescently coupled waveguides, we observe integer quantized soliton transport by one unit cell, with a nonlinear phase transition to a trapped soliton at higher power due to spontaneous symmetry breaking nonlinear bifurcations. In a separate experiment and at intermediate power, we observe fractionally quantized soliton Thouless pumping with a fraction of -1/2 after one period and integer quantization of -1 after two periods, as the soliton follows the trajectory of maximally-localized multi-band Wannier states. Furthermore, we theoretically describe fractional Thouless pumping in fermionic few-particle systems with integer filling and strong repulsive interactions, when every second multi-band Wannier is occupied. Using exact diagonalization and density matrix renormalization group calculations we confirm that small systems have a degenerate ground state manifold separated from higher bands and support average

pumping of 1/2 particles per period at intermediate adiabaticity. Finally, we present experimental advances in the fabrication of deep-etched two-dimensional photonic crystals in doped crystalline YAG and demonstrate the ability to fabricate large arrays with sub-micrometer lattice constants and deterministically varying etching depth.

Table of Contents

List of Figures

List of Tables

Acknowledgments

First and foremost, I would like to express my gratitude to my advisor and academic parent, Prof. Mikael C. Rechtsman. In a nutshell, I came to Penn State because of him, learned the art of physics because of him, and enjoyed my entire time at Penn State because of him. I could not have wished for a better mentor, and this thesis is based on everything I learned under his advisory. I have truly enjoyed my entire journey with him, beginning with our first meeting, discussing if I start on a theory or experimental project, until the end of my graduate studies when he gave me complete freedom to balance work and personal life. Mikael has inspired me in many ways, most notably through his enthusiasm and contagious joy for physics, his unstoppable motivation to explore new physical ideas, and his insistence to explain physics in simple terms. I am extremely grateful for his trust allowing me to find and explore my own interests.

My research could not have been possible without significant contributions from my collaborators. In particular, I would like to thank the incredibly talented and knowledgeable postdocs who I worked with. I learned the secrets of direct femto-second laser writing and soliton formation from Sebabrata Mukherjee. I immensely profited from discussion with Alexander Cerjan, who took incredibly short time to understand new topics and give insightful feedback. Finally, I deeply enjoyed working with Christina Jörg on nonlinear effects in waveguide arrays, inspiring me with her meticulous attention to experimental details. Furthermore, I would like to thank Gil Refael and Jacob Steiner, with whom I explored the theory world of fractional Thouless pumping in few-particle systems. I would also like to thank Sachin Vaidya, Charles Roques-Carmes, and Simo Pajovic, who I worked with to create volumetrically enhanced scintillation. During his time at Penn State, I had wonderful discussion with Sachin about higher-order topology, fragile phases, and generally brainstorming ideas. Furthermore, I have enjoyed working on waveguide projects with the younger generation of graduate students in my research group, namely Matthew Krebs, Mritunjay Kumar Joshi, Abhijit Chaudhari, and Jiachen Wang. I also owe a lot of gratitude to the other members of my research group for our scientific journey over the years.

The work presented in this dissertation was supported by the Office of Naval Research under the YIP program, Grant No. N00014-18-1-2595; the Packard Foundation under Fellowship No. 2017-66821; the Office of Naval Research (ONR) Multidisciplinary University Research Initiative (MURI) under Grant No. N00014-20-1-2325; the Air Force Research Laboratory (AFOSR) Multidisciplinary University Research Initiative

(MURI) under Grant No. FA9550-22-1-0339; the Verne M. Willaman Distinguished Graduate Fellowship at the Pennsylvania State University. Some numerical calculations were performed on the Pennsylvania State University's Institute for Computational and Data Sciences' Roar supercomputer. Any opinions, findings, and conclusions or recommendations expressed in this dissertation are those of the author and do not necessarily reflect the views of the funding agencies.

Chapter 1
Introduction

Topological protection is a powerful concept. Its first observation was reported by Nobel Laureate von Klitzing and co-workers Dorda and Pepper [3], who measured precisely quantized conductance (in integer multiples of fundamental constants) in two-dimensional electron gases with a perpendicular magnetic field. This effect is known as the integer quantum Hall effect and laid the foundation for the discovery of topological phases of matter in which physical observables are fully defined – up to fundamental constants – by topological invariants and therefore independent of the exact details of the sample. The importance of this finding cannot be overstated: As physical observables are completely independent of the system parameters and topologically protected against small perturbations, devices are possible that are robust against disorder and fabrication imperfections. Perhaps most spectacular, the quantization of conductance in the integer quantum Hall effect is so precise (less than one part in 10^{10}) that it is now incorporated into the international system of units (SI). [4].

Shortly after the discovery of the integer quantum Hall effect, two complementary explanations for the quantization were published. The first explanation was brought forward by Laughlin and is based on a simple but elegant gauge argument [5]. It shows that the conductance has to be quantized upon threading a single flux quantum (that can be gauged away) through the annulus of a Corbino disk. While this explanation is independent of the exact system parameters, it is limited to the very special Corbino disk geometry. The second explanation was brought forward by Thouless, Kohmoto, Nightingale, and den Nijs who used Kubo's formula to calculate the conductance of isolated bands in the bulk of a system with a periodic potential [6]. They found that each band can be associated with an integer number – called the first Chern number – that describes its quantized conductance when fully filled, as is the case for a Fermi level in a bandgap.

Another important milestone was the realization that the observed quantization in the integer quantum Hall effect is more general and does not necessarily need a magnetic field. Instead, a system needs to break time-reversal symmetry, as shown in a discrete model with a staggered flux but net zero magnetic field, which is now known as Haldane model [7]. Furthermore, it was realized that topology is a general wave phenomena and can be observed for fermions as well as bosons [8, 9] in continuous and discrete systems. Experimental observations have been made in numerous two-dimensional platforms, including microwaves [10], acoustics [11], photonic waveguides [12], ring resonators [13], twisted cavities [14], ultracold atoms in optical lattices [15, 16], mechanical pendulum systems [17], exciton-polaritons [18], and electronics [19]. But only few experiments (for example [10]) are direct analogues of the integer quantum Hall effect by breaking time-reversal symmetry using magnetic fields. This is especially prevalent in optics where the magneto-optical response is negligible at visible and telecommunication wavelengths [20]. Instead, a variety of methods to create artificial gauge fields [20, 21] have been developed, amongst others rotation [14, 22, 23], shaking [12, 15], displaced resonators [13], and strain [24–27]. More recently, a further alternative has emerged using a time-periodic modulation of the refractive index [28].

Another particular elegant way to avoid the experimental difficulty of time-reversal symmetry breaking was developed by Thouless, which is known as Thouless pumping [29]. Thouless pumps are dimensional reduced versions of the integer quantum Hall effect, in which one wavevector dimension is replaced by a periodic modulation. Hence they are 1+1 dimensional, with one spatial dimension and an additional synthetic dimension. Using Thouless pumps, significant progress has been made in the understanding of topological protection: In fermionic Thouless pumps it was rigorously shown for the first time that topological protection can be extended to interacting and disordered systems [30]. Later, this proof was extended to the two-dimensional case, laying the basis for the definition of the many-body Chern number [31]. Apart from pioneering the theoretical side, Thouless pumps are also ideal models to study in photonics, where design flexibility allows simple implementations, in particular using coupled waveguides.

While non-interacting/linear topological systems have been well understood, less is known in the presence of inter-particle interactions. Spectacular results are known from condensed matter, where strong interactions lead to the fractional quantum Hall effect [32], known to host quasi-particle excitations with non-Abelian braiding statistics, predicted to be useful for topological quantum computation [33]. That said, the behaviour of interacting bosonic and in particular photonic systems can be very different from the

electronic case. As photons are not charged they do not interact strongly, but at high optical power and in the mean-field limit, interactions between photons are described using nonlinearities. Its interplay with topology has shown first novel results, for example, the generation of entangled photons in edge states [34], nonlinearly-induced edge states in anomalous topological insulators [35], the observation of solitons in the bulk of an anomalous topological insulator executing cyclotron-like rotations [36,37], the observation of nonlinear wave propagation in edge states [38], as well as topologically protected lasing in edge states [39]. As another example, it has been proposed that edge states can be used as a super-ring resonator modes to generate dissipative Kerr solitons more efficiently and with smaller mode spacing [40].

Despite those promising first results, topology in the presence of interactions/nonlinearity is still far from being well understood given the lack of broad theoretical frameworks. Furthermore, many studies have focused on properties of topological edge states and no studies have shown the emergence of quantization, the hall-mark feature of topology, due to nonlinearity. In this dissertation, we study the interplay between topology (and especially topologically protected quantization of transport) and interactions/nonlinearity using Thouless pumps. In particular we will show that nonlinearity can act to quantize transport via soliton motion. The emergent quantization can be integer as well as fractionally quantized, with no counterpart in non-interacting/linear systems. This dissertation is structured as follows:

In Chapter 2, we review the theoretical background necessary to understand this dissertation. First, we introduce Thouless pumps and rederive the formulas for quantization of particle transport. On the way, we define important topological quantities, namely the Berry phase, Berry curvature, and the Chern number. Furthermore, we show the intricate relationship between Thouless pumps and their two-dimensional counterparts of Chern insulators via dimensional reduction, that constitutes a simple way to create Thouless pumping models. Second, we discuss single-band and multi-band Wannier functions and their relation to Thouless pumping. We explicitly show that the winding of the center of mass of Wannier states is equal to the Chern number. Third, we introduce femto-second laser-written waveguide arrays, the main experimental platform used in this dissertation. We discuss their fabrication and introduce the paraxial equation that governs the dynamics of light propagation in waveguide arrays. Finally, we discuss soliton formation at high optical input power and show how most relevant parameters in waveguide systems can be investigated with a single device: a directional coupler.

In Chapter 3, we show experimentally and theoretically the emergence of quantization

in nonlinear Thouless pumps via soliton motion, despite non-uniform band occupations, as necessary for quantization in non-interacting Thouless pumps. Quantization follows from the fact, that the soliton comes back to itself after each period – apart from a translation by an integer number of unit cells due to translation invariance. Using evanescently coupled waveguide arrays, we observe soliton pumping by up to one lattice constant with a subsequent nonlinear phase transition to a trapped soliton via spontaneous symmetry-breaking nonlinear bifurcations. Theoretically, we show that soliton pumping is a general phenomena and we observe that solitons from all bands are pumped by the Chern number of the band from which they bifurcate.

In Chapter 4, we present an analytic proof of this quantization mechanism. By expanding the discrete nonlinear Schrödinger equation into Wannier functions, we show that low-power solitons track the position of the single-band Wannier states of the band from which the solitons bifurcate. Thus, the displacement of a soliton is dictated by the Chern number of the respective band. The transport remains quantized for increasing power, as long as no nonlinear bifurcations destroy the trajectory of the soliton and the soliton stays stable. Furthermore, we find trajectories of unstable solitons that represent mathematical solutions but are experimentally unobservable. We close this chapter by showing quantized diagonal pumping in a two-dimensional Thouless pump.

In Chapter 5, we exploit that our analytic proof is only valid at low power. We theoretically and experimentally show that, at intermediate power and when the strength of the nonlinearity overcomes the band gap, soliton transport in Thouless pumps can be fractionally quantized. This happens, as the soliton follows the maximally-localized multi-band Wannier states that have fractional winding. To experimentally prove this point, we map out the propagation of a soliton in a suitable Thouless pump over two periods. We experimentally observe fractional pumping by -1/2 unit cells after one period and -1 after two periods. Furthermore, we numerically show that in a Thouless pump with more bands, a rich plateaux structure emerges with integer and fractionally quantized plateaux.

In Chapter 6, we theoretically describe fractional Thouless pumping in fermionic few-particle systems with integer filling and strong repulsive interactions. The effect occurs for two energetically close energy bands, when every second multi-band Wannier is occupied, which have fractional winding. Using exact diagonalization and density matrix renormalization group calculations we show that finite systems (up to a maximum system size) have a degenerate ground state manifold separated from higher bands that support average pumping of 1/2 particles per period at intermediate adiabaticity, without

breaking the underlying discrete translation symmetry.

Finally, in Chapter 7, we present experimental advances in the fabrication of deep-etched two-dimensional photonic crystals in doped crystalline YAG. We explore the influence of crucial fabrication parameters, particularly analyzing the impact of the writing power on the etching depth. By controlling the power as a function of writing depth, we demonstrate the ability to fabricate large arrays with sub-micrometer lattice constants and deterministically varying etching depth.

We conclude this dissertation with a summary of the work, outlining its impacts and providing an outlook.

Chapter 2
Theoretical and experimental background

This chapter introduces the theoretical and experimental background knowledge. Firstly, Thouless pumps – the central topological system investigated in this dissertation – are discussed, with emphasis on deriving the equations for the anomalous velocity and quantization of particle transport. Afterwards, we will introduce the Wannier basis, which is central for the theoretical understanding of soliton Thouless pumping. Finally, we introduce coupled waveguide arrays – the main experimental platform used in this dissertation. We discuss the fabrication and experimental properties of waveguides arrays and the formation of spatial solitons at high intensities due to Kerr nonlinearities.

2.1 Thouless pumps

The work in this dissertation is centered around discovering and exploring topological protection and the emergence of quantization in nonlinear optical systems, where the nonlinearity describes the interactions between photons in the mean-field limit. In the following, we will provide a brief theoretical introduction to the topological model used in this dissertation: Thouless pumps. Additional information about Thouless pumps can be found in the review paper in Ref. [41].

2.1.1 Introduction to Thouless pumps

Thouless pumps are spatially periodic, one-dimensional systems, with an additional time-periodic modulation. Often referred to as 1+1 dimensional models (one space and one time/modulation dimension), transport in Thouless pumps – integrated over

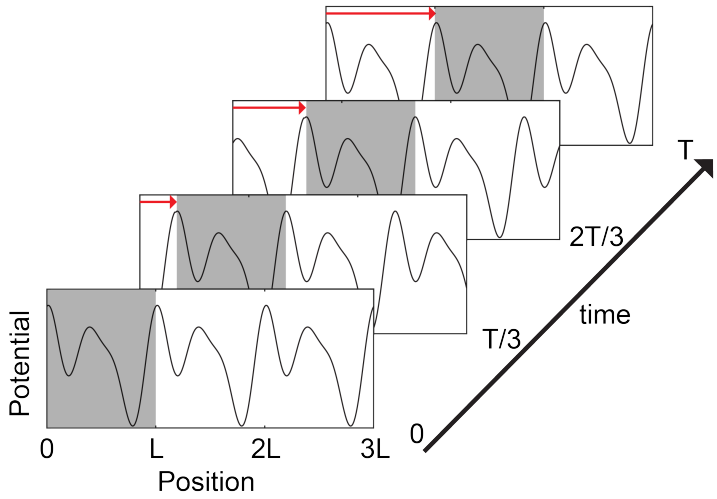

Figure 2.1. Prototypical Thouless pump. A periodic potential landscape (with lattice constant L) is slowly sliding to the right. The system is time-periodic with period T. Gray areas highlight one unit cell. Red arrows show the displacement of the potential at times t=$T/3$, $2T/3$ and T. According to Thouless, particle transport is quantized in an infinite system with adiabatic modulation and filled bands.

one modulation cycle and across a boundary – is integer quantized for infinite systems, adiabatic modulation and full bands [29]. Thouless pumps were introduced by David J. Thouless. By way of example he considered a slowly sliding potential, $V(x,t) = V_0(x) + V_1(x - vt)$, where x denotes the spatial coordinate, v the speed of the sliding potential and t time (see Fig. 2.1). In this setting, the potential is also periodic in time as the system comes back to itself after a period $T = v/a$, where a is the lattice constant. Thouless showed that the integrated current over one period can vary continuously in a torus, but is integer quantized (in multiples of the lattice constant) in an infinite periodic system with filled bands when the adiabatic theorem applies. Under these conditions, transport is topologically protected and does not depend on the exact details of the potential or the modulation. This makes Thouless pumps formidable topological models to study the topological protection of transport.

Furthermore, Thouless pumps have a deep connection with the integer quantum Hall effect, and the quantization of particle transport in Thouless pumps directly relates to the quantized conductance in the integer quantum Hall effect. When the time/modulation dimension is replaced with a second wavevector dimension, quantization is described mathematically identically and by the same topological invariant, the Chern number. We will make use of this connection in Chapter 2.1.3 to derive a specific example of a Thouless pump via dimensional reduction. In contrast to two-dimensional Chern insulators and their continuous counterpart the integer quantum Hall effect, Thouless pumps do not

need to explicitly break time-reversal symmetry using gauge fields; instead, it is in-built into the modulation. This facilitates implementations in photonics due to the design flexibility available in fabricated structures (see also Chapter 2.3.1) to realize arbitrary modulations but stands in the way of condensed matter implementations, where it is a challenge to precisely engineer time-dependent Hamiltonians.

Originally developed for electronic systems, it has been realized that topological protection and therefore also Thouless pumping is a general wave phenomena. Indeed, experimentally, Thouless pumps are mostly studied in bosonic platforms. To observe quantization, bosonic systems must mimic their electronic counterpart with a uniform band occupation, typically achieved by exciting the system with a localized Wannier state (see Chapter 2.2 for an introduction to Wannier states) that by definition has a uniform band projection. Alternatively, Bloch oscillations [42] have been used or coupling to a bath has been proposed [43]. In photonics, the first observation of Thouless pumping was reported in a quasi-periodic array of evanescently coupled waveguides [44] with end state to end state pumping. Since then, Thouless pumping has also been observed in ultracold atoms in optical lattices with effectively hard-core bosons [45] and fermions [46]. To name a few more works, dissipative Thouless pumps have been studied in Ref. [47] and building upon their synthetic dimension, Thouless pumps have also been used to simulate properties of the four-dimensional quantum Hall effect [48, 49]. A recent review on Thouless pumps can be found in Ref. [41].

On the theory side, Thouless pumps have had tremendous success explaining topological behavior in the presence of disorder and interactions. It was first shown for fermionic Thouless pumps that topological protection persists even in the case of many-body interactions and substrate disorder, as long as the bandgap stays open [30]. The proof was later generalized to two-dimensional systems [31] and led to the introduction of the many-body Chern number (a generalized version of the Chern number), which is calculated using twisted boundary conditions. In a numerical study it has been shown that for large systems the calculation can be reduced to a single boundary condition as the the bulk behavior is boundary independent [50]. For bosons, robustness against disorder has been studied experimentally in coupled waveguide arrays [51]. For interacting bosonic systems less is known. Amongst others, it has been predicted that few attractively interacting particles can show pumping [52, 53] and that repulsive bosons show integer quantized pumping, as long as the superfluid phase is avoided [54]. Disordered fermionic Thouless pumps have been studied in Ref. [55] and the effect of interactions on quantization in Ref. [56].

2.1.2 Adiabatic evolution, Berry phase and quantization of pumping

In this section, we derive the quantization of particle transport in Thouless pumps as originally shown in Ref. [29]. Further information can be found in Refs. [57, 58]. Along the way we introduce important concepts of topological physics, namely the Berry phase, the Berry curvature, and the Chern number.

Suppose a system is described by a Hamiltonian $\hat{H}(R)$ that depends on some arbitrary parameter $R(t)$ that is slowly (and we will later define what slowly means) modulated in time. Our aim is to calculate the particle transport induced by this modulation. As we will see in Chapter 2.3, for coupled waveguide arrays, time t has to be replaced with the propagation distance z, but the physics remains the same. We revert here to using time t, as this is the stereotypical case the reader would see the derivation also elsewhere. Instead of staying completely general, we assume the system is a Thouless pump, that is spatially one-dimensional with translation symmetry and we work in the wavevector representation using $\hat{H}_k(R)$, where k is the Bloch wavevector. At each point in time t, the instantaneous eigenstates $|u_{\alpha,k}(t)\rangle$ with eigenenergy $E_{\alpha,k}(t)$ are given by:

$$\hat{H}_k(R(t))|u_{\alpha,k}(t)\rangle = E_{\alpha,k}(t)|u_{\alpha,k}(t)\rangle. \tag{2.1}$$

Here, we have introduced another quantum number, α, that denotes the band index (and possibly other relevant quantum numbers) as known from condensed matter systems. (Note, that we do not use the standard notation of n for the band index, as n will later enumerate the sites of tight-binding lattices). The $|u_{\alpha,k}(t)\rangle$ are the cell-periodic parts of the Bloch wavefunction. An introduction to the Bloch basis is given in Appendix A. A general wave function $|\phi(t)\rangle$ must satisfy the time-dependent Schrödinger equation (we have set $\hbar = 1$)

$$i\partial_t|\phi(t)\rangle = \hat{H}(t)|\phi(t)\rangle. \tag{2.2}$$

and we have dropped the quantum number k for the moment, as translation invariance forbids coupling between different k values. The expansion of the wavefunction in terms of the instantaneous eigenstates of the Hamiltonian is

$$|\phi(t)\rangle = \sum_\alpha c_\alpha(t) e^{-i\int_0^t E_\alpha(t')dt'}|u_\alpha(t)\rangle, \tag{2.3}$$

where the dynamical phase is factored out. Plugging Eq. (2.3) back into Eq. (2.2) and

using orthonormality between eigenstates results in

$$\dot{c}_\alpha(t) = -c_\alpha(t)\langle u_\alpha(t)|\partial_t|u_\alpha(t)\rangle - \sum_{\beta\neq\alpha} c_\beta(t) e^{-i\int_0^t (E_\beta(t')-E_\alpha(t'))dt'} \langle u_\alpha(t)|\partial_t|u_\beta(t)\rangle. \tag{2.4}$$

Time differentiating Eq. (2.1), taking the internal product with $\langle u_\beta(t)|$, and switching the index labels ($\alpha \leftrightarrow \beta$), leads to

$$\langle u_\alpha(t)|\partial_t|u_\beta(t)\rangle = -\frac{\langle u_\alpha(t)|\dot{H}|u_\beta(t)\rangle}{E_\alpha(t) - E_\beta(t)} \tag{2.5}$$

and we realize that we can neglect the second term on the right-hand side of Eq. (2.4), as long as as the rate of change of the Hamiltonian is small compared to the energy spacing between energy levels. This is the adiabatic approximation [59]. Of course, this can always be achieved for systems with finite energy gaps in the limit of $\dot{R} \to 0$, which is refered to as the adiabatic limit.

When neglecting the second term on the right-hand side, Eq. (2.4) decouples and subsequently can easily be solved via

$$c_\alpha(t) = e^{i\gamma_\alpha(t)} c_\alpha(0), \tag{2.6}$$

where we have defined the Berry phase $\gamma_\alpha(t) = i\int_0^t \langle u_\alpha(t')|\partial_{t'}|u_\alpha(t')\rangle dt'$. It is easy to show that the Berry phase is real. Thus, during an adiabatic time evolution, the expansion coefficients, c_α are only multiplied by a complex phase and do not change their magnitude. This constitutes the main message of the adiabatic theorem: For an adiabatic modulation, no excitations to energy states of higher or lower bands occur, as $|c_\alpha(t)|^2 = |c_\alpha(0)|^2$. Most importantly for Thouless pumps, this means that an initial uniform band occupation will stay a uniform band occupation during the complete pumping cycle.

The Berry phase can be rewritten as an integral over parameter space

$$\gamma_\alpha(t) = i\int_0^t \langle u_\alpha(t')|\partial_{t'}|u_\alpha(t')\rangle dt' = i\int_{R(0)}^{R(t)} \langle u_\alpha(R')|\partial_{R'}|u_\alpha(R')\rangle dR', \tag{2.7}$$

which shows that it only depends on the path that is taken in parameter space, but not on the elapsed time. Hence, it is called a geometric phase. Originally, it was thought that this geometric phase is merely a phase choice and can be gauged away by redefining the eigenstates. While this is true for open paths, Berry realized that this is not true anymore if the path is closed in parameter space (e.g. the modulation is cyclic) and

the Hamiltonian comes back to itself [60]. In this case, γ_α becomes a gauge invariant quantity and has physical consequences [61]. We will revisit this point in Chapter 2.2.3 when we discuss the relation between Wannier states and Thouless pumps.

Before we can derive the quantization of particle transport, we have to consider the wavefunction to first-order correction. Suppose we initially have $c_\alpha(0) = 1$, such that $c_\alpha(t) \approx 1$ and $c_{\beta\neq\alpha}$ is of first order in the rate of change of R. Then, to first order in the rate of change of R (neglecting terms such as $\dot{R}^2$, $\ddot{R}$ and $c_\beta \dot{R}$), the wavefunction is given by [29]

$$|\phi(t)\rangle = e^{-i\int_0^t E_\alpha(t')dt'} e^{i\gamma_\alpha(t)} \left(|u_\alpha(t)\rangle + i \sum_{\beta\neq\alpha} \frac{\langle u_\beta(t)|\partial_t|u_\alpha(t)\rangle}{E_\beta - E_\alpha} |u_\beta(t)\rangle \right). \tag{2.8}$$

As expected, this quasiadiabatic wavefunction mostly occupies $|u_\alpha(t)\rangle$ with slight corrections stemming from other bands due to non-perfect adiabaticity.

Using Ehrenfest's theorem, the expectation value for the velocity (in the wavevector representation) of a particle with quantum numbers k and α is

$$v_{\alpha,k}(t) = \frac{d\langle x\rangle}{dt} = i\langle[\hat{H}, \hat{x}]\rangle = \left\langle \frac{\partial \hat{H}_k(t)}{\partial k} \right\rangle, \tag{2.9}$$

where we have reintroduced the wavevector k. Using Eq. (2.8) and only keeping terms to first order, leads to [57]

$$v_{\alpha,k}(t) = \frac{\partial E_{\alpha,k}(t)}{\partial k} + i \sum_{\beta\neq\alpha} \left(\frac{\langle u_{\alpha,k}(t)|\partial_t|u_{\beta,k}(t)\rangle\langle u_{\beta,k}(t)|\frac{\partial \hat{H}_k(t)}{\partial k}|u_{\alpha,k}(t)\rangle}{E_{\alpha,k}(t) - E_{\beta,k}(t)} - c.c. \right), \tag{2.10}$$

where *c.c.* denotes the complex conjugate. The first term on the right hand side of Eq. (2.10) is the group velocity, $v^{(\mathrm{gr})}_{\alpha,k}(t)$, defined by the band structure of the system. The second term is called the anomalous velocity, $v^{(\mathrm{a})}_{\alpha,k}(t)$. On first sight, this result is puzzling as the velocity is determined as a function of unoccupied bands [58]. But we know that in the adiabatic limit, those states do not participate. To resolve this, we use $\langle u_{\beta,k}(t)|\frac{\partial \hat{H}_k(t)}{\partial k}|u_{\alpha,k}(t)\rangle = (E_{\beta,k}(t) - E_{\alpha,k}(t))\langle u_{\beta,k}(t)|\partial_k|u_{\alpha,k}(t)\rangle$ and $\sum_\beta |u_{\beta,k}(t)\rangle\langle u_{\beta,k}(t)| = 1$ to rewrite the anomalous velocity as [57]

$$v^{(\mathrm{a})}_{\alpha,k}(t) \equiv \dot{R}\Omega_\alpha(k, R), \tag{2.11}$$

where we have defined $\Omega_\alpha(k, R)$ as the gauge-invariant Berry curvature over the two-

dimensional parameter space (k,R) as

$$\Omega_\alpha(k,R) = i\left[\left\langle \frac{\partial u_{\alpha,k}(t)}{\partial R}\middle|\frac{\partial u_{\alpha,k}(t)}{\partial k}\right\rangle - \left\langle \frac{\partial u_{\alpha,k}(t)}{\partial k}\middle|\frac{\partial u_{\alpha,k}(t)}{\partial R}\right\rangle\right]. \tag{2.12}$$

Finally, we are in the position to calculate the transport of a single particle during one adiabatic cyclic modulation. The center of mass displacement per period of a particle in a state labelled by wavevector k and in band α is given by the time-integrated velocity as

$$\Delta x_{\alpha,k} = \int_0^T v_{\alpha,k}^{(\mathrm{gr})}(t)dt + \int_{R(0)}^{R(T)} \Omega_\alpha(k,R)dR. \tag{2.13}$$

It is simple to see, that this quantity is non-quantized as the first term ins unbounded. Instead, we consider a particle that uniformly occupies all k states within an isolated band. Equivalently we can consider a completely filled band. In both cases the integrated group velocity is zero and the first term vanishes. Thus, the center of mass displacement after one period is

$$\begin{aligned}\Delta x_\alpha &= \frac{a}{2\pi}\int_{\mathrm{BZ}} dk \int_{R(0)}^{R(T)} \Omega_\alpha(k,R)dR \\ &= \frac{a}{2\pi}\oint \Omega_\alpha(k,R)\,dk\,dR \\ &\equiv a\cdot C\end{aligned} \tag{2.14}$$

where a is the lattice constant and the integral is over the first Brillouin zone (BZ). In the third line we combined the integrals to show that the integral is closed due to the periodicity of the Brillouin zone as well as the periodicity of the modulation. The last equality defines the Chern number, C, via $\oint \Omega_\alpha(k,R)\,dk\,dR = 2\pi C$. By converting the surface integral (of a closed torus) into a contour integral using Stoke's theorem, it can be shown that the Chern number is integer quantized [6, 57]. It is called the topological invariant of the system and characterized the transport properties of single isolated bands.

In summary, for an adiabatic modulation, and a uniformly filled band, the center of mass displacement per period is integer quantized by the Chern number in units of the lattice constant. Apart from the mathematical description presented in this section, there is a more intuitive way to understand the quantization of Thouless pumps in terms of the the center of mass positions of Wannier states. We discuss this approach in Chapter 2.2.3, after introducing the Wannier basis.

2.1.3 Relation to 2D systems and dimensional reduction

Finally, we discuss the question, how to find a nontrivial (Chern number different from zero) Thouless pumping model. The simplest and often most practical way is through dimensional reduction: Take any two-dimensional Chern insulator system, that is described by the Hamiltonian $\hat{H}(k_x, k_y)$, and promote one of the wavevectors to denote the cyclic modulation $k_y a \to R(t)$. Then, the new Hamiltonian $\hat{H}(k_x, R)$ represents a spatially one-dimensional system that is periodically modulated in time. By definition the resulting Thouless pump will show quantized pumping dictated by the Chern number of the two-dimensional Chern insulator. While this method is general, the resulting Thouless pumps can have complicated Hamiltonians and long-range hoppings which are difficult to realize experimentally. Of course, also the reverse way of dimensional extension is possible: Any Thouless pump can be promoted to be a two-dimensional Chern insulator and the quantization of transport is directly related to the quantization of conductance in the two-dimensional case.

One simple Thouless pumping model can be derived from the Harper-Hofstadter model, which describes a square lattice with nearest-neighbor hoppings of strength $|J|$ and a perpendicular magnetic field. Assuming a threaded flux of one third of a flux quantum per plaquette, the tight-binding Hamiltonian (in wavevector representation) is

$$H(k_x, k_y) = \begin{bmatrix} -2J\cos(k_y a) & -J & -Je^{-ik_x a} \\ -J & -2J\cos\left(k_y a + \frac{2\pi}{3}\right) & -J \\ -Je^{ik_x a} & -J & -2J\cos\left(k_y a + \frac{4\pi}{3}\right) \end{bmatrix}. \tag{2.15}$$

Replacing $k_y a \to R(t) = \Omega t$, turns Eq. (2.15) into a spatially one-dimensional model with a three-site unit-cell. Thouless pumping is realized through periodically modulating the strength of the on-site potential with different phase offsets for the three sites per unit cell. This model is called the diagonal Aubry-André-Harper (AAH) model [62–64]. In femto-second laser written waveguides the on-site potential modulation can be realized by changing the speed of translation during the fabrication process. But the level of control is much lower compared to a modulation of the nearest-neighbor hopping strengths. Therefore, we use the off-diagonal version of the AAH model, in which the modulation occurs in the hopping strengths. Equation (2.16) shows the Hamiltonian of

the off-diagonal version

$$H(k_x, \Omega t) = \begin{bmatrix} 0 & -J_{12}(t) & -J_{31}(t)e^{-ik_x a} \\ -J_{12}(t) & 0 & -J_{23}(t) \\ -J_{31}(t)e^{ik_x a} & -J_{23}(t) & 0) \end{bmatrix} \tag{2.16}$$

with

$$J_{12}(t) = J + \Delta J \cos(\Omega t) \tag{2.17}$$

$$J_{23}(t) = J + \Delta J \cos\left(\Omega t + \frac{2\pi}{3}\right) \tag{2.18}$$

$$J_{34}(t) = J + \Delta J \cos\left(\Omega t + \frac{4\pi}{3}\right) \tag{2.19}$$

In this model, the hoppings have a mean strength of J, modulated with a strength of ΔJ. In typical experiments $|\Delta J/J| < 1$, such that the hoppings do not change their phase (e.g. change from positive to negative) during the pumping cycle. Despite their similarities, the diagonal and the off-diagonal AAH models are topologically not equivalent [64]. Using the above description it is easy to generalize the AAH model to models with more sites per unit cell (as will be necessary in Chapter 5).

2.2 The Wannier basis

Wannier functions are an essential ingredient for the understanding of the theory and the experiments presented within this dissertation and perhaps the simplest way to understand Thouless pumping. In particular, Wannier functions will be of fundamental importance for the derivations presented in Chapter 4. In the following, we will first introduce single-band Wannier states and their most important properties, before extending the discussion to multi-band Wannier states. Finally, we will show the relation between Wannier states and Thouless pumping. We exclusively discuss one-dimensional Wannier states as are important in Thouless pumping. This section is based on an a review of Wannier functions in the context of topology that can be found in Ref. [65].

2.2.1 Single-band Wannier states

Assuming an isolated energy band, the single-band Wannier functions of band α, $|w_{R,\alpha}\rangle$, are defined as [66]

$$|w_{R,\alpha}\rangle = \frac{1}{\sqrt{N}} \sum_k e^{-ikR} |B_{k,\alpha}\rangle, \tag{2.20}$$

where N is the number of unit cells and the sum over k includes all values of the wavevector k in the Brillouin zone that are consistent with periodic boundary conditions. $|B_{k,\alpha}\rangle$ denotes the Bloch states of band α. We define the Bloch basis in Appendix A. There are as many single-band Wannier states as unit cells. Hence we use the lattice vector R to enumerate them. We have given the discrete definition here; in the continuum formulation the summation over k is replaced with an integral over the 1-dimensional Brillouin zone $\sum_k \to \frac{N}{\Omega_{\mathrm{BZ}}} \int_{\mathrm{BZ}}$, where $\Omega_{\mathrm{BZ}} = 2\pi/a$ is the volume of the Brillouin zone. Examples of single-band Wannier states for two different bands in a three band model are shown in Fig. 2.2a and c.

In other words, single-band Wannier states are the Fourier transform pairs of the Bloch states of a single band. Furthermore, in Appendix A, we prove the following important properties of Wannier states: (1) We show the orthogonality and completeness of Wannier states. And (2), we show that different Wannier states are related by translations of multiples of the lattice vector (see also Fig. 2.2a and c). This means, that once a single Wannier function is found, all others are easy to construct. From Eq. (2.20) it is also apparent, that Wannier states are not uniquely defined. Instead, each Bloch wavefunction $B_{k,\alpha}$ can be defined with a different phase $B_{\boldsymbol{k},\alpha}(\boldsymbol{r}) \to e^{i\zeta_{\boldsymbol{k},\alpha}} B_{\boldsymbol{k},\alpha}(\boldsymbol{r})$. This gauge choice can be used to change the localization properties of the Wannier states. In one-dimensional systems, it has been shown that Wannier states can always be chosen to be real and exponentially localized. A proof for crystals with inversion symmetry can be found in Ref. [67], and for more general crystals without inversion symmetry in Ref. [68].

As all Wannier states are just translational copies of each other, we can select one individual, discuss its properties, and then generalize. For simplicity, we focus on the Wannier state denoted by $R = 0$. From Eq. (2.20) it is now easy to see, that Wannier states are simply a summation over all Bloch states. Thus, if we prepare a particle in a Wannier state, its wavefunction has a uniform projection onto the respective energy band, as illustrated in Fig. 2.2b and d, in which a single-band Wannier state is projected onto the Bloch eigenstates. Hence, Wannier states meet the requirements necessary to observe quantized transport in Thouless pumps. In particular, an adiabatically-modulated system initially excited with a Wannier state, will have a uniform band projection at all times.

Furthermore, Wannier states can be chosen strongly localized, and are therefore ideal excitations in photonic waveguide experiments, where localized excitations are simpler to realize.

The localization properties [69] are one main advantage of the Wannier basis compared to the Bloch basis. Typically, the most important Wannier states are the most localized ones (e.g. with the smallest spread) which are referred to as maximally-localized Wannier states and are the solid state equivalent of localized molecular orbitals. A localized basis bears advantage as short-range interactions will only mediate interactions between few, not too distanced Wannier states, but all Bloch states are needed to equivalently describe the interactions.

While it is simple to *define* Wannier functions in any dimension, it took until Marzari and Vanderbilt [70] to introduce a practical way to numerically find maximally-localized Wannier states. The exception is one dimension, for which maximally-localized Wannier states can be conveniently calculated as the eigenvectors of the projected position operator $\hat{P}\hat{X}\hat{P}$ [71], where $\hat{P} = \sum_k^{\text{occ}} |B_{k,n}\rangle\langle B_{k,n}|$ is the projection operator of the occupied band and $\hat{X} = \text{diag}(e^{i2\pi\hat{x}/N})$ is the Resta position operator [72] with $\hat{x}$ being the standard position operator.

Given the exponential localization of Wannier states, their center of mass position is meaningful. Due to its relevance for Thouless pumping, we explicitly derive it here in one dimension. For simplicity, we use $R = 0$ and the continuum formulation and first calculate the effect of the position operator on a Wannier state:

$$\begin{aligned}
\hat{x}|w_{0,\alpha}\rangle &= \frac{a}{2\pi}\int_0^{2\pi/a} dk\, x e^{ikx}|u_{k,\alpha}\rangle \\
&= \frac{a}{2\pi}\int_0^{2\pi/a} dk\, (-i\partial_k e^{ikx})|u_{k,\alpha}\rangle \\
&= \frac{a}{2\pi}\int_0^{2\pi/a} dk\, e^{ikx}(i\partial_k|u_{k,\alpha}\rangle), \qquad (2.21)
\end{aligned}$$

where we have used partial integration for the third line. The center of mass position of a single-band Wannier state (defined as the diagonal position operator matrix element) in one dimension is given by:

$$\begin{aligned}
\langle w_{0,\alpha}|\hat{x}|w_{0,\alpha}\rangle_V &= \left(\frac{a}{2\pi}\right)^2 \int_0^{2\pi/a} dq \int_0^{2\pi/a} dk\, \langle u_{q,\alpha}|(e^{i(q-k)x} i\partial_k|u_{k,\alpha}\rangle_V \\
&= \left(\frac{a}{2\pi}\right)^2 \int_0^{2\pi/a} dq \int_0^{2\pi/a} dk\, \langle u_{q,\alpha}|(e^{i(q-k)x} i\partial_k|u_{k,\alpha}\rangle_{UC} \sum_R e^{i(k-q)R}
\end{aligned}$$

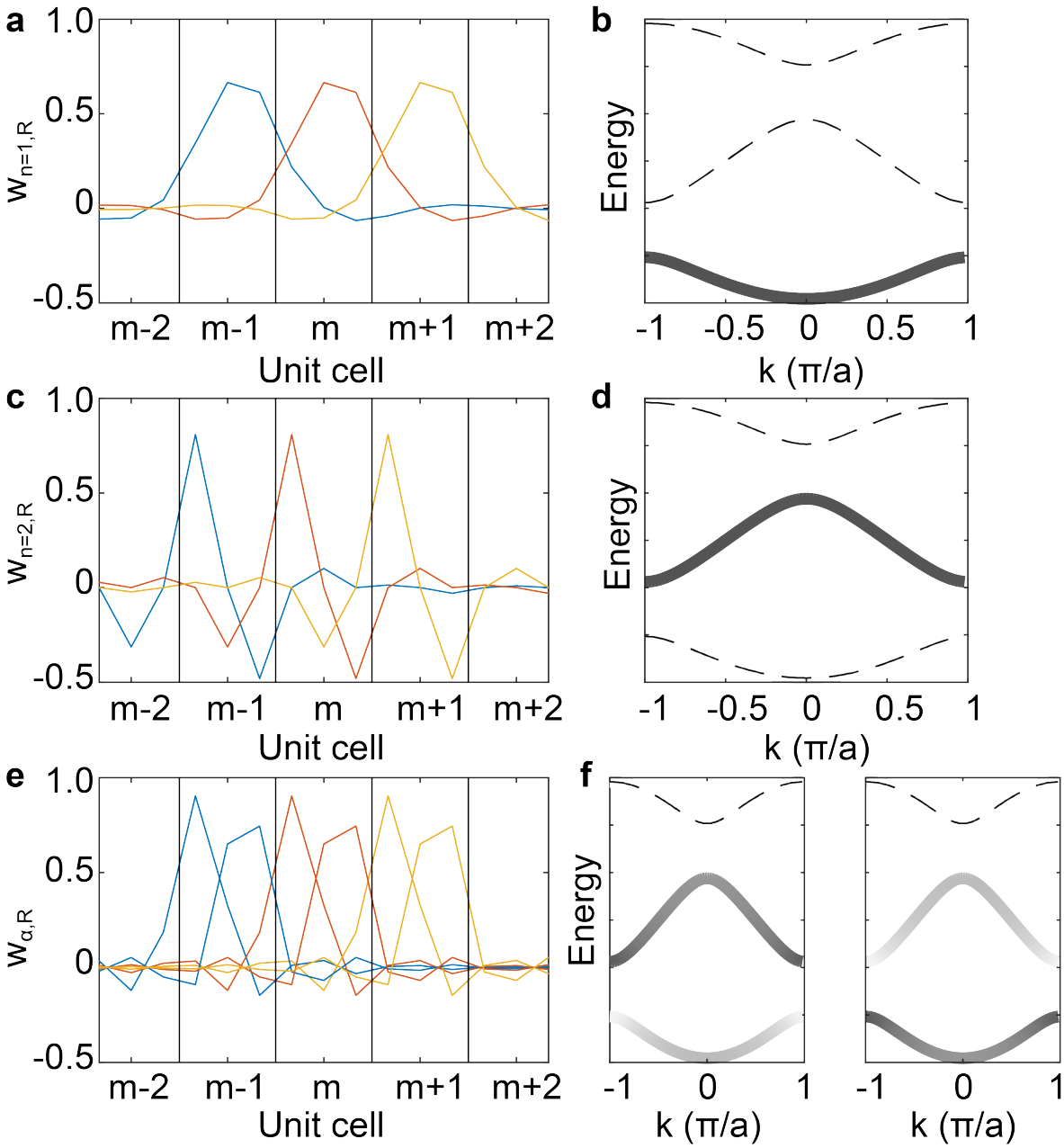

Figure 2.2. Wannier functions in a multi-band model. **a**, Maximally-localized single-band Wannier functions of the lowest (α=1) band shown in three neighboring unit cells. Equivalently, these are non-maximally-localized multi-band Wannier states. **b**, Projection of a single-Wannier state from **a** onto the Bloch states showing with uniform occupation of the lowest band. The dashed lines illustrates the position of bands with no projection. **c**,**d**, Similar to **a**,**b**, but for the second-lowest band (α=2). **e**, Examples of maximally-localized multi-band Wannier functions of the lowest two bands localized in three neighboring unit cells. There are two Wannier functions localized in each unit cell. **f**, Projection of the two different multi-band Wannier functions from **e** onto the Bloch states, that show nonuniform occupation. When both panels are overlaid, the occupation becomes uniform in both bands.

$$
\begin{aligned}
&= \frac{a}{2\pi}\int_0^{2\pi/a} dq \int_0^{2\pi/a} dk \, \langle u_{q,\alpha}|(e^{i(q-k)x} i\partial_k |u_{k,\alpha}\rangle_{UC} \delta(k-q) \\
&= \frac{a}{2\pi}\int_0^{2\pi/a} dk \, \langle u_{k,\alpha}| i\partial_k |u_{k,\alpha}\rangle_{UC} \\
&= \frac{a}{2\pi}\gamma_\alpha,
\end{aligned} \tag{2.22}
$$

where the subscript V denotes an integration over the whole system, while UC denotes an integration over the unit cell only. In the last line, we have used the definition of the Berry phase. Importantly, the Berry phase is calculated for a closed path through the one-dimensional Brillouin zone, instead of an externally modulated parameter (as described in Chapter 2.1.2), a far from trivial realization first made by Zak [73]. According to equation 2.22, the center of mass of a single-band Wannier state within a unit cell is given by the Berry phase that is gauge independent, confirming that gauge invariant quantities are important as they often have physical meaning. In this case, it has been realized that the Berry phase (and therefore the position of the Wannier state) can be used to define the polarization, in what is now known as the modern theory of polarization [72, 74, 75].

2.2.2 Multi-band Wannier states

If two or more energy bands are degenerate, single-band Wannier states cannot be defined anymore [69]. Instead, if a group of bands is isolated from all other energy bands, multi-band Wannier states can be defined as

$$
|w_{R,\tilde{\alpha}}\rangle = \frac{1}{\sqrt{N}} \sum_k e^{-ikR} |\tilde{B}_{k,\tilde{\alpha}}\rangle, \tag{2.23}
$$

where, importantly, $|\tilde{B}_{k,\tilde{\beta}}\rangle$ are not Bloch states, but rather a combination of Bloch states (of same k) from different bands:

$$
|\tilde{B}_{k,\tilde{\alpha}}\rangle = \sum_\alpha U_{\tilde{\alpha},\alpha}(k) |B_{k,\alpha}\rangle. \tag{2.24}
$$

Here, $U_{\tilde{\alpha},\alpha}(k)$ is a unitary matrix that defines the degree of mixing of the Bloch states of different bands within the multi-band Wannier state and defines the gauge for the multi-band Wannier states. For multi-band Wannier states $\tilde{\alpha}$ looses its meaning as a band index, but merely enumerates the multi-band Wannier states ranging from one to the number of bands involved and we find the same number of Wannier states in each unit cell. Most properties of single-band Wannier states carry over to multi-band

Wannier states, including orthogonality, completeness and relation via translation.

Due to the k dependent mixing of Bloch states of different bands, multi-band Wannier states generally cannot be identified with a single band, but only with a group of bands. Furthermore, multi-band Wannier states show nonuniform (and non-universal) occupation of the bands (see Fig. 2.2f) and no quantization is expected in linear Thouless pumping for such an excitation. Using a particular gauge choice, namely $U_{\tilde{\alpha},\alpha} = \delta_{\tilde{\alpha},\alpha}$, we see that single-band Wannier states are one example of multi-band Wannier states.

The possibility of different gauge choices lead to different multi-band Wannier states and gauge dependent centers of mass, which is in contrast to the single-band Wannier states. The analogue gauge-invariant quantity is the sum of the centers of mass of the multi-band Wannier states [65]. We show examples of multi-band Wannier states (with different gauge choices) in Fig. 2.2 a,c,e. Clearly, the center of mass of individual multi-band Wannier states is gauge-dependent. Similar to the single-band Wannier states, typically, maximally-localized multi-band Wannier states are desired. In one dimension maximally-localized multi-band Wannier states can be efficiently calculated as eigenstates of the projected position operator, when projecting into the subspace of multiple bands. We point out that multi-band Wannier states can be calculated for groups of energetically separated bands, but must be used (instead of single-band Wannier functions) for degenerate bands.

2.2.3 Relation to Thouless pumping

In Chapter 2.2.1, we have shown that the center of mass position of single-band Wannier state is given by the Berry phase. In Chapter 2.1.2 we have derived an equation for the center of mass displacement of a wavefunction with a uniform band projection during an adiabatic Thouless pumping process. Here, we combine both results to show that the quantization in Thouless pumping can be analyzed by the center of mass displacement of single-band Wannier states. In other words, in Thouless pumps, the winding of the Wannier states is equal to the Chern number.

Using Eq. (2.14), the center of mass displacement after one period and for a particle that uniformly occupies a single band is given by

$$\begin{aligned}\Delta x_\alpha &= a \cdot C \\ &= \frac{a}{2\pi} \oint \Omega_\alpha(k, R)\, dk\, dR\end{aligned}$$

$$
\begin{aligned}
&= \frac{a}{2\pi}\int_{R(0)}^{R(T)} dR \left(\int_0^{\frac{2\pi}{a}} dk\, \Omega_\alpha(k,R)\right) \\
&= \frac{a}{2\pi}\int_{R(0)}^{R(T)} dR \left(i\int_0^{\frac{2\pi}{a}} dk\ (\langle\partial_R u_{k,\alpha}(R)|\partial_k u_{k,\alpha}(R)\rangle - \langle\partial_k u_{k,\alpha}(R)|\partial_R u_{k,\alpha}(R)\rangle)\right) \\
&= \frac{a}{2\pi}\int_{R(0)}^{R(T)} dR \left(i\int_0^{\frac{2\pi}{a}} dk\ (\langle\partial_R u_{k,\alpha}(R)|\partial_k u_{k,\alpha}(R)\rangle + \langle u_{k,\alpha}(R)|\partial_R\partial_k u_{k,\alpha}(R)\rangle)\right) \\
&= \frac{a}{2\pi}\int_{R(0)}^{R(T)} dR\ \frac{\partial}{\partial_R}\left(i\int_0^{\frac{2\pi}{a}} dk\, \langle u_{k,\alpha}(R)|\frac{\partial}{\partial_k}|u_{k,\alpha}(R)\rangle\right) \\
&= a\int_{R(0)}^{R(T)} dR\ \left(\frac{1}{2\pi}\frac{\partial}{\partial_R}\gamma_\alpha(R)\right). \qquad (2.25)
\end{aligned}
$$

This set of equations is most easily verified from bottom to top, where we have used the product rule for differentiation from the sixth to the fifth line, and partial integration from the fifth to the forth line. The result shows that the integrated change of the Berry phase divided by 2π is equal to the Chern number. As the Berry phase (calculated over the Brillouin zone) determines the position of the single-band Wannier states, the change of the Berry phase is equal to change of the position of the Wannier states. As a result, tracking the position of the instantaneous Wannier states as a function of the adiabatic parameter R, is perhaps the easiest way to calculate the Chern number and to analyze the topology of Thouless pumps. For a Chern number C, the Wannier states are being displaced by C unit cells after each period and the position of the Wannier states (projected into one unit cell) winds C times around the unit cell. This argument can be generalized to multi-band Wannier states, where the winding of sum of the centers of the multi-band Wannier states gives the sum of the Chern numbers of the respective bands.

2.3 Coupled waveguides

The extremely rich and versatile world of coupled waveguides forms the basis of the experimental work in Chapters 3 and 5. For this dissertation, we define a waveguide as a structure that confines light in two spatial directions while it is free to propagate in the remaining third. The transverse spatial shape of the waveguide determines the mode of the waveguide, meaning the electric field profile that is supported. Waveguides can support multiple modes (multi-mode waveguides) but here we are only concerned with single-moded waveguides. Perhaps the most commonly known waveguides are optical fibers that form the backbone of today's internet architecture and can be drawn with lengths of tens of kilometers. Apart from drawing optical fibers, waveguides can

be fabricated and explored in a variety of ways, amongst them in silicon photonics, plasmonics, or using laser writing. The techniques differ in precision, propagation losses, and their capabilities to write arbitrary configurations. In this dissertation, we use femto-second laser written waveguides [76, 77], which can be fabricated with high precision, low propagation losses and in arbitrary 3D configurations [78].

In the following, we first introduce the fabrication of waveguides using femto-second laser writing. Second, we rederive the paraxial equation that governs the propagation of light in our waveguide arrays. As the paraxial equation is mathematically identical to the Schrödinger equation, waveguide arrays can be used to investigate a plethora of physical effects, including Hamiltonians known from condensed matter. We further introduce the tight-binding approximation and the effects of nonlinearities on the propagation of light, in particular the formation of spatial solitons. Finally, we will introduce directional couplers, the workhorse device to measure the most important experimental parameters in coupled waveguide arrays.

2.3.1 Direct femto-second laser writing

Perhaps the most versatile technique for the fabrication of coupled waveguides is direct femto-second laser writing [76, 77, 79, 80]: A high power laser beam is focused into a suitable host material, that is translated through the focal point. At the focal point (more precisely, focal volume), multi-photon processes lead to a permanent change of the refractive index [78]. For an illustration of this process, see Fig. 2.3.

The index changing process depends on the material and can lead to a increase of the refractive index (densification) or decrease of the refractive index, typically on the order of 10^{-3}. To guide light, an increase in the refractive index is needed (as will become clear in Chapter 2.3.2) and the properties of such waveguides are highly analogous to those of drawn optical fibers. Popular materials, that lead to a refractive index increase, are fused silica [78] and borosilicate glass (e.g. Corning Eagle XG). The latter is the material used in this dissertation. But even in the case of a decrease in the refractive index, waveguides can be written (see for example the review in Ref. [81]). Those, so-called, type-2 waveguides, typically consist of two patterned regions that embrace an unperturbed region, which therefore locally has a higher refractive index compared to its surrounding. While waveguiding is possible in this configuration, it is comparatively harder to write low-loss waveguides with reproducible coupling strengths. Type-2 waveguides are used when there is no alternative material with a refractive index increase, as is the case for doped glasses suitable for lasing [82]. Typically, type-2 waveguides are not used for

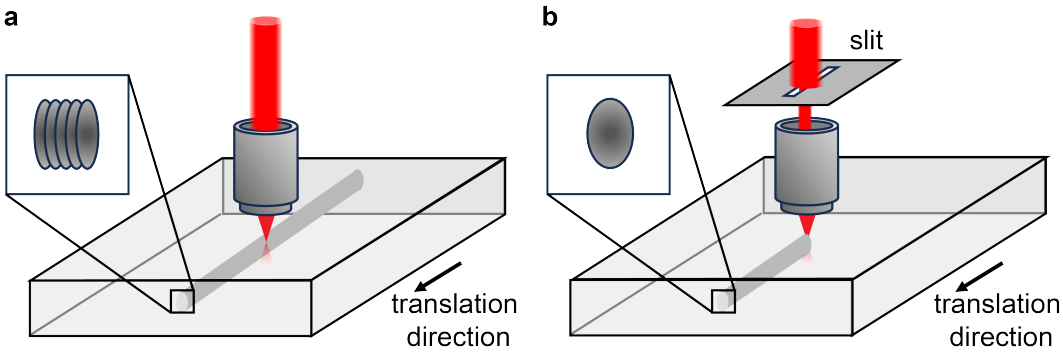

Figure 2.3. Direct femto-second laser writing. Focusing a femto-second laser beam into a suitable material leads to a permanent change in the refractive index. **a**, In the multi-pass technique, the sample is translated multiple times with small transverse displacements, to build up the desired refractive index profile, as illustrated in the inset. **b**, An adjustable slit, placed before the focusing lens, widens the focal spot such that waveguides can be written using only a single translation. This figure is replicated from Ref. [1]

waveguide arrays.

Simply focusing a laser beam into a suitable material, will lead to a change of the refractive index with a highly elliptical cross-section. In the transverse direction (orthogonal to the axis of the fabrication laser beam), the width of the created refractive index profile can even be smaller than the linear diffraction limit, as it stems from a multi-photon absorption process. In the longitudinal direction (parallel to the axis of the fabrication laser beam), the width of the created refractive index profile is typically larger. While those structures can guide light, it can be difficult to make them single-moded and write structures with well defined couplings in all directions. Furthermore, the modes typically have large propagation losses. More suitably shaped refractive index profile changes can be fabricated, for example, using the multi-pass technique or slit-beam shaping.

In the multi-pass technique, the sample is translated through the focus multiple times, with a small transverse off-set to build up the desired refractive index profile shape (see Fig. 2.3a). In principle, this technique allows for a precise control of the shape of the refractive index profile on the expense of being very time-consuming as each waveguide needs multiple passes. Using slit-beam shaping [83], waveguides can be written via a single translation. A mechanical slit is inserted in front of the focusing lens parallel to the writing direction (see Fig. 2.3b). As a result, the focal spot widens in the transverse direction, while simultaneously decreasing in the longitudinal direction. Typical fabrication parameters (as used for the work within this dissertation) are listed

Central wavelength of fabrication laser	1030 nm
Laser repetition rate	500 kHz
Temporal pulse width	≈260 fs
Average power	500-550 mW
Laser polarization	circular
Slit width	1.8 mm
Numerical Aperture	0.4
Translation speed	8 mm/s

Table 2.1. Fabrication parameters. Typical fabrication parameters for Eagle XG substrates using a Menlo BlueCut femto-second fiber laser system.

in Table 2.1. The resulting waveguides are slightly elliptical and have propagation losses as low as 0.3 dB/mm.

2.3.2 Paraxial equation and tight binding

In the following subsection we turn to the mathematical description of electromagnetic wave propagation in femto-second laser written waveguide structures. The propagation of electromagnetic fields is described by Maxwell's equations. Directly solving Maxwell's equation (as done in finite-difference time domain simulations), is not efficient for typical waveguide configurations. Instead, the propagation in waveguides with a small refractive index change (as in femto-second laser written waveguides) is described by the paraxial equation. We first rederive the paraxial equation and make the analogy to the Schrödinger equation apparent. Afterwards, we will introduce a corresponding tight-binding description that simplifies numerical calculations and is used throughout this dissertation. More information can be found for example in Refs. [84, 85].

Suppose we are given a system described by the refractive index profile $n(\boldsymbol{r}) = n_0 + \Delta n(\boldsymbol{r})$, where n_0 denotes the refractive index of the ambient medium (e.g. Eagle XG glass) and $\Delta n(\boldsymbol{r})$ describes the small refractive index changes due to femto-second laser writing. $\boldsymbol{r}$ is the position vector, with components in the $x-$, $y-$ and z-direction. We assume that the propagation direction of the waveguides is parallel to the z-direction. The four macroscopic Maxwell's equations in matter that describe the propagation of electromagnetic waves are as follows (using SI convention):

$$\nabla \cdot \boldsymbol{D} = \rho_f \tag{2.26}$$

$$\nabla \cdot \boldsymbol{B} = 0 \tag{2.27}$$

$$\nabla \times \boldsymbol{E} = -\frac{\partial \boldsymbol{B}}{\partial t} \tag{2.28}$$

$$\nabla \times \boldsymbol{H} = \boldsymbol{J}_f + \frac{\partial \boldsymbol{D}}{\partial t} \tag{2.29}$$

Here, $\boldsymbol{E}$ and $\boldsymbol{B}$ denote the electric and magnetic field, $\boldsymbol{D}$ and $\boldsymbol{H}$ denote the displacement and magnetic induction field, ρ_f and $\boldsymbol{J}_f$ are the free charge and current densities and t is time. To keep the equations short, we mostly omit to explicitly denote the spatial and temporal dependence of the fields.

The definition of the auxiliary displacement field $\boldsymbol{D}$ is given by the constitutive relation that relates the components D_i of the displacement field $\boldsymbol{D}$ with the components E_i of the electric field $\boldsymbol{E}$ via a power series (see for example Ref. [86]) as

$$D_i/\epsilon_0 = \sum_j \epsilon_{ij} E_j + \sum_{j,k} \chi^{(2)}_{ijk} E_j E_k + \sum_{j,k,l} \chi^{(3)}_{ijkl} E_j E_k E_l + O(E^4). \tag{2.30}$$

Here, ϵ_0 is the vacuum permittivity. A similar equation exists for the relation between $\boldsymbol{H}$ and $\boldsymbol{B}$, but for most dielectric materials (including the materials used within this dissertation), the relative magnetic permeability is scalar and close to unity ($\mu_r \approx 1$), such that $\boldsymbol{H} = \boldsymbol{B}/\mu_0$, with μ_0 the vacuum permeability.

To simplify the equations further, we assume the following: (1) The structure is time-independent with no free charges and currents. (2) The field strengths are small, such that we are in the linear regime. (3) The material is macroscopic and isotropic. (4) We assume monochromatic light.

From assumptions (2) and (3) follows that $\boldsymbol{E}$ and $\boldsymbol{D}$ are related by a scalar dielectric function, ϵ_r, also called the relative permittivity:

$$\boldsymbol{D} = \epsilon_0 \epsilon_r \boldsymbol{E}. \tag{2.31}$$

Using Eqs. (2.28) and (2.29), together with $\boldsymbol{H} = \boldsymbol{B}/\mu_0$ leads to the wave equation in medium

$$\nabla \times (\nabla \times \boldsymbol{E}) = -\nabla \times \frac{\partial \boldsymbol{B}}{\partial t} = -\frac{\partial}{\partial t} (\nabla \times \boldsymbol{B}) = -\mu_0 \epsilon_0 \epsilon_r \frac{\partial^2 \boldsymbol{E}}{\partial t^2} = -\frac{n^2}{c^2} \frac{\partial^2 \boldsymbol{E}}{\partial t^2}, \tag{2.32}$$

where we have introduced the speed of light, $c = 1/\sqrt{\mu_0 \epsilon_0}$, and the refractive index, $n = \sqrt{\epsilon_r \mu_r}$. The operator on the left-hand side couples the different polarizations and makes Eq. (2.32) computationally intensive to solve. This is the case for regular photonic

crystals (with large refractive index contrasts). After rewriting

$$\nabla \times (\nabla \times \boldsymbol{E}) = \nabla (\nabla \cdot \boldsymbol{E}) - \nabla^2 \boldsymbol{E} \tag{2.33}$$

we can neglect the first term on the right-hand side by using the weakly guiding approximation [87], that is justified as the refractive index change in femto-second laser written waveguides is on the order of 10^{-3}. As a result, Eq. 2.32 becomes a scalar equation. If we furthermore assume monochromatic light with angular frequency w_0 (assumption 4), we can write $E(\boldsymbol{r}, t) = E(\boldsymbol{r})e^{-iw_0 t}$ and we are left with

$$\nabla^2 E = -n^2 \frac{w_0^2}{c^2} E, \tag{2.34}$$

which is the Helmholtz equation.

We will now transform this equation into the paraxial equation. We start by writing the electric field as a transverse envelope function $\psi(x, y, z)$ that slowly changes in the propagation direction z and a carrier part that changes rapidly: $E(x, y, z) = \psi(x, y, z)e^{ik_0 z}$. Here, $k_0 = \frac{w_0 n_0}{c}$ is the wavevector of the carrier.

Plugging this into Eq. (2.34), and neglecting $\frac{\partial^2 \psi}{\partial z^2}$, which is justified when $|\frac{\partial^2 \psi}{\partial z^2}| \ll k_0 |\frac{\partial \psi}{\partial z}|$, we find

$$i\frac{\partial}{\partial z}\psi = -\frac{1}{2k_0}\nabla_\perp^2 \psi - \frac{k_0}{n_0}\frac{n^2 - n_0^2}{2n_0}\psi, \tag{2.35}$$

where $\nabla_\perp^2$ denotes the Laplacian in the transverse (x, y) directions. For femto-second laser written waveguide arrays the refractive index change is small and we approximate $n^2 \approx n_0^2 + 2n_0\Delta n$ to first order in Δn to obtain

$$i\frac{\partial}{\partial z}\psi(x, y, z) = -\frac{1}{2k_0}\nabla_\perp^2 \psi(x, y, z) - k_0\frac{\Delta n(x, y, z)}{n_0}\psi(x, y, z), \tag{2.36}$$

where we made the dependencies explicit again. Equation (2.36) is the paraxial equation that governs the dynamics of light in waveguide arrays. It is mathematically identical to the Schrödinger equation, with the propagation distance z playing the role of time t, and the electric field envelope $\psi(x, y, z)$ playing the role of the quantum mechanical wavefunction. At this point, it is also clear, why we strive to create a refractive index *increase*, as this leads to a potential *decrease* and thus to bound states and waveguiding.

Equation (2.36) can be efficiently solved using a symmetrized split step method (also referred to as beam propagation method) [84]. For simplicity, we introduce the kinetic

operator $\hat{T} \equiv -\frac{1}{2k_0}\nabla_\perp^2$ and the potential operator $\hat{V} \equiv -k_0\frac{\Delta n(x,y,z)}{n_0}$, such that

$$i\frac{\partial}{\partial z}\psi(x,y,z) = (\hat{T}+\hat{V})\psi(x,y,z) \tag{2.37}$$

For each operator individually, Equation (2.37) is simple to solve by exponentiation. For example, neglecting the kinetic part, the solution is $\psi(x,y,z) = e^{-i\hat{V}_D z}\psi(x,y,0)$, where the subscript D makes it apparent that the potential operator is a diagonal operator when acting on $\psi(x,y,z)$. Thus, the matrix exponential reduces to an exponential of a diagonal matrix which is simple to evaluate. When neglecting the potential operator, the equation is solved via $\psi(x,y,z) = e^{-i\hat{T}z}\psi(x,y,0) = \mathfrak{F}^{-1}\left(e^{-i\hat{T}_D Z}\,\mathfrak{F}\,\psi(x,y,z)\right)$, where we have introduced the spatial Fourier transform, $\mathfrak{F}$, and its inverse, $\mathfrak{F}^{-1}$, as the kinetic operator $\hat{T}$ becomes a diagonal operator ($\hat{T}_D$), when acting on the Fourier transformed wavefunction $\mathfrak{F}\psi(x,y,z)$. In the general case, when neither $\hat{T}$ nor $\hat{V}$ are neglected, this procedure will has to be modified as $\hat{T}$ and $\hat{V}$ do not commute. We can solve for small step sizes Δz via

$$\begin{aligned}
\psi(x,y,z+\Delta z) &= e^{-i(\hat{T}+\hat{V})\Delta z} \\
&= e^{-i\hat{T}_D\Delta z/2}e^{-i\hat{V}\Delta z}e^{-i\hat{T}\Delta z/2}\psi(x,y,z) \\
&= \mathfrak{F}^{-1}\left(e^{-i\hat{T}\Delta z/2}\,\mathfrak{F}\left(e^{-i\hat{V}_D\Delta z}\,\mathfrak{F}^{-1}\left(e^{-i\hat{T}_D\Delta z/2}\,\mathfrak{F}\,\psi(x,y,z)\right)\right)\right),
\end{aligned} \tag{2.38}$$

where we have used the Baker-Campbell-Hausdorff formula up to second order in Δz in the second line. In the last line we have made explicit, how the matrix exponentials are solved most easily. Using Fourier transforms we make sure that the matrix operators are each time evaluated as exponentials of a diagonal matrix.

It is possible to further simplify Eq. (2.36) for waveguides arrays using a tight-binding description when the distance between waveguides is large compared to the mode size. Taking inspiration from condensed matter systems, we assume that the wavefunction of the system can be approximated as a superposition of isolated orbital wavefunctions. This is a well suited approximation for coupled waveguide systems, for which the exponentially localized modes of isolated waveguides play the role of the the tightly-bound atomic orbital wavefunctions. As our waveguides are single-moded we only have to take into account one orbital per site.

For the derivation, we assume that we know the eigenstates of the isolated waveguides,

given by

$$\hat{H}_i|\psi_i\rangle = E_i|\psi_i\rangle \qquad \forall i = 1, 2, ..., N. \tag{2.39}$$

Here, N is the number of waveguides and $\hat{H}_i = \hat{T} + \hat{V}_i$ is the Hamiltonian, $\hat{T}$ is the kinetic operator and $\hat{V}_i$ is the potential operator defined by the refractive index change of waveguide i only. Furthermore, we assume that $\langle\psi_j|\psi_i\rangle = \delta_{j,i}$, hence the states are orthonormal. We aim to solve the paraxial equation for the full system, given by

$$i\frac{\partial}{\partial z}|\psi\rangle = \hat{H}|\psi\rangle, \tag{2.40}$$

where the Hamiltonian of the full system is given by $\hat{H} = \hat{T} + \sum_i \hat{V}_i = \hat{H}_i + \Delta U_i$ and the wavefunction $|\psi\rangle$ is unknown. Analogue to tight-binding, we assume that the wavefunction can be sufficiently well approximated by a linear combination of atomic orbitals: $|\psi\rangle = \sum_j \phi_j|\psi_j\rangle$, where the ϕ_j are complex expansion coefficients. Using this ansatz in Eq. (2.40) and multiplying from the left with $\langle\psi_i|$ results in:

$$\begin{aligned}
i\frac{\partial}{\partial z}\phi_i &= \langle\psi_i|\hat{H}|\psi\rangle \\
&= \sum_j \langle\psi_i|\hat{H}_i + \Delta U_i|\psi_j\rangle\phi_j \\
&= \langle\psi_i|\hat{H}_i + \Delta U_i|\psi_i\rangle\phi_i + \sum_{j\neq i}\langle\psi_i|\hat{H}_i + \Delta U_i|\psi_j\rangle\phi_j \\
&= \left(E_i + \langle\psi_i|\Delta U_i|\psi_i\rangle\right)\phi_i + \sum_{j\neq i}\langle\psi_i|\Delta U_i|\psi_j\rangle\phi_j \\
&\equiv V_i\phi_i - \sum_{j\neq i} J_{i,j}\phi_j \\
&\equiv H_{i,j}\phi_j
\end{aligned} \tag{2.41}$$

In the last two lines, we have defined the tight-binding Hamiltonian $H_{i,j}$, whose diagonal entries are the on-site potentials V_i for sites i and whose off-diagonal entries are the hopping parameters $J_{i,j}$ between modes i and j. These tight-binding parameters are typically treated as fitting parameters that are determined from the experiment. Often only the hopping between nearest-neighbor (and sometimes next-nearest neighbor) waveguides are taken into account, as the overlap between the tightly bounded wavefunction decreases exponentially the further the waveguides are apart. The resulting set of N coupled differential equations can be solved numerically extremely efficiently. Eigenvalues (and

therefore band structures) can be calculated by diagonalization. To solve for z propagation, we use a fourth order Runge-Kutta algorithm.

2.3.3 Nonlinearity and solitons

In the derivation of Eq. (2.36), we assumed only weak electric fields, and Eq. (2.30) was truncated after the linear term. In the presence of strong electric fields, this is not a good approximation anymore and higher order terms cannot be neglected. For inversion symmetric materials (as borosilicate glass), it can be shown that the second order terms are zero [87]. Thus, the next relevant order is three. Third order nonlinearity is commonly known as Kerr nonlinearity. Its effect can be incorporated as an intensity dependent change of the refractive index via $n = n_0 + n_2|E|^2$.

In the paraxial approximation, the nonlinearity can be added perturbatively

$$i\frac{\partial}{\partial z}\psi = -\frac{1}{2k_0}\nabla_\perp^2\psi - k_0\frac{\Delta n}{n_0}\psi - \frac{n_2|\psi|^2}{n_0}\psi, \tag{2.42}$$

where we have suppressed the spatial dependence of $n(x, y, z)$ and $\psi(x, y, z)$. In the tight-binding approximation this straightforwardly translates into

$$i\frac{\partial}{\partial z}\phi_j = \sum_j H_{j,i}\phi_i - g|\phi_j|^2\phi_j, \tag{2.43}$$

where g can be treated as a parameter describing the strength of the nonlinearity that is determined from the experiment. For a focusing nonlinearity $g>0$. A different derivation can be found in Ref. [88].

Equations (2.42) and (2.43) are known as the continuum and discrete nonlinear Schrödinger equation, respectively. The continuum version (with $\Delta n = 0$) is also known as Gross-Pitaevskii equation for Bose-Einstein condensates. In that case, ψ describes the condensate wavefunction in the mean-field limit and n_2 is proportional to the s-wave scattering strength between the atomic constituents [89]. The nonlinearity therefore describes the interaction between bosonic particles in the mean-field limit (in which the operators are replaced with complex numbers and fluctuations around their mean values are small). In the photonics case, the nonlinearity describes the collective effect of photons interacting with each other mediated by the underlying medium.

The introduction of nonlinearity has severe consequences: (1) The eigenstates of the (nonlinear) Hamiltonian do not form a complete basis anymore. As a result, most useful tools for solving linear differential equations and even tools for an intuitive understanding,

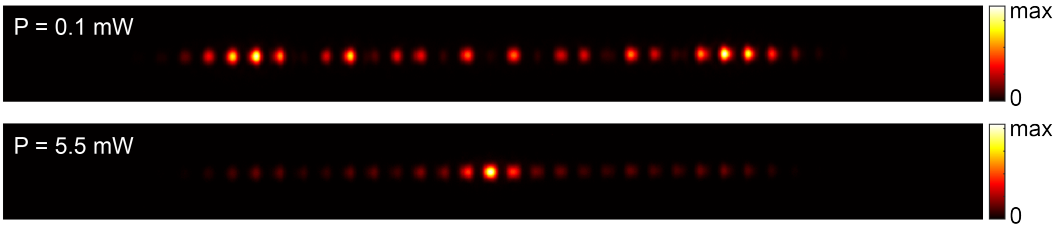

Figure 2.4. Observation of discrete soliton formation. Intensity distribution at the output facet of a 76-mm-long array of straight waveguides with a separations of 19 μm between waveguides. The upper panel shows discrete diffraction for linear propagation at input power of P=0.1 mW. The lower panel shows discrete spatial soliton formation at high input power of P=5.5 mW.

become invalid. In non-integrable systems, not even the number of nonlinear eigenstates is known and we have to rely on numerical techniques to find the nonlinear eigenstates. (2) Nonlinear equations allow for particular eigenstates: solitons[1] [90, 91]. Solitons are localized states even in systems with underlying translation symmetry, as the nonlinearity breaks translation symmetry.

Solitons forming in waveguide arrays according to Eqs. (2.42) or (2.43) are localized in space and therefore called discrete spatial solitons. They can exist when the nonlinearity balances the (spatial) diffraction. In Fig. 2.4 we show the formation of a discrete spatial soliton in an array of femto-second laser written waveguides at high optical power. Intuitively, spatial solitons can be understood as eigenstates of their self-induced potential well. In this dissertation, we work exclusively with spatial solitons, but we note that there also exist other types, for example temporal solitons, for which the nonlinearity balances the (temporal) dispersion and the solitons are localized in time. Temporal solitons have important application in optical fiber systems, where they are, for example, used to generate a supercontinuums and frequency combs. Discrete spatial solitons in waveguide arrays were first predicted [92] and early observations of spatial solitons in waveguides were conducted in AlGaAs [93]. In two dimensions, spatial solitons were first observed in optically induced photonic lattices [94].

In contrast to their continuum counterpart ($\Delta n = 0$), there is no known analytical solution for discrete solitons in the discrete nonlinear Schrödinger equation and we rely on numerical techniques to find discrete solitons. In this dissertation, we use a self-consistency method and a Newton iteration scheme. Both algorithms are described in Appendix B. The discreteness has further consequences: While solitons in the continuum

[1] In the literature solitons are sometimes defined more strictly as nonlinear, travelling, nondissipative wave that emerges spatially unchanged from a collision with other solitons. In this dissertation, we use a less restrictive definition.

can propagate shape-preserving in any direction, moving solitons in lattices radiate due to a Peierls-Nabarro (PN) potential barrier [95]. When the soliton is localized at different positions within the lattice, its energy is different. Thus, a moving soliton effectively travels in a changing potential and radiates. Ultimately, after looses enough intensity, the soliton motion comes to a stop [96, 97].

The discrete solitons, discussed in later chapters of this dissertation, can be divided into two classes: stable and unstable solitons. Stable solitons can exist infinitely long, while unstable solitons will eventually fall apart. Already the slightest perturbations (e.g. numerical imprecision's) will perturb the unstable soliton enough to fall apart. The stability of solitons can be analyzed using linear stability analysis. Linear stability analysis is described in Appendix B.

2.3.4 Calibration of parameters using directional couplers

In this section, we will apply the tight-binding description and show how to experimentally extract the most important parameters for waveguide systems, namely: The coupling strength between waveguides as a function of separation, the on-site potential differences between waveguides, and the strength of nonlinearity. These parameters can be extracted from a two waveguide system, called directional coupler. While directional couplers are often portrayed in a form where two waveguides are well separated, then come close together and then separate again, we use an experimentally much simpler version as illustrated in Fig. 2.5, consisting of two straight waveguides with a separation s over a coupling length l.

In the tight-binding approximation (including Kerr nonlinearity), a two-waveguide system is described by the following two equations

$$i\frac{\partial}{\partial z}\phi_1 = V_1\phi_1 - J_{1,2}\phi_2 - g|\phi_1|^2\phi_1 \tag{2.44}$$

$$i\frac{\partial}{\partial z}\phi_1 = V_2\phi_2 - J_{2,1}\phi_1 - g|\phi_2|^2\phi_2 \tag{2.45}$$

with $J_{1,2} = J_{2,1} \equiv J$ due to reciprocity. For low input power ($g = 0$), the resulting set of equations can be solved exactly and for an initial condition of $\phi_1(0) = 1$ and $\phi_2(0) = 0$, we find for the intensity in waveguide 2 [98]:

$$|\phi_2(z)|^2 = \frac{1}{1 + \left(\frac{\Delta}{2J}\right)^2} \sin^2\left[Jz\sqrt{1 + \left(\frac{\Delta}{2J}\right)^2}\right]. \tag{2.46}$$

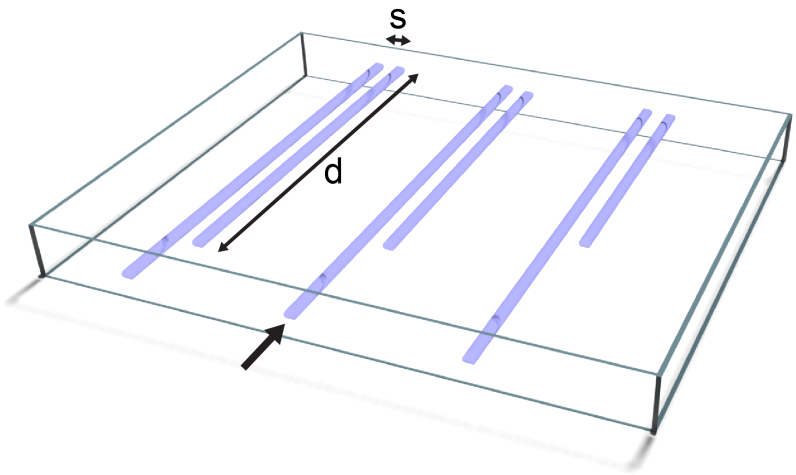

Figure 2.5. Illustration of directional couplers. Three directional couplers with equal separation s and decreasing coupling length d (from left to right). The black arrow indicates the excitation direction. Many relevant waveguide parameters can be calibrated using only directional couplers, including the coupling strength $J(s)$, an on-site potential difference V and the strength of nonlinearity g.

This formula can be used to determine J for a given separation s between the waveguides. For this, we excite waveguide one and measure the relative intensity $|\phi_2|^2$ in waveguide 2, as a function of propagation length z which is given by the length of the coupler l (see Fig. 2.6a). Fitting Eq. (2.46) to the measurement gives J as well as an on-site potential difference $\Delta = V_1 - V_2$. Repeating this measurement for couplers with different separations s, results in a functional form of $J(s)$, which can be well described by an exponentially decaying function. A typical result is shown in Fig. 2.6b. Intuitively, this can be understood by the exponentially decaying overlap (and thus hopping strength) between the two waveguide modes for increasing separation. To determine a relative on-site potential difference Δ, similar experiments can be performed by writing waveguides with increasing (or decreasing) speed.

In our experiments we observe small on-site potential differences also for directional couplers, for which both waveguides are written with identical power and speed (see Fig. 2.6c), indicating that the writing of the first waveguide leads to small environmental changes that effect the writing of the second. While we expect that this effect is strongly suppressed in the bulk of the system, we take care, especially in Chapter 5, that the on-site differences can be neglected. As an alternative to directional couplers, lattices can be used with equally spaced waveguides. While lattices have the advantage of no on-site potential differences in the bulk, they need more space.

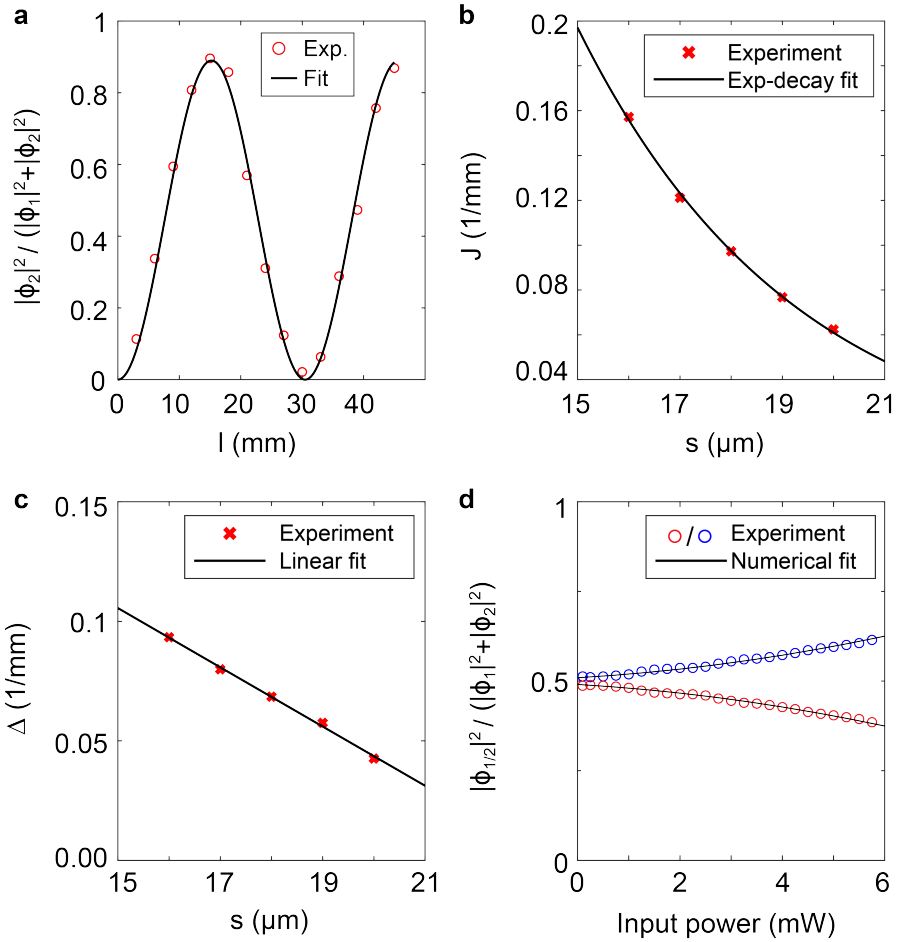

Figure 2.6. Waveguide characterization using directional couplers. **a**, Experimentally measured normalized intensity in waveguide 2 (red) as a function of coupling length l. The separation s=18 μm. The black line is a fit according to Eq. 2.46 resulting in J=0.10/mm and Δ=0.07/mm. **b**, Hopping strength J as function of separation. **c**, On-site potential difference Δ as a function of separation. **d**, Experimentally measured normalized intensity in waveguide 1 (red) and 2 (blue) as a function of input power. Fitting numerical propagation simulations gives a value of g=0.07/mm per mW input power.

At high power ($g > 0$) a single directional couplers can be used to determine the strength of nonlinearity g. We fit the output of numerical propagation simulations to experimentally measured output intensities, given that we have determined the hopping strength at low power. A typical result is shown in Fig. 2.6d.

Chapter 3
Integer quantized soliton Thouless pumping

This chapter describes the theoretical and experimental discovery of integer quantized pumping of solitons in nonlinear photonic Thouless pumps despite a nonuniform band projection. We find quantized soliton pumping by the Chern number for all bands. At higher power, spontaneous symmetry-breaking nonlinear bifurcations lead to a nonlinear phase transition resulting in a trapped soliton and zero pumping. Our implementation using coupled waveguides is amongst the first experimental works showing the emergence of topologically protected quantization in interacting bosonic systems. This chapter is based on work that was done in collaboration with Sebabrata Mukherjee and Mikael C. Rechtsman and has been published in Ref. [99].

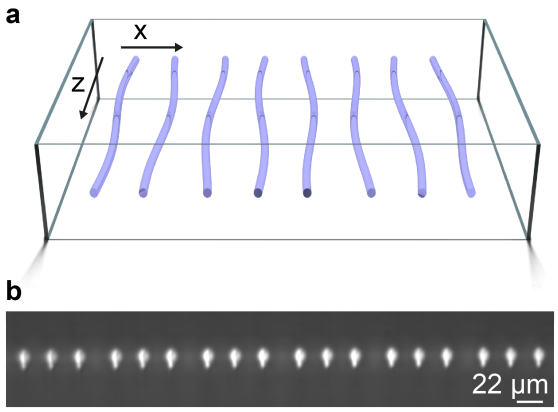

Figure 3.1. Photonic implementation of a topological Thouless pump. a, Schematic illustration of the implementation of a pump model in a one-dimensional waveguide array where the waveguides are modulated in plane. **b**, Micrograph of the output facet showing six out of ten unit cells for one lattice implementation.

3.1 Introduction

In the previous chapter, we have discussed that quantized transport is topologically protected in noninteracting/linear Thouless pumps with filled bands. Furthermore, we introduced soliton formation in coupled waveguide arrays at high optical power. In this chapter, we will combine both and show quantized soliton transport despite a nonuniform band projection.

Originally, topological protection was observed in the context of the integer quantum Hall effect [3] in two-dimensional electron gases. There, completely filled bands (for electrons, this means low temperature and a Fermi level in a bandgap) show topologically protected transport that results in a quantized conductance [3, 6] and, according to the bulk-boundary correspondence, leads to unidirectional edge states. For electron gases, it has been shown that topological protection not only occurs in clean systems, but instead persists even in the presence of many-body interaction and disorder, as long as the bandgap stays open, and interactions and correlations are short-ranged [31]. As a result, the conductance in the integer quantum Hall effect is precisely quantized (better than one part in 10^{-10} [4]) for a wide range of parameters and independent of sample details. Having said this, the significance of topology reaches far beyond two-dimensional electron gases. As a general wave phenomena, topology has been shown to apply broadly to a range of physical platforms, including fermionic platforms, like solid states, as well as bosonic platforms, like photonics, ultracold atoms in optical lattices, and others [20, 58].

For non-interacting systems, topology has been fully classified in the tenfold way based on the internal symmetries, time-reversal, charge conjugation symmetry, and a combination of both [100]. An extension to higher order topology has been brought forward, where the protection is based on spatial symmetries [101, 102], and d-dimensional systems have d-2 dimensional boundary phenomena. However, if topological protection is based on spatial symmetries, topology only protects against disorder that preserves that symmetry, which is typically not the case for random fabrication disorder [103], but could be applicable in certain solid state materials.

In photonics, a particularly suitable way to study topological protection of bulk transport is by using Thouless pumps [29], due to the design flexibility of fabricated photonic structures. A schematic of an implementation using waveguides is shown in Fig. 3.1. In summary (for more details see Chapter 2.1), a Thouless pump is a one-dimensional model that captures the topological quantization of transport in the integer quantum Hall effect using the notion of dimensional reduction: an adiabatically, time-varying

potential mathematically maps onto a momentum coordinate in a conceptual second dimension [29]. Analogue to the integer quantum Hall effect, quantization for Thouless pumps assumes uniformly filled electron bands below a Fermi energy, or an equivalent occupation for non-equilibrium bosonic systems. For bosons, this is experimentally often achieved using localized Wannier states, but it has also been proposed to use Bloch oscillations [42] or dissipation [43].

In complete analogy to the two-dimensional case, interparticle interactions and disorder do not destroy quantization in a fermionic Thouless pump as long as it is short-ranged and the bandgap stays open [30]. In contrast, disordered bosonic Thouless pumps might loose quantization in the thermodynamic limit as the bandgap goes to zero when different k-states can couple, but average quantization has been experimentally observed in finite disordered waveguide systems [51]. For interacting bosons even less is known and mostly theoretical work has been done. For example, Ref. [54] suggested that quantization persists for strong repulsive interactions as long as the superfluid phase is avoided. Although individual photons typically do not interact with each other, interactions between photons can be mediated by an underlying medium at high power, described collectively using nonlinearities in the mean-field limit (see also Chapter 2.3.3). Nonlinearities have shown to give raise to a variety of fascinating optical effects with significant technological application potentials for complex on-chip operations, including solitons, frequency combs and supercontinuum generation. Thus, it is important to understand the robustness of topological protection under the influence of particle interactions/nonlinearities and to study the emergence of novel topological protection schemes due to nonlinearities.

In this chapter we theoretically propose and experimentally demonstrate quantized nonlinear Thouless pumping of photons with a band projection that is decidedly nonuniform. In our system, nonlinearity acts to quantize transport via soliton formation. At even higher power spontaneous symmetry-breaking bifurcations lead to a transition to a trapped soliton and zero pumping. Quantization follows from the fact that the instantaneous soliton solutions centred upon a given unit cell are identical after each pump cycle, up to translation invariance; this is an entirely different mechanism from traditional Thouless pumping. This result shows that nonlinearity and interparticle interactions can induce quantized transport and topological behaviour without a linear counterpart.

3.2 The 3-site AAH model

We illustrate our findings of quantized nonlinear Thouless pumping in an array of coupled waveguides. In the scalar-paraxial regime, the propagation of monochromatic light in the array is governed by the discrete nonlinear Schrödinger equation (see Chapter 2.3.2):

$$i\frac{\partial}{\partial z}\phi_n = \sum_m H^{\text{lin}}_{n,m}(z)\phi_m - g|\phi_n|^2\phi_n. \tag{3.1}$$

Here, $\phi_n(z)$ is the wavefunction, that describes the strength of the electric field envelope in waveguide n; m and n run over all waveguides, $H^{\text{lin}}_{n,m}$ is the linear z-dependent tight-binding Hamiltonian (for example, describing a linear Thouless pump) and z is the propagation distance, which for Thouless pumps plays the part of a synthetic wavevector dimension. The parameter g describes the strength of the nonlinearity and is positive (negative) for a focusing (defocusing) Kerr nonlinearity. In the case of sufficiently low intensities, the equation reduces to the linear Schrödinger equation. From an experimental point of view, g is dependent on the nonlinear refractive index coefficient of the underlying material, on the effective area of the waveguide modes, and on the wavelength. This nonlinear Schrödinger equation with $g > 0$ is equivalent to an attractive Gross-Pitaevskii equation describing bosonic interactions in a Bose-Einstein condensate in the mean-field limit. Indeed, the results we obtain below are generically applicable to a range of bosonic wave systems.

We use an off-diagonal implementation of the Aubry-André-Harper (AAH) [62, 63] model with three sites per unit cell labelled A, B and C (Fig. 3.2a). The off-diagonal AAH model is described by a tight-binding Hamiltonian with equal on-site potential (which can be set to zero at all lattice sites) and real off-diagonal nearest-neighbour couplings $J_n(z)$ that are periodic functions with modulation frequency Ω. The modulation of the couplings over one period is displayed in Fig. 3.2b, where the choice of colours corresponds to Fig. 3.2a. Replacing the general linear Hamiltonian in equation (3.1) with the AAH model results in:

$$i\frac{\partial}{\partial z}\phi_n = J_n(z)\phi_{n+1} + J_{n-1}(z)\phi_{n-1} - g|\phi_n|^2\phi_n. \tag{3.2}$$

This equation conserves the norm of the solution: $P \equiv \sum_n |\phi_n|^2$.

To emphasize the relationship between a 1+1-dimensional pumping model (1 spatial and 1 propagation/temporal dimension) to a two-dimensional Chern insulator, we plot the band structure in Fig. 3.2c. At each point z within a period, the energy eigenvalues

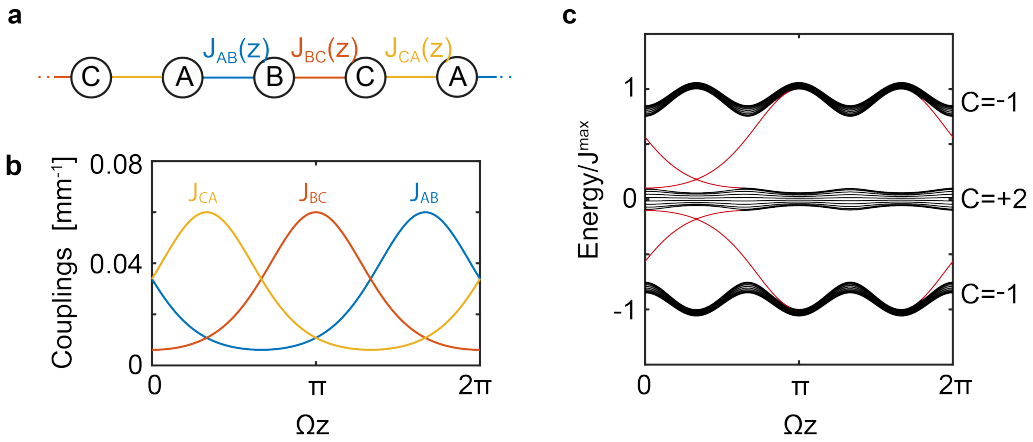

Figure 3.2. Photonic implementation of a topological Thouless pump. a, Schematic illustration of a Thouless pump model with three sites (A,B,C) per unit cell and z-dependent couplings between neighboring sites. **b**, Evolution of the couplings during one driving period. **c**, Band structure calculated with open boundary conditions showing three bands with Chern numbers $C = \{-1, 2, -1\}$. Red lines denote localized edge states.

of the instantaneous Hamiltonian (calculated for an array of 30 waveguides with open boundary conditions) are calculated and plotted. The band structure shows three bands with Chern numbers C={-1, 2, -1} connected via topological end states (red). A schematic illustration of a realization in a one-dimensional array of evanescently coupled waveguides is shown in Fig. 3.1a. The modulation of the coupling is achieved by periodically modulating the waveguide positions and therefore changing the spatial overlap of neighbouring waveguide modes. The position of waveguide n in the transverse direction is given by $x_n(z) = n \cdot d + \delta \cos(2\pi n/3 + \Omega z + \alpha_0)$ with d being the average separation between two waveguides, δ the spatial modulation strength and α_0 an initial phase. The white-light micrograph in Fig. 3.1b shows the output facet of a waveguide array with six out of ten unit cells.

3.3 Numerical Propagation Simulations

Using this Thouless pump, we demonstrate the differences between linear and nonlinear quantized pumping in three distinct regimes with different powers: (1) a low-power, linear regime in which the wavefunction evolves according to the linear Schrödinger equation; (2) an intermediate-power regime in which we observe the formation of a soliton that is pumped by a fixed number of unit cells during a pump period; and (3) a high-power regime in which we observe a trapped soliton. We refer to the three regimes as the

linear, pumped and trapped regimes, respectively. Numerical propagation simulations of equation (2) with a 4th-order Runge-Kutta scheme are shown in Fig. 3.3 for three periods. We use periodic boundary conditions; the number of waveguides exceeds the number of waveguides shown.

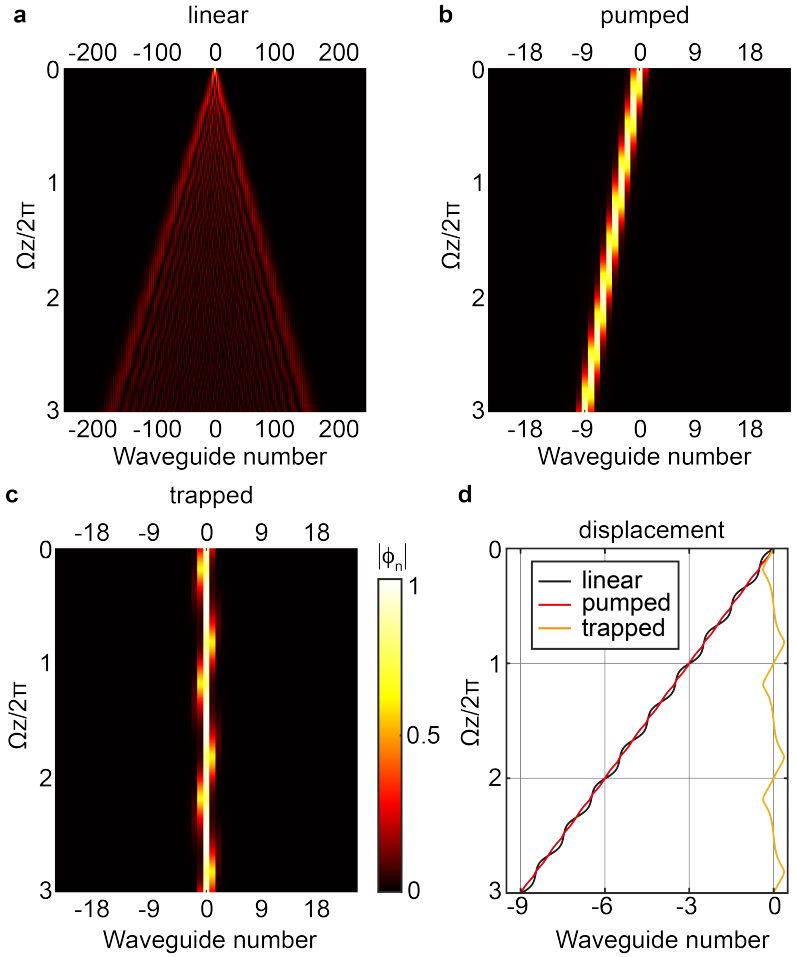

Figure 3.3. Linear and nonlinear propagation in topological Thouless pumps. a, Normalized amplitude of the discrete wavefunction, $|\phi_n|$, for a linear evolution over three periods for an input state with uniform excitation of the lowest band (chosen as a maximally-localized Wannier state). It develops a discrete diffraction pattern, while its centre of mass is being pumped to the left by three unit cells after three periods. **b**, Nonlinear evolution for a pumped soliton with a degree of nonlinearity $gP/J^{\max} = 1.9$. The excitation is an instantaneous nonlinear eigenstate (that is, a soliton) of the system. **c**, Same as **b** but with $gP/J^{\max} = 2.1$ and showing a trapped soliton. **d**, Displacement of the centre of mass for the cases shown in **a-c**. The parameters for all figures are d=22 μm, δ=2 μm, α_0=–2π/12 and Ω=2π/L with L=8,000 mm.

In the linear regime (Fig. 3.3a) the excitation is chosen as a maximally-localized Wannier state of the lowest band with Chern number $C = -1$ (see Fig. 3.2c) that

uniformly populates all Bloch states within that band. This occupation is analogous to a low temperature Fermionic system with the Fermi level in a bandgap, as is necessary for quantized pumping. Owing to diffraction, the wavefunction spreads during evolution, showing two dominant outer lobes similar to diffraction in a trivial array of straight waveguides. The bulk topological properties of the model are manifested in the transverse displacement of the centre of mass by C times the lattice constant (see also Fig. 3.3d).

Characteristic nonlinear behaviour (at a power at which we may clearly see the formation of discrete solitons) is displayed in Fig. 3.3b and c. In both cases, the excitation is a nonlinear eigenstate (that is, a soliton) of the instantaneous nonlinear Hamiltonian, which bifurcates from the lowest band and is found using Newton's method or a self-consistent algorithm (for more information see Appendix B). Here, bifurcation from a band means means that in the low-power limit the nonlinear eigenvalue of the soliton approaches the band from which it bifurcates. Thus the soliton can be clearly identified with a single band. In this limit the soliton can be approximated as the lowest Bloch state within that band multiplied with a hyperbolic secant envelope function. We point out that bifurcation from a band does not imply a uniform band occupation, but instead the projection of the soliton wavefunction onto the linear Bloch states is a strong function of power. The difference between the pumped regime (Fig. 3.3b) and the trapped regime (Fig. 3.3c) is dictated by the amount of power injected into the system, $gP/J^{\max} = 1.9$ and $gP/J^{\max} = 2.1$, respectively. In both regimes, a suppression of spatial diffraction due to the focusing Kerr nonlinearity is observed. Although the shape of the wavefunction changes during one period, it remains strongly peaked and reproduces itself after each period, so that its shape resembles the shape of the input state. In the pumped regime (Fig. 3.3b), the wavefunction travels across the lattice with a displacement identical to the Chern number of the band from which it bifurcates ($C = -1$). After each period, the soliton is displaced by three lattice sites (one unit cell), which can be clearly seen in Fig. 3.3d. At high power (Fig. 3.3c), the nonlinearly induced potential effectively decouples the waveguide and the wavefunction is trapped within the single site into which it was injected: the soliton's centre of mass oscillates around one lattice site (Fig. 3.3d), but never crosses onto another site. After each cycle the trapped soliton ends up in the starting position. The solutions shown in Fig. 3.3b and c are the pumped and trapped solitons, respectively.

We find analogue behavior for higher bands. In particular, in Fig. 3.4 we contrast linear propagation and nonlinear soliton propagation related to the middle band over three periods, showing distinct differences in the band projections. In the linear regime

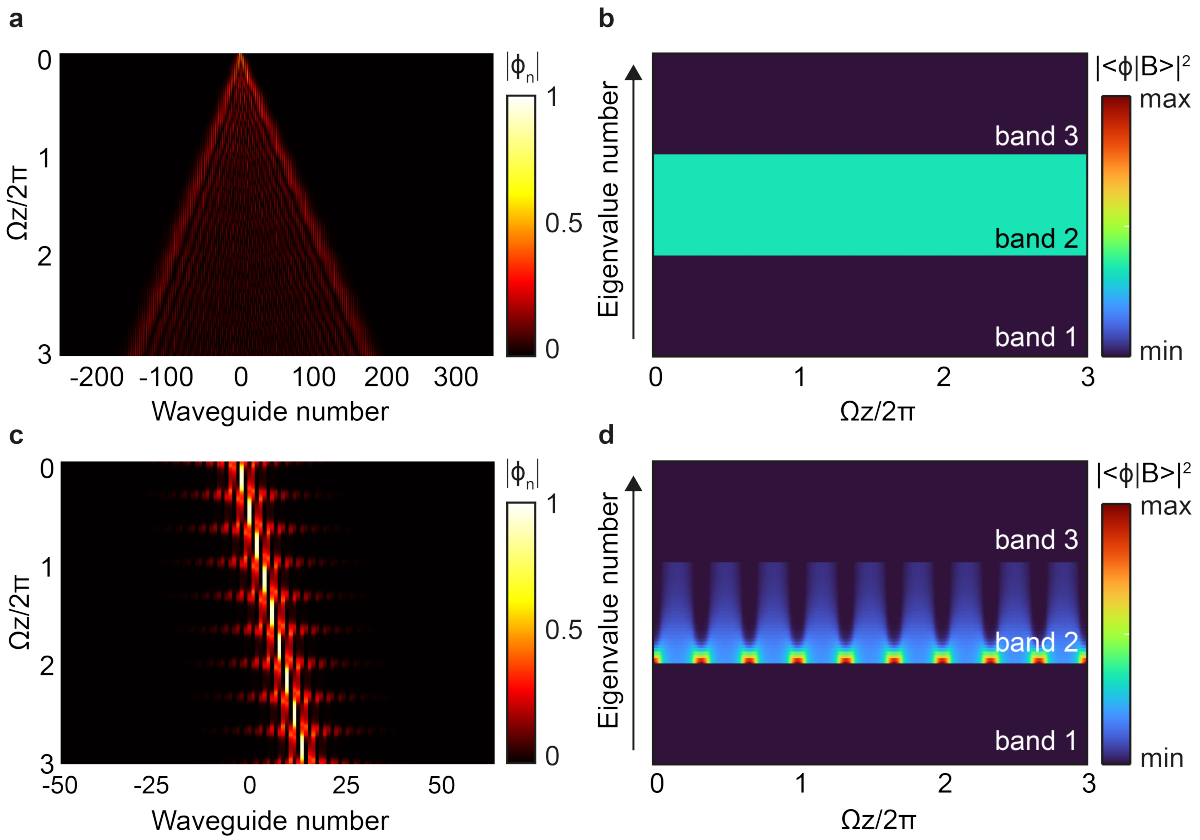

Figure 3.4. Linear and nonlinear higher band Thouless pumping. **a**, Numerically calculated z-evolution for an initial excitation of a maximally-localized Wannier state of the middle band. The displacement of the centre of mass is dictated by the Chern number of the occupied band ($C = +2$). **b**, Uniform projection of the propagated wavefunction, $\psi(z)$, in **a** onto the instantaneous Bloch states, $B(z)$, of the linear Thouless pump, with increasing energy from bottom to top. **c**, Similar to **a**, but with an initial excitation of a nonlinear eigenstate bifurcated from the middle band with $gP/J^{\max}$=0.2. The displacement of the centre of mass is identical to the Chern number of the band from which the soliton bifurcates ($C = +2$). **d**, Projection of the propagated soliton onto the instantaneous Bloch states of the linear Thouless pump. The projection shows a strongly nonuniform occupation of the linear Bloch states. Parameters for the system are chosen to be identical to those in Fig. 3.3, except L=4×10^3 mm with a size of 900 sites for **a**,**b** and L=8×10^5 mm for **c**,**d**.

(Fig. 3.4a) the excitation is chosen to be a maximally-localized Wannier function of the middle band. By definition, this initially ensures a uniform band occupation of the respective band. Analogue to Fig. 3.3a, we then numerically evolve the wavefunction over three periods and choose the modulation frequency such that the adiabatic theorem applies and excitations between bands are negligible. Due to translation symmetry, coupling between states within the same band are forbidden. Thus, the occupation of the middle band stays uniform over the entire pumping cycle, as shown in Fig. 3.4b.

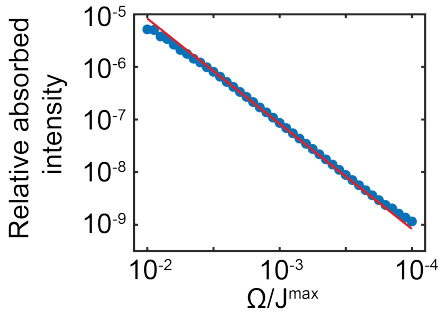

Figure 3.5. Adiabaticity of soliton pumping. Absorbed intensity (relative to the total intensity) during one driving period in relation to the driving frequency. Blue circles are numerical values and the red line has a slope of -2. The parameters for the simulation are 180 sites with absorbing boundary conditions using 40 sites at each end, d=24μm, δ=2μm, α_0=$-2\pi/12$ and $gP/J^{\max}$=1.9.

During propagation, the wavefunction diffracts and the centre of mass is displaced (in units of the lattice constant) by the Chern number of the uniformly excited band, which is +2 for the middle band.

In contrast, Fig. 3.4c and d show the nonlinear propagation and band projection, respectively, when the system is initially excited with an instantaneous soliton, that bifurcates from the middle band. Analogue to Fig. 3.4b the wavefunctions stays localized during the nonlinear propagation, but is displaced by +2 unit cells after each period, corresponding to the Chern number of the band from which the soliton bifurcates. We find those solitons using Newton's method (see Appendix B) and use a maximally-localized Wannier state of the respective band as initial guess. The strength of the nonlinearity is $gP/J^{\max}$=0.2, one order of magnitude lower than used for Fig. 3.3. We choose a lower power compared to Fig. 3.3, as we find that solitons from higher bands become unstable at higher input power. Owing to the lower power, the solitons extend over several unit cells during propagation and mainly occupy the lowest-energy eigenstate. The overlap of the soliton's wavefunction with the instantaneous linear Bloch states (Fig. 3.4d) unequivocally shows a distinctly nonuniform occupation of any band, that is furthermore power dependent.

The displacement of the wavefunction's centre of mass in the linear case is well understood and arises from a uniform occupation of a topologically nontrivial band. The same principle is responsible for quantized charge transport in Fermionic pumps even when disorder and interparticle interactions are present [30]. In stark contrast, here, the projection of the pumped soliton state onto the complete set of linear Bloch states does not show a uniform occupation of any band; indeed, the occupation is a strong function

of power. This means that the band occupation (to the extent that it is meaningful in this nonlinear system) is nonuniform and non-universal; thus quantized soliton motion is dictated by the band from which it bifurcates, rather than by the population within each band. Not surprisingly, propagation with the same input wavefunction but in the linear regime does not show quantized pumping. In the nonlinear regime we find numerically that the input soliton 'tracks' the instantaneous localized stable soliton solutions at every value of z during propagation. In other words, it behaves much as an eigenstate would in a linear time-varying, but adiabatic, system, despite being a fundamentally nonlinear entity. Strictly speaking, these solitons radiate because of the z-dependence of the Hamiltonian. To show that nonlinear Thouless pumps, similarly to linear pumps, have an adiabatic regime and therefore show perfectly quantized pumping in the adiabatic limit, we numerically evaluate the intensity radiated by the soliton during propagation. We use a system of 180 sites and numerically calculate the remaining intensity with absorbing boundary conditions on 40 waveguides at each end. We find that the radiated intensity is proportional to Ω^2 (see Fig. 3.5) and therefore becomes negligible for $\Omega \to 0$. This agrees with the results of Ref. [104, 105], which proposes this as a nonlinear version of the adiabatic theorem. Thus, we can analyse the pumped and trapped solitons in terms of instantaneous nonlinear eigenstates.

3.4 Nonlinear bifurcations as phase transition

To explain the mechanism of pumping, we examine the position of the centres of mass of instantaneous solitons found at each time slice, z, as shown in Fig. 3.6a-d. The instantaneous nonlinear eigenstates (solitons) are obtained using a Newton iteration scheme. For that purpose, we use the FindRoot function in Mathematica [106] (with a precision of more than 15 digits). This method depends critically on the initial ansatzes. At high power, $gP/J^{\max} = 5$, we use six different ansatzes to evaluate the relevant soliton eigenstates, belonging to six different branches. Three of the initial ansatzes are localized on a single site, while the other three ansatzes are localized between two sites with equal intensity in two neighbouring sites. We then iteratively use the solitons at higher power as ansatzes for lower power.

We see that in Fig. 3.6a, in the pumped regime ($gP/J^{\max} = 1.5$), the soliton solutions follow a contiguous path through the lattice. For this power, we find a soliton solution (per unit cell), which is displaced along its path by one unit cell. For higher power ($gP/J^{\max} = 1.9$, Fig. 3.6b), new nonlinear eigenstates emerge via saddle-node nonlinear

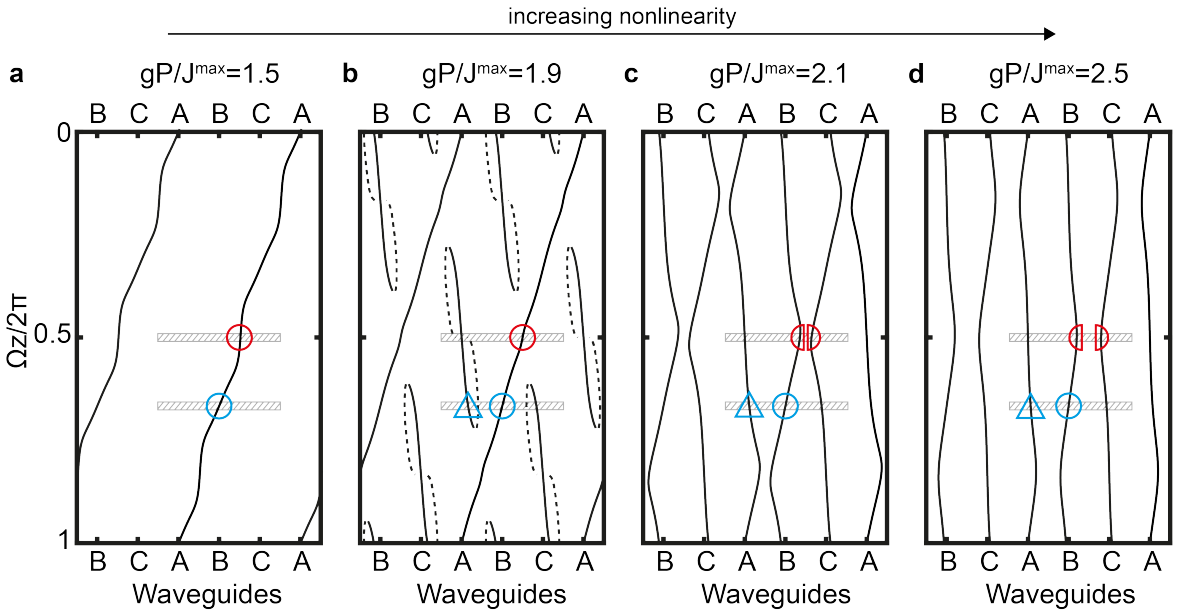

Figure 3.6. Mechanism of nonlinear pumping. a-d, Centres of mass of available soliton solutions at each value of z in the pump cycle, showing contiguous paths. Black solid (dashed) lines indicate the position of the centre of mass for stable (unstable) nonlinear eigenstates of the instantaneous Hamiltonian. Gray-hatched areas at $\Omega z/2\pi$=0.5 and $\Omega z/2\pi$=2/3 illustrate the positions for which the bifurcation diagrams in Fig. 3.7 are calculated. Blue and red symbols label specific soliton positions of different branches, as shown in Fig. 3.7**a**,**b**. Each lattice consists of 30 sites and the parameters are the same as in Fig. 3.3.

bifurcations (see Fig. 3.7b; for a classification of bifurcations see, for example, chapter 21 in Ref. [107].) However, at this power, these bifurcations do not divert the original path of the soliton. In contrast, for still higher power ($gP/J^{\max}$=2.1, 2.5, Fig. 3.6c and d, respectively), a pitchfork bifurcation (see Fig. 3.7a) of nonlinear eigenstates, associated with a spontaneous symmetry breaking, gives rise to the splitting of the path of the soliton's centre of mass, causing it to return to the site from which it started at the beginning of the cycle. A depiction of the centres of mass of the bifurcating nonlinear solutions as a function of power, including the pitchfork and the saddle node bifurcation, are shown in Fig. 3.7a,b, and a clear animation of this process can be seen in Supplementary Video 2 in Ref. [99].

As we have described, owing to the periodic Hamiltonian, the nonlinear eigenstates at the beginning and end of each pump cycle are identical, and, owing to translation invariance, exist for each unit cell. During adiabatic evolution, the soliton then tracks these eigenstates and when coming back to the beginning of a pump cycle, the soliton is forced to occupy the initial state either in the same unit cell or displaced by an integer

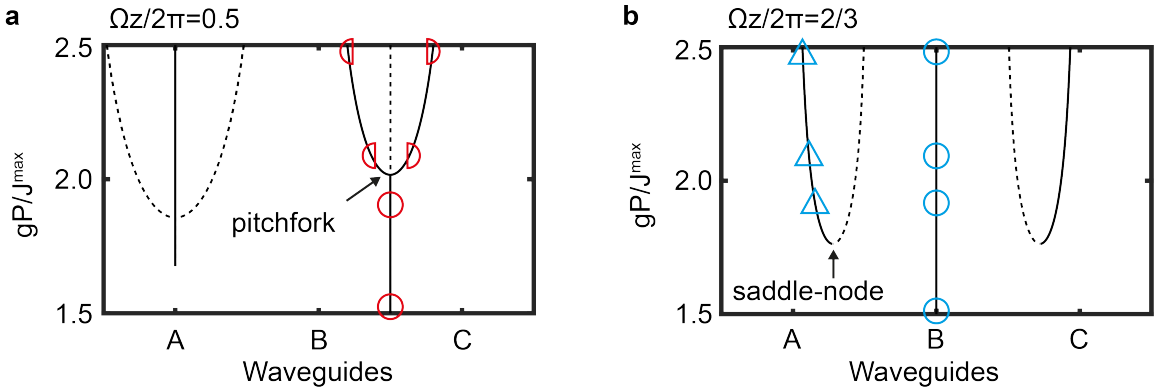

Figure 3.7. Nonlinear bifurcations. a,**b**, Bifurcation diagrams for the nonlinear eigenstates at $\Omega z/2\pi$=0.5 (**a**) and $\Omega z/2\pi$=2/3 (**b**), as a function of power. Blue and red symbols label specific soliton positions of different branches, as shown in Fig. 3.6 **a-d**.

number of unit cells. In our model the Hamiltonian takes on the same form after 1/3 (2/3) of one full period, including a translation by one (two) sites. This allows us to observe quantized pumping of single sites as well, in addition to integer unit cells.

Although no topological invariants are known for nonlinear systems, we can a posteriori define a topological invariant for nonlinear pumping. To that end, we define an extended unit cell such that the exponential tails of the localized soliton become negligible within it. We then solve for periodic evolution of the soliton therein and include the potential induced by the nonlinearity as a linear potential in the Hamiltonian. With this, we are able to calculate the Chern number using the techniques of Ref. [108] for the band describing the soliton evolution, which is C=-1 for the cases shown in Fig. 3.6a,b and C=0 for those in Fig. 3.6c,d.

In Fig. 3.8 we show such calculated Chern numbers for the soliton when tuning the system through a nonlinearly induced topological phase transition (by increasing the power) as well as through a linear topological phase transition (by changing the hopping strength). We find that the nonlinear topological transition is not instantaneous as it is not associated with a linear gap closing point. Instead, there exists a transition region, in which pumping with no quantization is observed. The width of the transition region is model dependent, but follows the same principle: For a range of power values above the pitchfork bifurcation threshold (that splits the path) and below the threshold power to form a new contiguous path (e.g. for the trapped soliton), no contiguous trajectory exists. In this region the soliton follows its stable instantaneous soliton trajectory until, at some point during the pumping cycle, the soliton becomes unstable and diffracts.

We observe a different picture for linear topological phase transitions. To tune

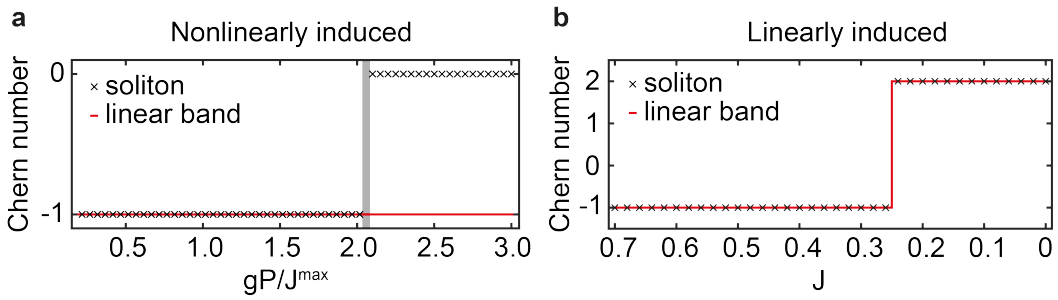

Figure 3.8. Linear and nonlinear phase transitions. **a**, Nonlinearly induced topological phase transition. The Chern number associated with the soliton is calculated for increasing power $gP/J^{\max}$. In the grey area, no contiguous path for an adiabatic soliton evolution is found. The red line indicates the Chern number of the lowest band in the linear model from which the soliton bifurcates. **b**, Linearly induced topological phase transition. The Chern number associated with the soliton is calculated as a function of decreasing hopping strength J. The red line indicates the linear Chern number of the band from which the soliton bifurcates. The topological phase transition occurs at $J = 0.25$.

the off-diagonal AAH model through a (standard linear) topological phase transition, we parameterize the (dimensionless) nearest-neighbour couplings in the following way: $J_n(z) = J + K \cdot \cos(2\pi n/3 + \Omega z + 2\pi/6)$, with $K = 1$. For $J > 0.25$ the system is topologically equivalent to the model described before, having Chern numbers of $C = \{-1, 2, -1\}$. For $J = 0.25$ a gap closing occurs, changing the Chern numbers to $C = \{2, -4, 2\}$ for $J < 0.25$ [64]. We calculate the Chern number associated with the soliton propagation for a soliton (with $gP/K = 0.7$), which bifurcates from the lowest linear energy band, while sweeping downward from $J = 0.7$ to $J = 0$ and therefore through a linear topological phase transition. Figure 3.8b shows that the soliton is pumped by the Chern number of the band from which it bifurcates and changes its behaviour at the topological phase transition point, when the Chern number of the lowest band itself changes from -1 to +2. We expect the transition point of soliton pumping and the Chern number change to coincide exactly in the limit of low power, but this is difficult to numerically verify as the the calculation of solitons is challenging at extremely low power. For increasing soliton power, we observe increasing (but small) deviations between the linear phase transition and the soliton behavior.

3.5 Experimental Observation

We experimentally probe the three regimes (linear, pumped and trapped) in a one-dimensional laser-written array of evanescently coupled waveguides [76,78] with a focusing Kerr nonlinearity, which is present owing to the ambient borosilicate glass. To reach the necessary degree of nonlinearity, we launch intense laser pulses into single waveguides, mostly exciting the soliton. To reduce additional, unwanted nonlinear effects, especially the generation of new wavelengths via self-phase modulation, the pulses are temporally stretched to 2 ps and down-chirped accordingly. As a result, 76% of the pulse intensity (equivalent to the full-width at half-maximum (FWHM) of a Gaussian) is found in a range of 20 nm for input powers up to 6 mW (see also Refs. [36, 38] and Appendix C). The wavelength-dependent change in the couplings is therefore similar to the intrinsic coupling strength uncertainty $\Delta J/J \approx \pm$ 10% [99]. For the maximum propagation length of the waveguide arrays used in our experiments, chromatic dispersion effects can be neglected. The losses in the waveguides are about 0.7 dB cm^{-1} and independent of power. Under these conditions, we can approximate the dynamics in our system with the nonlinear Schrödinger equation (see Eq. (3.2)).

In separate experiments, we observe nonlinear soliton pumping by one, two and three sites. Figure 3.9a-c shows the observed waveguide occupancies at the output facet. We use (time-averaged) optical input powers of $\langle P\rangle_t$=$\{0.1, 2.0, 3.5, 5.0, 6.0\}$ mW, which we convert into $gP/J^{\max}$ for each individual experiment with g=$(0.07\pm0.01)\,\mathrm{mm}^{-1}$ per mW of (time-averaged) input power (see Fig. 2.6d). For low power ($gP/J^{\max}$=0.1 and 0.2), linear diffraction is observed and the intensity spreads over several sites. The displacement of the centre of mass is not quantized, because the single-site excitation does not uniformly populate a band. For increasing input power, we observe strong localization of the wavepacket caused by soliton formation (blue arrow): this is the pumped regime. A further increase in the input power causes light to strongly localize in the waveguide into which it was injected (green arrow): this is the trapped regime. This transition from linear diffraction to a pumped soliton and finally to a trapped soliton is the experimental signature of quantized nonlinear pumping.

For the corresponding simulations in Fig. 3.9d-f, we scaled the coupling function using the linear propagation in the individual array and included realistic optical losses (measured to be approximately 0.7 dB cm^{-1}). Owing to the losses, the power thresholds to observe the pumped and trapped soliton are higher than those in the idealized lossless case (Fig. 3.3 and 3.6). In Fig. 3.9, simulations that take into account such loss agree well

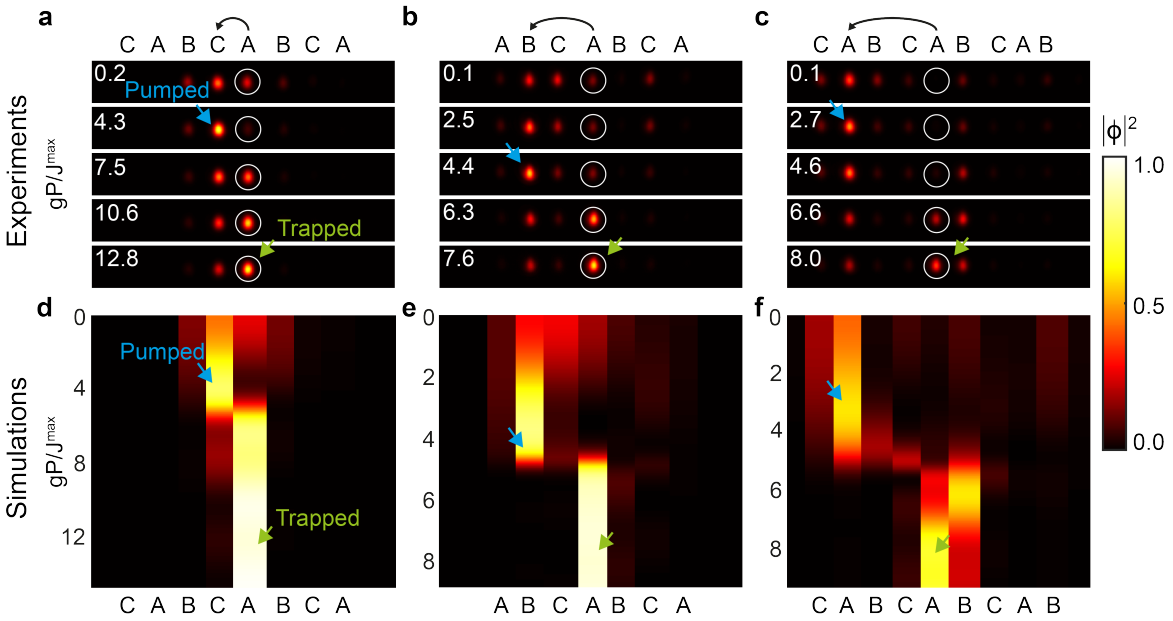

Figure 3.9. Experimental observation of quantized nonlinear topological pumping. **a**, Experimentally observed normalized intensity pattern at the output facet of a 76-mm-long waveguide array consisting of 30 waveguides (d=24 μm, δ=2 μm) after 1/3 of a full period. White circles denote the excited waveguide; input power increases from top to bottom. The blue arrow denotes the observation of the pumped soliton; the green arrow shows the trapped soliton. **b**, Same as a except for an array covering 2/3 of a full pumping period (d=23 μm, δ=2 μm). **c**, Same as a except for an array covering one full pumping period (d=21 μm, δ=1 μm). **d-f**, Corresponding nonlinear tight-binding simulations for **a-c**, respectively, including propagation loss.

with the experimental results. The lower contrast in the experiment arises from the fact that the tails of the pulse (in time) propagate linearly and diffract, while only the region of high power in the temporal centre of the pulse is affected by strong nonlinearity [36]. Nonetheless, the pumped soliton and a transition to a trapped soliton is clearly observed in simulation and experiment.

Finally, we also experimentally confirm our theoretical prediction that the trapping of the soliton is due to a pitchfork bifurcation (as shown in Fig. 3.7a). We measure the output power in the waveguide in which we expect the pumped soliton to be localized as a function of input power. Once the pumped soliton appears, a further increase of the input power leads to an increase of the peak power of the pumped soliton (when the wavefunction is normalized to the total power) owing to the soliton's stronger confinement. For a sufficiently high input power, the pitchfork bifurcation is triggered. At this point, the power in the waveguide where the pumped soliton is localized decreases relative to

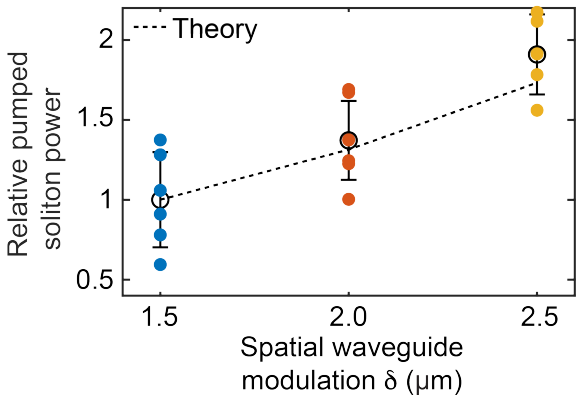

Figure 3.10. Parameter dependence of pitchfork bifurcation. Input power (relative to the mean input power at modulation δ=1.5 μm) required for maximum relative intensity in the pumped soliton as a function of spatial modulation strength δ of the waveguides. Dots in colour are measurements, black lines are the respective mean values with one standard deviation. The black dotted line shows the numerically obtained threshold power for the pitchfork bifurcation point.

that in the injected waveguide. This point marks the onset of trapping, and thus the appearance of the pitchfork bifurcation. We can test the dependence of this threshold power on the spatial modulation strength δ. We measure the threshold power for three different arrays with varying δ, as well as in six different unit cells within the same waveguide array (with the same δ). In Fig. 3.10, we plot the experimentally obtained optical input power required to observe the onset of trapping, as a function of the degree of waveguide modulation, δ. We compare this to the numerically obtained power for which the pitchfork bifurcation occurs. To directly compare the two, we normalize the power to unity at $\delta = 1.5$ μm; on this basis, clear agreement between theory and simulation is observed.

3.6 Conclusion and Outlook

In summary, our results show the emergence of quantization in interacting topological systems described via nonlinearities in the mean-field limit. We theoretically proposed and experimentally observed integer quantized soliton Thouless pumping, that is, a self-forming localized state shows quantized pumping despite a nonuniform band projection. Using evanescently coupled waveguides, we directly observed soliton pumping by 1/3, 2/3 and one full unit cell after (1/3, 2/3 and one full pumping cycle), corresponding to a Chern number of -1. At high optical power, we observe a transition to a trapped soliton, caused by spontaneous symmetry-breaking nonlinear bifurcations. We found

that quantized soliton pumping applies to all bands, in particular we find solitons that bifurcate from higher bands and are pumped by the Chern number of the respective band, e.g. by more lattice constants and against the modulation direction.

We anticipate this work to be a starting point for the exploration of topologically quantized transport in nonlinear and interacting systems. Possible future directions of interest are quantized nonlinear pumping in higher-order topological systems, as well as a complete understanding of the dynamics of Thouless pumping in systems with interactions on the few-particle level. The perhaps most pressing question at this point will be answered in the next chapter: Is it a general rule that solitons pump by the Chern number of the band from which they bifurcate or is it model dependent?

Chapter 4
Analytical proof of quantization of soliton Thouless pumping

This chapter is purely theoretical and presents an analytic proof that the pumping of low-power solitons in Thouless pumps is dictated by the Chern number of the band from which they bifurcate. By expanding the discrete nonlinear Schrödinger equation in the Wannier basis, we show that the trajectory of stable solitons tracks the position of Wannier states. Hence, soliton pumping is quantized by the Chern number which can thus be considered to be a physically meaningful topological invariant for describing nonlinear systems. Finally, we show quantized pumping in 2+2 dimensions. This chapter is based on work that was done in collaboration with Mikael C. Rechtsman and has been published[1] in Ref. [109].

4.1 Introduction

In the previous chapter, we have theoretically described and experimentally observed quantized nonlinear Thouless pumping via soliton motion despite nonuniform band occupation [99]. The quantization followed from the fact that the Hamiltonian of a Thouless pump is time periodic and thus comes back to itself after a period. For an adiabatic modulation, in which the propagation is dictated by the instantaneous solitons, this implies that the soliton wavefunction must – in the low-power regime – return to itself (apart from a translation by an integer number of unit cells) as the same solitons exist at the beginning and end of each pumping cycle. We observed experimentally and numerically that solitons bifurcating from a given band are transported in accordance with the Chern number of that band. However, no proof for the amount of pumping was

[1] Copyright (2022) by The American Physical Society.

provided and a comprehensive theoretical understanding of this effect has not yet been presented.

Our goal is to predict if, under what conditions, and by what amount a soliton is pumped, and to define a topological invariant for the nonlinear system. This is a highly challenging task due to the lack of a broad theoretical framework for topological invariants and associated physical observables in any interacting system. One approach that comes to mind is to calculate the many-body Chern number using twisted boundary conditions. This requires full knowledge of the wavefunction, which means that we have to solve first for the propagation before we can use the propagated wavefunction to calculate the topological invariant. Therefore, it has no predictive power. In the previous chapter we used a similar approach and calculated the Chern number for the linearized system that included the nonlinearly-induced on-site potential. Similarly, this approach lacks predictive power as the propagation already has to be solved before attempting to calculate the invariant. Thus, an entirely new approach is needed.

In our approach we restrict ourselves to low-power solitons and show that their trajectories are dictated by the Chern number of the band from which they bifurcate. During an adiabatic modulation a stable soliton remains a soliton of the instantaneous Hamiltonian. Hence, it is sufficient to show the existence of a stable soliton for all times, and that its position is linked to the position of the Wannier states. Specifically, we solve for the instantaneous solitons in the basis of Wannier functions, in which the equations take the form of a simple one-dimensional lattice with Kerr nonlinearity. We illustrate the resulting quantization in a Rice-Mele model. For each band we find a stable instantaneous soliton centered upon a Wannier function for all times during the pump cycle. Additionally, we find an unstable soliton centered between two Wannier functions. Finally, we show quantized nonlinear pumping in a 2+2-dimensional pump.

4.2 The Wannier function picture

In this chapter we revert to using time t instead of propagation distance z, as no experiments are presented and Thouless pumps were originally defined with modulations in time. Of course, all results are independent of this change of variables. Our focus lies on systems with a slowly varying, time-periodic Hamiltonian describing a (linear) Thouless pump. The pump is entirely general at this stage; later we illustrate the results in a Rice-Mele model. The time dynamics are described by the discrete nonlinear Schrödinger equation with a focusing Kerr nonlinearity [88, 110] (although the results

generalize straightforwardly to localized-bright-solitons in the discrete defocusing case),

$$i\frac{\partial}{\partial t}\phi_n(t) = \sum_m H_{n,m}(t)\phi_m(t) - g|\phi_n(t)|^2\phi_n(t). \tag{4.1}$$

Here, $\phi_n(t)$ is the amplitude of the wave function at site n and time t, $H_{n,m}(t)$ is a time-periodic tight-binding Hamiltonian and $g > 0$ is the strength of the focusing nonlinearity. For our analysis it does not make a difference if $H_{n,m}$ describes hoppings between sites or orbitals on a given site. Thus, we refer to both as sites. The indices n and m run over all sites with periodic boundary conditions. As already mentioned in the previous chapter, Eq. (4.1) describes a range of systems, including the propagation of intense light through nonlinear media [88, 110], the dynamics of Bose-Einstein condensates [111], and exciton-polariton condensates [112–114]. It conserves the norm of the wave function ($P = \sum_n |\phi_n|^2$) and, without loss of generality, in this chapter, we use normalized wave functions ($P = 1$) and vary g. The degree of nonlinearity is then given by g with respect to the hopping parameters in $H_{n,m}$. We refer to solitons as having "low power" if they are calculated with small g/J.

In the linear case ($g = 0$), quantized Thouless pumping necessarily requires adiabatic time modulation and uniform band occupation. For fermionic systems (like electrons in the solid state), this corresponds to a Fermi level within a bandgap. For bosonic systems, a simple way to obtain uniform band filling is via the initial excitation of a single Wannier function. Over time, the wave function will evolve but retain a uniform band occupation throughout the pump cycle as dictated by the adiabatic theorem. Quantized pumping itself can be understood as the flow of the instantaneous Wannier functions, as displayed in Fig. 4.1a and b, whose winding around the unit cell as a function of the pump parameter is equivalent to the Chern number of the occupied band (see also Chapter 2.2.3).

In the nonlinear case ($g \neq 0$), the time evolution of stable solitons (i.e., nonlinear eigenstates) has similarities to the adiabatic time evolution of eigenstates in linear systems [104, 105]: For sufficiently slow driving, excitations of other states are negligible and the wave function continues to occupy the instantaneous soliton for all times during the pump cycle. It is therefore possible to calculate the adiabatic time evolution for solitons in two ways: (1) numerically solving Eq. (4.1) as a function of time or (2) solving for the instantaneous nonlinear eigenstates at different time slices in the pump cycle. Importantly, the instantaneous states must be stable, as otherwise small perturbations around the linearized solution exponentially increase (see Appendix B

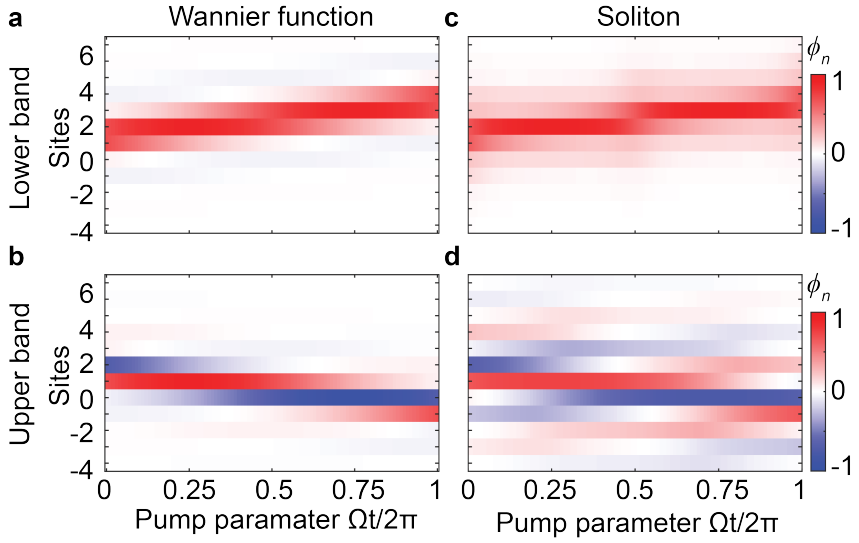

Figure 4.1. Wannier states and soliton functions. **a**, Instantaneous maximally-localized Wannier wave function for one pump cycle calculated for the lower band in a Rice-Mele model with Chern number C=+1. **b**, Similar to **a**, but calculated for the upper band with a Chern number of C=-1. **c**,**d** Similar to **a** and **b**, but showing the instantaneous soliton wave function. The degree of nonlinearity is g/J=2 and g/J=3 for **c** and **d**, respectively.

for more information on linear stability analysis). We illustrate the second method in Fig. 4.1c and d, which show the wave function of instantaneous solitons. Strikingly, the trajectories of the instantaneous solitons are noticeably similar to those of the instantaneous Wannier functions of the bands from which the solitons bifurcate. As the available solitons at the beginning and at the end of each pump cycle are identical in each unit cell, quantized motion of solitons is expected, even for nonuniform band occupation [99]. Below, we prove that the number of unit cells which the solitons are pumped corresponds to the Chern number of the band from which they bifurcate.

4.3 Derivation of the Discrete Nonlinear Schrödinger Equation in Wannier basis

We now present the missing link to show that the position of the instantaneous soliton is indeed intimately related to that of the Wannier functions. Showing that the solitons pump by the same number of unit cells as the Wannier functions will prove that the solitons are transported by C unit cells, where C is the Chern number. As we are only concerned with finding the instantaneous solitons for a static Hamiltonian at a given point in the pump cycle, we use $\phi_n(t) \rightarrow e^{-i\lambda t}\phi_N$, where λ is the nonlinear eigenvalue,

such that Eq. (4.1) takes the following form:

$$\lambda\phi_n = \sum_m H_{n,m}\phi_m - g|\phi_m|^2\phi_m. \tag{4.2}$$

We first rewrite Eq. (4.2) in the basis of Wannier functions as in Ref. [115] by expanding the wave function in the Wannier basis,

$$\phi_n = \sum_{\mathbf{R},\alpha} c_{\mathbf{R},\alpha} w_{\mathbf{R},\alpha,n}, \tag{4.3}$$

with expansion coefficients $c_{\mathbf{R},\alpha}$ and Wannier functions $w_{\mathbf{R},\alpha,n}$ that are labelled by the lattice vector $\mathbf{R}$ and a band index α. Wannier functions form a complete and orthonormal set:

$$\sum_n w^*_{\mathbf{R}',\alpha',n} w_{\mathbf{R},\alpha,n} = \delta_{\mathbf{R}',\mathbf{R}}\delta_{\alpha',\alpha}. \tag{4.4}$$

Furthermore, the Wannier states form Fourier pairs with the Bloch states, $B_{k,\alpha,n}$, which are labelled by the crystal momentum $\mathbf{k}$:

$$w_{\mathbf{R},\alpha,n} = \frac{1}{\sqrt{N}} \sum_{\mathbf{k}} e^{-i\mathbf{k}\mathbf{R}} B_{\mathbf{k},\alpha,n}, \tag{4.5a}$$

$$B_{\mathbf{k},\alpha,n} = \frac{1}{\sqrt{N}} \sum_{\mathbf{R}} e^{i\mathbf{k}\mathbf{R}} w_{\mathbf{R},\alpha,n}. \tag{4.5b}$$

Bloch states form the energy eigenstates of the linear Hamiltonian, $H_{n,m}$, with eigenenergy $E_{\mathbf{k},\alpha}$ and obey the following eigenvalue equation:

$$E_{\mathbf{k},\alpha} B_{\mathbf{k},\alpha,n} = \sum_m H_{n,m} B_{\mathbf{k},\alpha,m}. \tag{4.6}$$

More information on the Wannier basis can be found in Chapter 2.2 and in Appendix A.

Replacing the wave function in Eq. (4.2) via Eq. (4.3), multiplying from the left with $w^*_{\mathbf{R}',\alpha',n}$, summing over all sites, and using the orthogonality relation of Wannier functions (Eq. (4.4)), results in:

$$\lambda c_{\mathbf{R}',\alpha'} = \sum_{\mathbf{R},\alpha} c_{\mathbf{R},\alpha} \sum_{n,m} w^*_{\mathbf{R}',\alpha',n} H_{n,m} w_{\mathbf{R},\alpha,m} - \sum_{\substack{\mathbf{R},\mathbf{R}'',\mathbf{R}''' \\ \alpha,\alpha'',\alpha'''}} g W^{\alpha,\alpha',\alpha'',\alpha'''}_{\mathbf{R},\mathbf{R}',\mathbf{R}'',\mathbf{R}'''} c^*_{\mathbf{R},\alpha} c_{\mathbf{R}'',\alpha''} c_{\mathbf{R}''',\alpha'''}, \tag{4.7}$$

where W is an overlap integral between four Wannier functions:

$$W^{\alpha,\alpha',\alpha'',\alpha'''}_{\mathbf{R},\mathbf{R}',\mathbf{R}'',\mathbf{R}'''} = \sum_n w^*_{\mathbf{R},\alpha,n} w^*_{\mathbf{R}',\alpha',n} w_{\mathbf{R}'',\alpha'',n} w_{\mathbf{R}''',\alpha''',n}. \tag{4.8}$$

The first term on the right-hand side of Eq. (4.7) can be simplified, using the Fourier series description of the band structure:

$$E_{\mathbf{k},\alpha} = \sum_{\tilde{\mathbf{R}}} e^{i\mathbf{k}\tilde{\mathbf{R}}} \epsilon_{\tilde{\mathbf{R}},\alpha}. \tag{4.9}$$

In the Thouless pumps under consideration $E_{\mathbf{k},\alpha}$ is real, periodic and even around $\mathbf{k} = 0$. It follows that $\epsilon_{\tilde{\mathbf{R}},\alpha} = \epsilon_{-\tilde{\mathbf{R}},\alpha} = \epsilon^*_{\tilde{\mathbf{R}},\alpha}$. Thus the Fourier series coefficients are a real and even function of $\tilde{\mathbf{R}}$. With this:

$$\begin{aligned}
&\sum_{\mathbf{R},\alpha} c_{\mathbf{R},\alpha} \sum_{n,m} w^*_{\mathbf{R}',\alpha',n} H_{nm} w_{\mathbf{R},\alpha,m} \\
&\quad = \sum_{\mathbf{R},\alpha,n} c_{\mathbf{R},\alpha} w^*_{\mathbf{R}',\alpha',n} \frac{1}{\sqrt{N}} \sum_{\mathbf{k}} E_{\mathbf{k},\alpha} e^{-i\mathbf{k}\mathbf{R}} B_{\mathbf{k},\alpha,n} \\
&\quad = \sum_{\mathbf{R},\tilde{\mathbf{R}},\alpha,n} c_{\mathbf{R},\alpha} w^*_{\mathbf{R}',\alpha',n} \epsilon_{\tilde{\mathbf{R}},\alpha} \frac{1}{\sqrt{N}} \sum_{\mathbf{k}} e^{-i\mathbf{k}(\mathbf{R}-\tilde{\mathbf{R}})} B_{\mathbf{k},\alpha,n} \\
&\quad = \sum_{\mathbf{R}} \epsilon_{\mathbf{R}'-\mathbf{R},\alpha'} c_{\mathbf{R},\alpha'},
\end{aligned} \tag{4.10}$$

where we have used Eq. (4.5a) and Eq. (4.6) for the first equality, Eq. (4.9) for the second and Eq. (4.5a) and Eq. (4.4) for the third. Plugging Eq. (4.10) into Eq. (4.7) directly gives

$$\lambda c_{\mathbf{R},\alpha} = \sum_{\mathbf{R}'} \epsilon_{\mathbf{R}-\mathbf{R}',\alpha} c_{\mathbf{R}',\alpha} - \sum_{\substack{\mathbf{R}',\mathbf{R}'',\mathbf{R}''' \\ \alpha',\alpha'',\alpha'''}} g W^{\alpha,\alpha',\alpha'',\alpha'''}_{\mathbf{R},\mathbf{R}',\mathbf{R}'',\mathbf{R}'''} c^*_{\mathbf{R}',\alpha'} c_{\mathbf{R}'',\alpha''} c_{\mathbf{R}''',\alpha'''}. \tag{4.11}$$

Up until now, no assumptions have been made and Eqs. (4.2) and (4.11) are equally valid to find static solitons, apart from the fact that they are written in different bases: ϕ_n describes the amplitude on individual real space sites, while $c_{\boldsymbol{R},\alpha}$ describes the amplitude of Wannier functions. We refer to the two descriptions as "real space" and "Wannier space," respectively. To proceed, we make the following reasonable simplifications: (1) We focus on static solitons at low power, whose occupation for isolated (nondegenerate) energy bands tends to be in one band only, due to the large energy difference separating the bands. Therefore, we can neglect any nonlinear inter-band coupling terms in Eq.

(4.11) and only focus on individual bands. (2) We restrict ourselves to systems that allow exponentially localized Wannier functions, such that the dominant term in the overlap integral is given by the Wannier functions localized at the same position, which applies to a Thouless pump at any given time slice. Then, the static discrete nonlinear Schrödinger equation takes the following fully simplified form in the Wannier basis:

$$\lambda c_{\mathbf{R},\alpha} = \sum_{\mathbf{R}'} \epsilon_{\mathbf{R}-\mathbf{R}',\alpha} c_{\mathbf{R}',\alpha} - g W^{\alpha,\alpha,\alpha,\alpha}_{\mathbf{R},\mathbf{R},\mathbf{R},\mathbf{R}} |c_{\mathbf{R},\alpha}|^2 c_{\mathbf{R},\alpha} \tag{4.12}$$

This equation has an intuitive interpretation: It describes hopping in a lattice with a Kerr nonlinearity, where the hopping strengths are given by the Fourier coefficients of the (linear) energy bands. In contrast to Eq. (4.2), the sites in this lattice do not represent sites in real space, but rather Wannier functions. Furthermore, and importantly, the unit cell in the Wannier space only consists of a single site. This allows us to use the knowledge about solitons in simple 1D lattices (see, for example, Refs. [88, 92, 95, 110]), where we already know that two types of static solitons exist: one stable on-site soliton and one unstable inter-site soliton (see also Fig. 4.3a). In Wannier space, the on-site soliton is always centered on a single Wannier function. After transforming back from Wannier into real space, the obtained real space soliton is localized near the Wannier center. (Its center of mass (c.m.) is not necessarily identical to the c.m. of the Wannier function due to interference effects between multiple occupied Wannier functions.) As this is valid for all times t during a pump cycle, and the on-site soliton is expected to be stable for all times, we have shown that the motion of the soliton is dictated by the motion of the Wannier centers. As the displacement of a Wannier center over a full cycle in a Thouless pump is equal to the Chern number of their respective band [58, 72, 73] (see also Chapter 2.2.3), the displacement of low-power pumped solitons is given by the Chern number of the band from which they bifurcate.

4.3.1 Example: Rice-Mele model

To numerically illustrate our findings by example, we use a Rice-Mele model [116] with a focusing nonlinearity ($g > 0$). The Rice-Mele model has two sites per unit cell and is the Thouless pump model with the smallest number of sites per unit cell. The linear

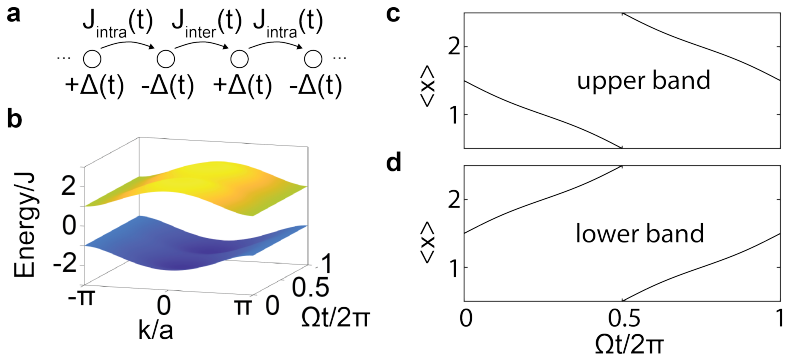

Figure 4.2. Rice-Mele model. **a**, Schematic illustration of the Rice-Mele model showing the inter-unit cell hopping ($J_{\text{inter}}(t)$), intra-unit cell hopping ($J_{\text{intra}}(t)$) and a staggered on-site potential $\Delta(t)$. **b**, Band structure of the Rice-Mele model showing two bands with Chern number $C = +1$ for the lower and $C = -1$ for the upper band. **c**,**d** Center of mass position of the instantaneous Wannier functions for the upper (**c**) and lower band (**d**) as a function of the pumping parameter Ωt.

Hamiltonian of the Rice-Mel model is schematically illustrated in Fig. 4.2a and given by

$$\begin{aligned} H_{nm}^{\text{RM}}(t) = &-[J + (-1)^{m+1}\delta\cos(\Omega t)]\delta_{n-1,m} \\ &-[J + (-1)^{m}\delta\cos(\Omega t)]\delta_{n+1,m} \\ &-\Delta(-1)^{m}\sin(\Omega t)\delta_{n,m} \end{aligned} \tag{4.13}$$

Here, Ω is the modulation frequency. The parameter J describes the average hopping strength between nearest-neighbor sites, which is modulated with strength δ, introducing a difference between intra- and inter-unit cell hoppings. The parameter Δ gives the strength of modulation of the staggered on-site potential. For specific numerical examples throughout this chapter, we use $\delta/J = 0.5$, $\Delta/J = 1$, and 200 sites with periodic boundary conditions. The band structure of this model shows two bands (see Fig. 4.2) with Chern number $C = +1$ and -1 for the lower and upper band, respectively. A simple way to calculate the Chern number is to plot the position of the Wannier centers for one pump cycle $t \in [0, 2\pi/\Omega]$ and evaluate their winding around the unit cell, as shown in Fig. 4.2c and d.

We illustrate the intimate link between the position of the soliton and the Wannier function in the Rice-Mele model for $\Omega t = 2\pi/8$, where no spatial symmetries pin the soliton to a fixed position. We calculate the instantaneous solitons in two ways and then compare their shape in real and Wannier space: (1) The exact soliton (Fig. 4.3b-e; shown in red) is calculated via Eq. (4.2) in real space and then transformed via change of basis into Wannier space. (2) We use Eq. (4.12) and calculate the soliton (Fig. 4.3b-e; shown

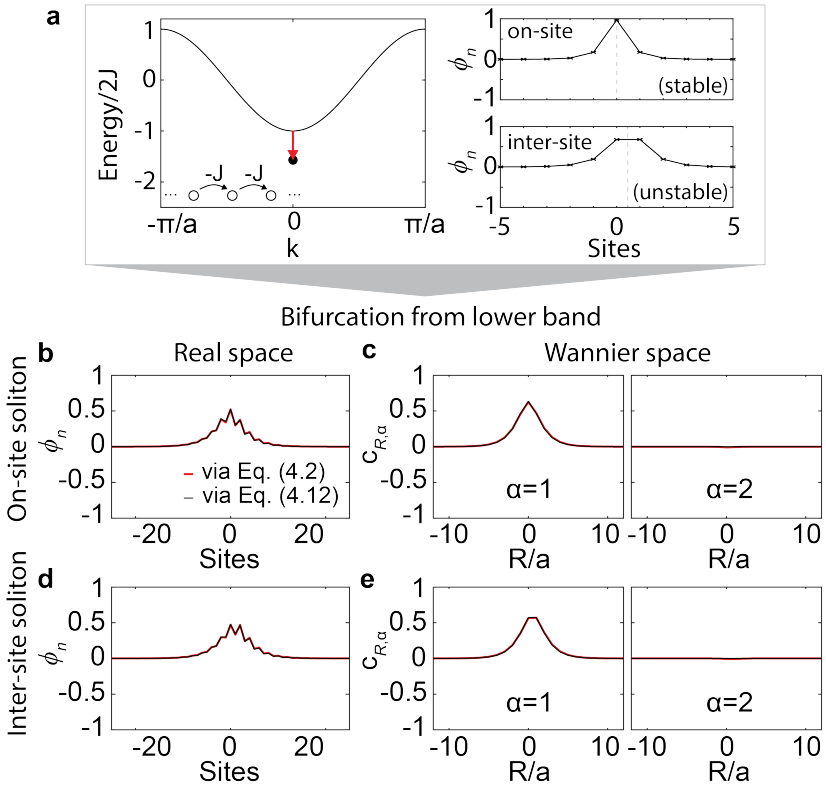

Figure 4.3. Comparison between soliton calculation in real space via Eq. (4.2) and Wannier space via Eq. (4.12) for the lower band of a Rice-Mele model. a, Left: band structure for a simple 1D lattice with hopping $J > 0$. Bifurcation of solitons (for focusing nonlinearity) occurs from the bottom of the band. Right: The two types of possible solitons: on-site and inter-site solitons. **b**, **c**, Expansion coefficients, ϕ_n and $c_{\boldsymbol{R},\alpha}$, of the instantaneous on-site soliton in real space (**b**) and Wannier space (**c**) for $\Omega t = 2\pi/8$ and the lower band in a Rice-Mele model with g/J=1. The soliton calculated in real space via Eq. (4.2) is shown in red. The soliton calculated in Wannier space via Eq. (4.12) is shown in black. α is the band index and a is the length of the unit-cell. **d**, **e**, Similar to **b** and **c** but for the inter-site soliton.

in black) in Wannier space, which is then transformed into real space. For low degree of nonlinearity, excellent agreement is observed, both for the on-site and the inter-site solitons (see Fig. 4.3b–e).

Similar behavior is found for solitons that bifurcate from the upper band, as shown in Fig. 4.4. For a focusing nonlinearity solitons bifurcate from the bottom of the band, which for the upper band is located at $k = \pm\pi/a$. As a consequence those solitons inherit a staggered phase. This is most clearly visible in Wannier space, where the phase structure is decisively staggered. In real space, the staggered phase is visible but follows a more intricate pattern, as can be understood from transforming the staggered phase in Wannier space back into real space. In the Wannier picture, the upper band is described

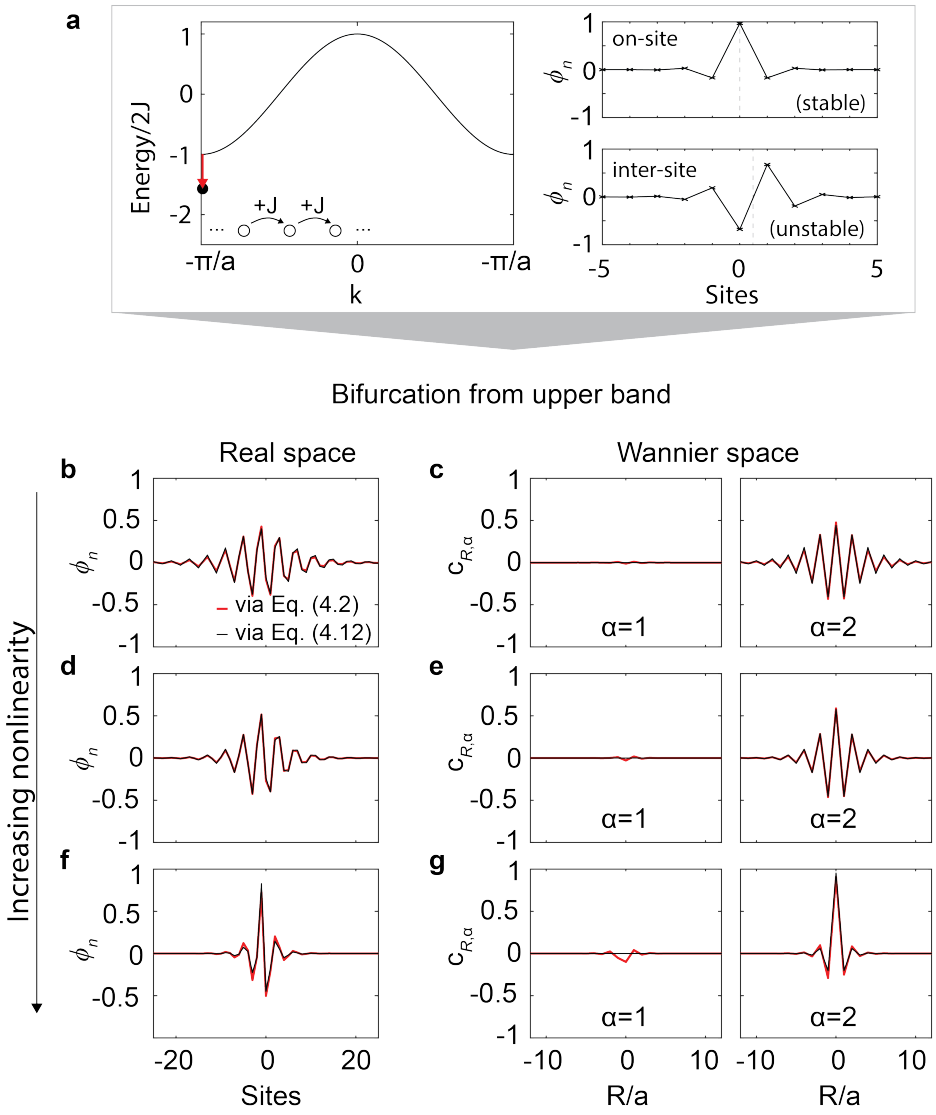

Figure 4.4. Comparison between soliton calculation in real space via Eq. (4.2) and Wannier space via Eq. (4.12) for the upper band of a Rice-Mele model. Similar to Fig. 4.3, but with the following differences: **a**, Left: For the upper band (and a focusing nonlinearity) the soliton bifurcates from the bottom of the band at $k = \pm\pi/a$. Right: Note the phase structure due to the bifurcation from $k = \pm\pi/a$ for the on-site and the inter-site solitons. **b-g**, Expansion coefficients, ϕ_n and $c_{\boldsymbol{R},\alpha}$, of the instantaneous on-site soliton in real space (**b**,**d**,**f**) and Wannier space (**c**,**e**,**g**) for $\Omega t = 2\pi/8$ and the upper band in a Rice-Mele model calculated for increasing nonlinearity. (b),(c) are calculated with g/J=1; **d**, **e**, are calculated with g/J=1.4; **f**,**g**, are calculated with g/J=2.5. Not the increasing occupation of the lower band for increasing nonlinearity in the exact calculation (Eq. (4.2)) that is not captured in the simplified Wannier picture (Eq. (4.12)).

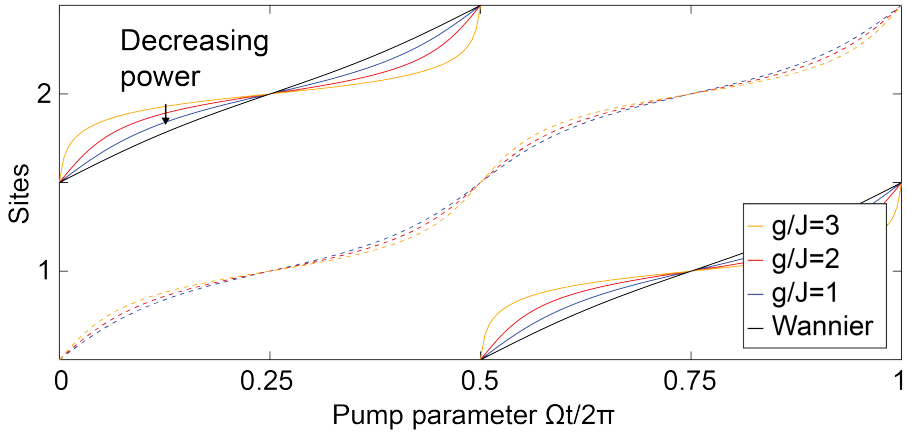

Figure 4.5. Soliton and Wannier flow. Position of the center of mass (c.m.) of the instantaneous solitons that bifurcate from the lower band with Chern number C=+1 for one pump cycle and projected into one unit cell. Stable on-site (unstable inter-site) soliton is shown with solid (dashed) lines. Different degrees of nonlinearity are shown in color. Black line shows the c.m. position of the Wannier function.

by Wannier sites and a positive nearest-neighbor hopping between them - in contrast to a negative nearest-neighbor hopping between the Wannier sites of the lower band. This allows the conclusion, that our discussion is equally valid for a defocusing nonlinearity, since after replacing $J \to -J$ and multiplying Eq. 4.2 (with $g < 0$) with minus one, the resulting equation is analogue to finding solitons with with eigenvalue $-\lambda$ in the focusing case. With increasing nonlinearity (Fig. 4.4 b-g), the projection of the exact soliton calculated via Eq. (4.2) shows more and more occupation of Wannier states of the lower band, suggesting that the approximations made in Eq. (4.12) become less accurate.

In order to show the pumping process, we calculate the position (modulo a unit cell) of the lower-band soliton for one complete pump cycle. Figure 4.5 shows the position of the stable on-site soliton (solid lines) and the position of the unstable inter-site soliton (dashed lines) for different degrees of nonlinearity (g/J) calculated via Eq. (4.2). While the unstable inter-site solitons (dashed lines) are mathematical solutions, propagation simulations via Eq. (4.1) show that the soliton breaks apart almost immediately due to its instability. In contrast, the on-site soliton is stable and follows the position of the Wannier function (black). We point out that, even at low power, due to interference terms between the occupied Wannier functions, the c.m. of the soliton does not have to be centered exactly upon the c.m. of the Wannier function, but is localized close to it. For stronger nonlinearity, the approximations of Eq. (4.12) become less accurate and larger deviations occur, due to the increasing occupation of Wannier functions of the upper band. Nevertheless, for increasing power, soliton motion remains quantized to the

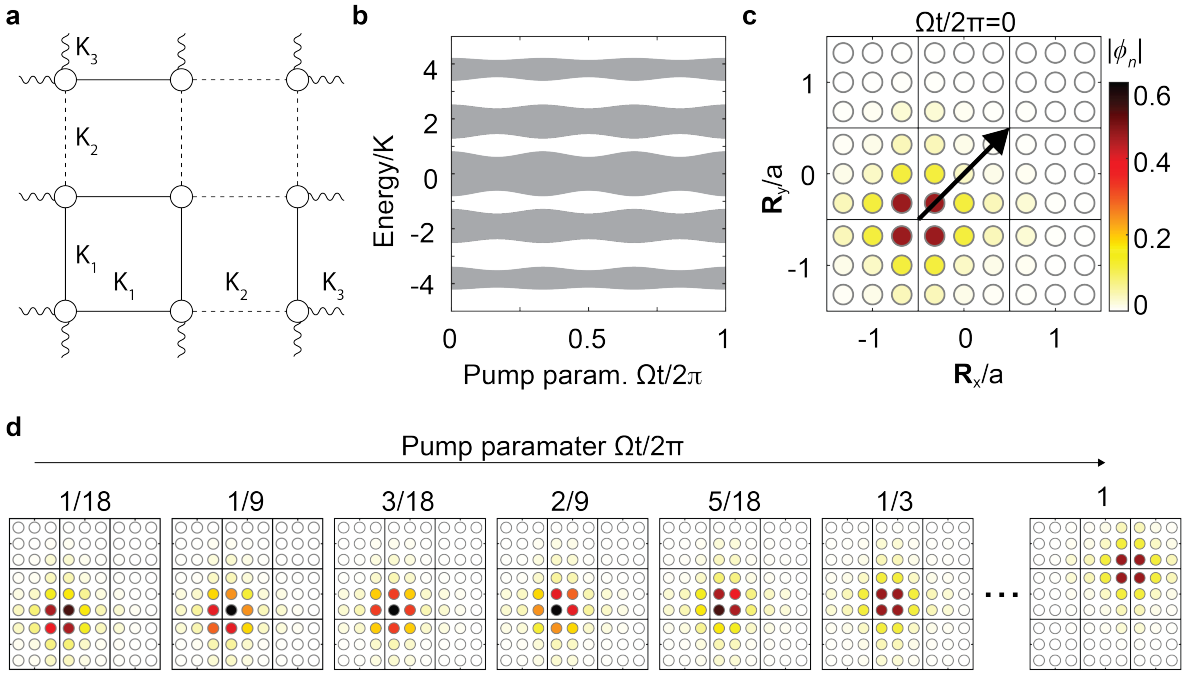

Figure 4.6. Two-dimensional quantized nonlinear pumping. **a**, Schematic of the unit cell with nine sites and three different hoppings, which are modulated in time. **b**, Band structure for the system shown in **a**. **c**, Instantaneous soliton localized at the corner of the unit cell for $\Omega t/2\pi$=0. **d**, Same as **c**, but showing the movement of the soliton for evolving pump parameter. The parameters for the AAH-model are chosen as $\tilde{K}/K$=0.7. In **c**,**d** the degree of nonlinearity is g/K=5.

Chern number: the solitons at the beginning and end of each pump cycle continue to be identical (apart from a translation by an integer number of unit cells). However, at some finite power a nonlinear bifurcation may act to split the trajectory or make the soliton unstable. This would change, or destroy, quantization.

4.3.2 Example: 2+2D pumping

Finally, we show that quantized nonlinear pumping can be extended to higher dimensions, by using a two-dimensional model consisting of the sum of two Thouless pumps in orthogonal spatial directions. Here, we use the off-diagonal version of the Aubry-André-Harper (AAH) model [62–64]. A schematic of the model is depicted in Fig. 4.6a, where only the hoppings are modulated: $K_j = -K - \tilde{K}\cos(4\pi j/3 + \Omega t)$ with $j \in \{1, 2, 3\}$. This model has been used to simulate the 4D quantum Hall effect and its topological properties are described by the second Chern number, which is the product of first Chern numbers for the two orthogonal directions [49]. The band structure for the pump cycle

is shown in Fig. 4.6b. We focus on a soliton that bifurcates from the lowest band. We point out that, while the linear model is separable in the x and y directions, the nonlinear model is not. Figure 4.6c shows the soliton at the beginning of the pump cycle $\Omega t/2\pi = 0$, pinned to the corner of the unit cell, due to symmetries. During the pump cycle (see Fig. 4.6d), the soliton is pumped by +1 unit cell in the x direction and +1 unit cell in the y direction, corresponding to the Chern numbers of the pumps in those directions, respectively.

4.4 Conclusion

In summary, we have shown that solitons in weakly interacting bosonic systems are pumped by the Chern number of the band from which they bifurcate, despite nonuniform band occupation. This proves that quantized nonlinear Thouless pumping is protected by the Chern number, which can thus be considered to be a physically meaningful topological invariant for describing nonlinear systems. We expect the soliton motion to remain quantized for increasing power until a nonlinear bifurcation splits the path of the soliton or makes it unstable. Furthermore, we described the Thouless pumping of unstable inter-site solitons and showed that quantized nonlinear pumping can also be observed in two-dimensional systems. Our results pave the way to a broader understanding of the interface between interacting systems (in particular described by nonlinearities in the mean-field limit) and topology.

Before the submission of the work presented in this chapter, we became aware of a related work by Nader Mostaan and co-workers [117].

Chapter 5
Fractionally quantized soliton Thouless pumping

This chapter describes the theoretical and experimental discovery of fractionally quantized pumping of solitons in nonlinear Thouless pumps at intermediate power. In contrast to previous chapters, the soliton exhibits integer quantized pumping only after multiple periods, but is displaced by a fraction after each period, as the soliton follows the maximally-localized multi-band Wannier state with fractional winding. At high power spontaneous symmetry breaking bifurcations lead to trapping. Our results are amongst the first observations of topologically protected fractional quantization in bosonic systems.

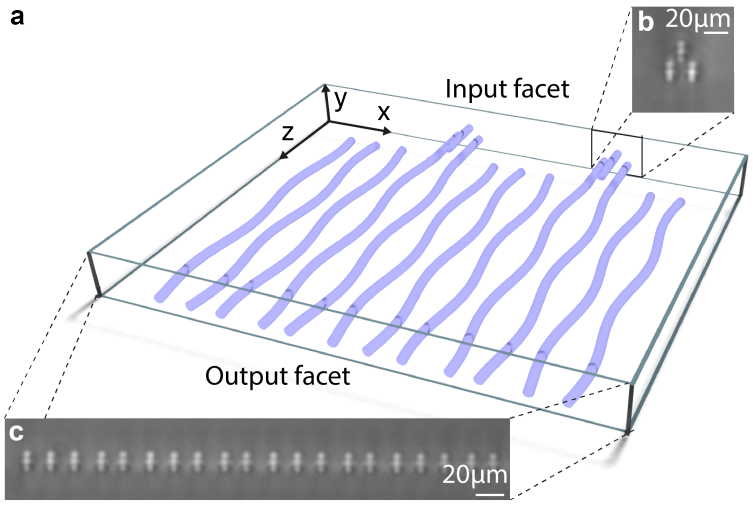

Figure 5.1. Photonic implementation of a five site AAH model. **a**, Schematic of the implementation of the model in arrays of evanescently coupled waveguides. Only two waveguides per unit cell extend to the input facet, with an additional waveguide fabricated on top to transform a single-site excitation into an effective two-site excitation. **b**,**c**, White-light micrographs showing the input (**b**) and output (**c**) facets.

This chapter is based on work that was done in collaboration with Sebabrata Mukherjee, Christina Jörg and Mikael C. Rechtsman and has been published in Ref. [2].

5.1 Introduction

In the previous two chapters we studied Thouless pumps [29], dimensional reduced versions of the integer quantum Hall effect. In the integer quantum Hall effect, a gas of non-interacting electrons can be rigorously shown to exhibit integer-quantized Hall conductance [3, 6, 118], fixed to a topological invariant – the Chern number. It was therefore a surprise when plateaux of fractional conductance appeared in the experiment of Tsui, Stormer and Gossard [32]. There, the strong interaction between electrons played the key role, giving rise to the formation of fractionally charged quasiparticles [119–121]. While the physics of the integer quantum Hall effect has been predicted and observed in a variety of experimental platforms including photonics [20] the physics of the fractional quantum Hall effect is experimentally mostly unexplored apart from its original electronic system. First experiments in bosonic platforms created bosonic two-particle fractional quantum Hall states using repulsive interactions between polaritons mediated by Rydberg atoms in a twisted cavity [122] and using ultracold atoms in an Harper-Hofstadter optical lattice model [123].

A conceptually different approach to incorporate interactions has been taken by treating the interactions of many photons in the mean-field limit using nonlinearity. This approach has led to the prediction and observation of various new topological phenomena in one-dimensional topological systems [124,125], two-dimensional topological insulators [35–38], as well as in 1+1 dimensional Thouless pumps [99]. The latter system is specifically suitable for studies in photonics due to the design flexibility available in fabricated structures. In particular, the results of Ref. [99] are described in Chapter 3 and show integer quantized nonlinear Thouless pumping via soliton motion, despite a decisively nonuniform band projection. Quantization stems from the fact that the soliton comes back to itself – modulo a translation by an integer number of unit cells due to translation invariance – after each period. In the previous Chapter 4, we analytically proofed that the position of low-power solitons is dictated by the position of the Wannier state of the band from which the soliton bifurcates. Hence, soliton pumping is not just quantized, but quantized by the Chern number of the respective band [109, 117].

In this chapter we theoretically predict and experimentally demonstrate quantized fractional pumping via soliton motion at higher power, when the strength of the nonlinearity

exceeds the relevant bandgap. We experimentally observe fractional soliton pumping by a fraction of $f = -1/2$ in arrays of evanescently coupled waveguides with Kerr nonlinearity. Fractional pumping occurs as the soliton follows the maximally-localized multi-band Wannier functions and returns to itself – modulo a translation by an integer number of unit cells – only after multiple periods. There is no known analogue in linear systems. Finally, we numerically show how tuning the strength of the nonlinearity leads to multiple plateaux of integer and fractionally quantized displacement within one Thouless pump model.

5.2 The 5-site AAH model

Experimentally, we realize a nonlinear Thouless pump by focusing high-peak-power laser pulses into arrays of single-mode evanescently coupled waveguides. Due to the Kerr effect, the refractive index becomes intensity-dependent, and the propagation of photons in the system is described by the discrete nonlinear Schrödinger equation [88, 90–94, 110]

$$i\frac{\partial}{\partial z}\phi_n(z) = \sum_m H_{n,m}\phi_m(z) - g|\phi_n(z)|^2\phi_n(z) \tag{5.1}$$

where m, n denote lattice sites, $\phi_n(z)$ is the amplitude of the wavefunction at propagation distance z for site n, $H_{nm}(z)$ is a z-dependent tight-binding Hamiltonian describing a topological Thouless pump, and $g > 0$ describes the strength of the focusing Kerr nonlinearity. In waveguide systems, z plays the role of a temporal coordinate. Equation (5.1) is also known as the Gross-Pitaevskii equation, which describes interacting bosons in a Bose–Einstein condensate in the mean-field limit [89, 111]. Therefore, our results are not restricted to photonics, but hold for a range of interacting and nonlinear bosonic systems [22, 112–114, 126]. In waveguides, the nonlinearity describes an effective interaction between photons mediated by the ambient material. To treat experiment and theory on the same footing, we define $P = \sum_n |\phi_n(z = 0)|^2$, and refer to the strength of nonlinearity as a dimensionless quantity, $gP/J^{\max}$, where $J^{\max}$ is the largest hopping value in the Hamiltonian. We illustrate fractional Thouless pumping in an off-diagonal Aubry-André-Harper (AAH) model [44, 62–64] with five sites per unit cell and zero on-site detuning (Fig. 5.2a). Its nearest-neighbour couplings $J_n(z)$ are periodically modulated in z, and the Hamiltonian is given by $H_{nm}(z) = -J_n(z)\delta_{m,n+1} - J_{n-1}(z)\delta_{m,n-1}$. Figure 5.2b shows the strength of the hoppings over one period, as used in the experiment. The band structure of this model is depicted in Fig. 5.2c and has five bands with Chern numbers

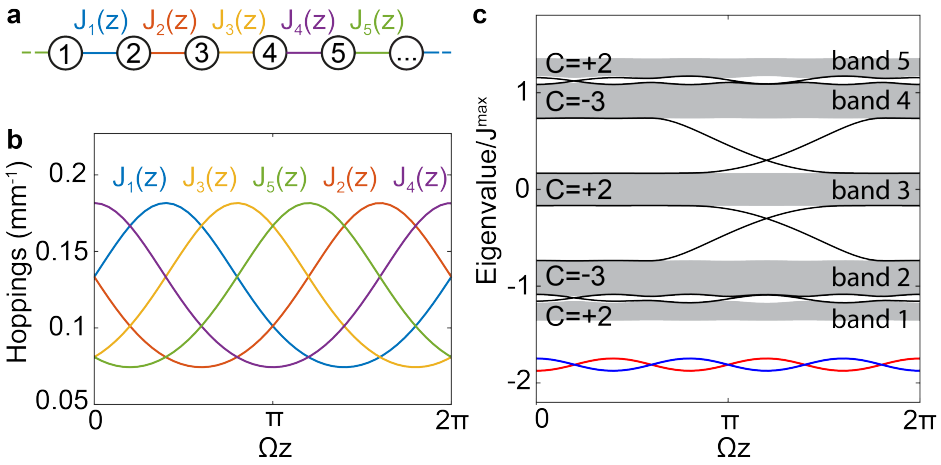

Figure 5.2. Model for quantized fractional Thouless pumping. a, Illustration of the off-diagonal AAH model, with five sites per unit cell and z-dependent hoppings $J_n(z)$ between nearest-neighbour sites. **b**, Modulation of the hopping strength over one period. **c**, Band structure (instantaneous energy eigenvalues) of the Hamiltonian, showing five bands (grey) with Chern numbers $C = \{2, -3, 2, -3, 2\}$, end states (black lines) crossing the bandgaps, and nonlinear eigenvalues (red and blue lines) of instantaneous solitons that are pumped by a fraction $f = -1/2$.

$C = \{2, -3, 2, -3, 2\}$. A schematic illustration of the implementation in an array of evanescently coupled waveguides is shown in Fig. 5.1, where the periodic modulation of the distance between neighbouring waveguides changes the evanescent hopping strength. In the experiment the position of waveguide n is $x_n(z) = n{\cdot}d{+}\delta\cos(\Omega z + 4\pi n/5 - 6\pi/20)$, where d defines the average separation between waveguides, δ is the spatial modulation strength, and Ω is the modulation frequency. Throughout this chapter, we use d=17.25 μm and δ=1 μm. Figure 5.1a also schematically shows an input region, where only two waveguides per unit cell are extended all the way to the input facet with an additional waveguide on top. We use this 'triple coupler' to transform a single-site excitation of the upper waveguide into an effective two-site excitation of the two lower waveguides. White-light images of the input and output facets are shown in Fig. 5.1b,c, respectively.

5.3 Propagation simulations

Quantized pumping in linear Thouless pumps (g=0) requires uniform band occupation and adiabatic driving. Under these conditions, the displacement per period is dictated by the Chern number of the occupied band. The scenario is very different in the nonlinear domain, which we explain as follows. Nonlinear systems allow for spatially localized

eigenstates, so-called solitons [92,127–130] and we are only concerned with bright discrete spatial solitons, for which the focusing nonlinearity balances the spatial diffraction. For decreasing power, solitons can be traced back to the (linear) band from which they bifurcate (see Appendix B). In the previous chapter, it has been shown that low-power solitons in Thouless pumps move (that is, are pumped) according to the Chern number of the band from which they bifurcate, despite non-uniform band occupation, because they follow the position of the instantaneous single-band Wannier functions [109]. An equivalent result has also been reported in Ref. [117]. Integer quantization occurs because, after each period, the soliton returns to its initial state, apart from a translation by an integer number of unit cells [99]. Throughout this chapter, Wannier functions are defined for the linear (non-interacting) model. In the adiabatic limit, the propagation of a stable soliton can be examined by calculating the instantaneous soliton for each z-slice. We confirm the existence of an adiabatic limit for soliton pumping numerically, which agrees with the results of Refs. [104, 105].

We focus on the propagation of a soliton that, at z=0 and $P \to 0$, bifurcates from the lowest band. Figure 5.3a (left) shows one example of a low-power soliton ($gP/J^{\max}$=0.55) for two pumping periods. After each period, the soliton's wavefunction returns to its initial wavefunction (as shown by the insets), only translated by two unit cells, as dictated by the Chern number of the band from which the soliton bifurcates (the band has Chern number +2). The propagation of a soliton for higher power ($gP/J^{\max}$=1.65), which shows fractional pumping, is displayed in the centre of Fig. 5.3a. In this case, the soliton after one period is clearly different from the soliton at z=0. The wavefunction is not peaked on two sites, but instead on a single site, and its center of mass displacement is -1/2 unit cells. Only after two periods is the soliton's wavefunction identical to the initial one modulo a translation by one unit cell in the negative direction (leftward). This behaviour goes hand in hand with the presence of two soliton solutions that are degenerate at certain points in the pump cycle (these are the nonlinear eigenvalues plotted in Fig. 5.2c in red and blue), as we explain in the following. For even higher power, the soliton is trapped (Fig. 5.3a, right side). Although we show only one example of each regime in Fig. 5.3a, quantization of soliton transport occurs over a wide range of nonlinearity and has a rich plateau structure, as shown below.

To explain this behaviour, and especially the origin of fractional pumping, we plot in Fig. 5.3b–d the center of mass positions of the instantaneous solitons from Fig. 5.3a together with the position of the relevant maximally-localized instantaneous Wannier functions, projected into a single unit cell. For single bands, the latter are identical to

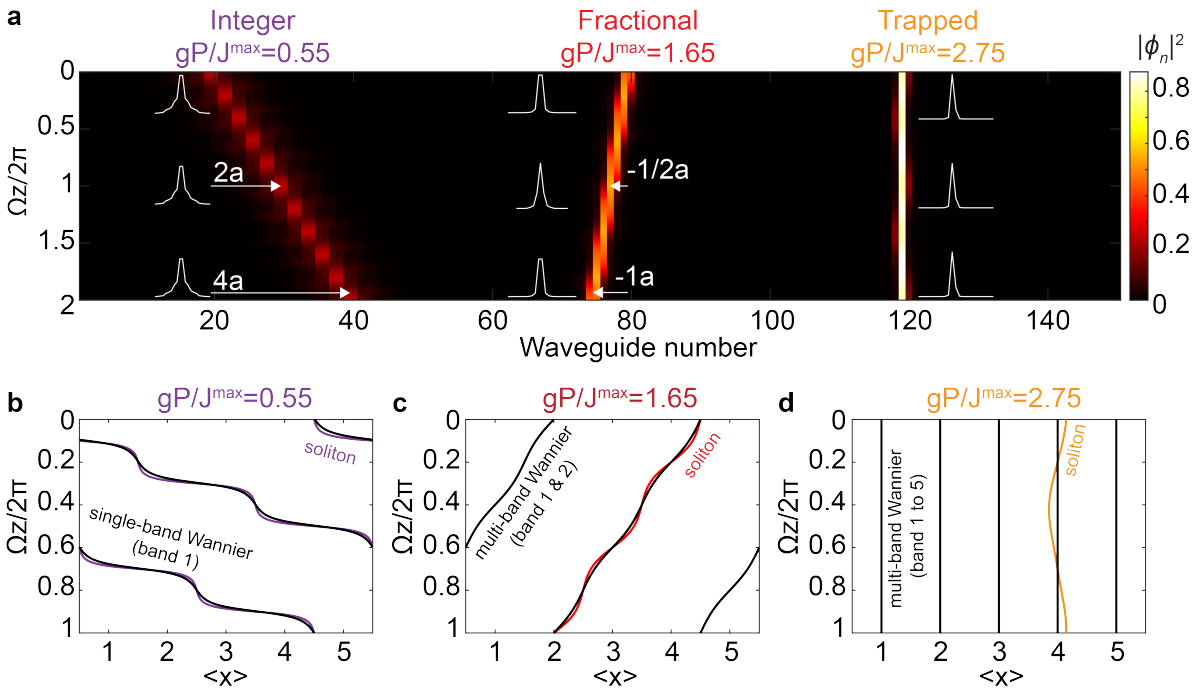

Figure 5.3. Theory of quantized fractional Thouless pumping. **a**, Individually normalized wavefunctions of instantaneous solitons ($gP/J^{\max}$=0.55, 1.65 and 2.75, from left to right), calculated for two periods. The insets show the shape of the solitons at z=0 and after each full period. Arrows denote the displacement of the soliton after one and two periods in units of the lattice vector a. Notice that the shape of the fractionally pumped soliton (in the centre) changes after each period, and its displacement is only 1/2 of a unit cell per period. **b**–**d**, Comparison between the center of mass trajectory of the relevant instantaneous Wannier functions (black) of the linear model and the instantaneous solitons (purple, red) projected into one unit cell (with sites 1 to 5). The low-power soliton ($gP/J^{\max}$=0.55; shown in **b** in purple) follows the single-band Wannier function of the lowest band. The trajectory of the fractionally pumped soliton ($gP/J^{\max}$=1.65; shown in **c** in red) follows the maximally-localized multi-band Wannier function calculated for the two lowest bands combined. The position of the trapped soliton ($gP/J^{\max}$=2.75; shown in **d** in orange) follows the multi-band Wannier functions calculated for all five bands combined.

the gauge-invariant eigenvalues of Wilson loops. As proved in Refs. [109, 117], the stable low-power soliton follows (with small deviations) the position of the Wannier functions of the band from which it bifurcates. Hence, the gauge-invariant positions of the single-band Wannier function for each z-slice dictates the path of the low-power ($gP/J^{\max}$=0.55) soliton as depicted in Fig. 5.3b. As the two lowest bands of the AAH model are only separated by a small bandgap, the underlying assumption that the soliton's dynamics are determined by a single band is no longer justified for increasing power. Instead, an effective description has to take into account the lowest two bands, for which their multi-band Wannier functions have to be calculated, which means that there are two

Wannier functions per unit cell. Importantly, multi-band Wannier functions are typically quite different in shape compared with each of the single-band Wannier functions (see, for example, Ref. [65] for details). Although the center of mass positions of multi-band Wannier functions are not gauge-invariant, the positions of the maximally-localized Wannier functions are unique, as in the single band case. In Fig. 5.3c we show that, for $gP/J^{\max}$=1.65, the soliton follows the position of the instantaneous maximally-localized multi-band Wannier functions. As those are displaced by only 1/2 of a unit cell per cycle (and transform into each other), the soliton pumps fractionally. With further increasing power, the soliton becomes trapped and follows the instantaneous maximally-localized multi-band Wannier functions of all bands, which are delta functions for each site in a tight-binding model, shown in Fig. 5.3d. Thus, the trapped regime can be thought of as the trivial limit of multi-band pumping. Although the winding of the trajectories in Fig. 5.3b,c looks deceptively similar, there are distinct differences between integer and fractional pumping. First, while at each z-slice there is only one position value in Fig. 5.3b, there are two in Fig. 5.3c, as the number of Wannier functions per unit cell equals the number of participating bands. Second, the winding of the Wannier function in Fig. 5.3b over one period is equal to the Chern number of the band (C_1=+2) and dictates the pumping. In Fig. 5.3c, the combined winding of both Wannier functions gives the combined Chern number of both bands, $C_{1-2} = +2 - 3 = -1$.

In a conventional fermionic Thouless pump with a Fermi level in the bandgap above the second band, both multi-band Wannier states are simultaneously occupied and therefore only integer-quantized pumping occurs. Remarkably, for the soliton it is possible to track a single maximally-localized multi-band Wannier function along its trajectory (as shown in Fig. 5.3c), and the soliton is therefore pumped by a fraction after one period and by an integer after two periods. Fractional pumping is therefore an intrinsically nonlinear effect, because the projection of the multi-band Wannier function onto the linear energy eigenstates (that is, the occupation of the Bloch states) changes with z. In contrast, any linear pumping process with non-degenerate bands has—in the adiabatic limit—a constant occupation by definition. Observing that the soliton follows the maximally-localized multi-band Wannier function, whose combined displacement is given by the sum of the Chern numbers C_i of the respective bands denoted by i, we label the fractionally pumped soliton by the fraction f that describes the average displacement per period:

$$f = \frac{\sum_{i=1}^{N_b} C_i}{N_b} \tag{5.2}$$

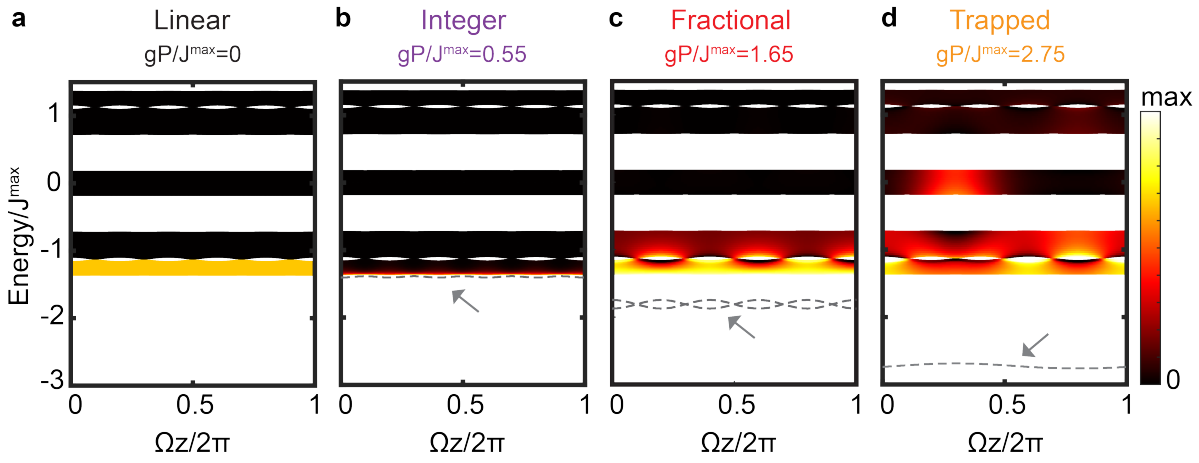

Figure 5.4. Band occupations in different regimes of quantized Thouless pumping. **a**, In the linear regime a uniform band occupation during the complete pumping cycle is necessary for quantization. **b-d**, Band occupation of the propagated solitons in the integer quantized (fractionally quantized, trapped) regime are shown in **b** (**c**,**d**), respectively. Band occupations are calculated as projections of the propagated wavefunction onto the instantaneous Bloch functions of the linear model. Dashed lines indicate the nonlinear eigenvalues of the solitons. Each subfigure is individually normalized.

where N_b denotes the number of participating bands. In this way, the numerator defines the number of unit cells by which the soliton is pumped in the x-direction before returning to the same wavefunction, and the denominator defines the number of pump cycles (in z) over which this process occurs. For the cases shown in Fig. 5.3b–d, $f = 2/1 = 2$, $f = (2-3)/2 = -1/2$ and $f = (2-3+2-3+2)/5 = 0$, respectively. From Eq. (5.2) it is clear that bandgap closings (including topological transitions) within the group of participating bands will not change f and therefore do not change the soliton's fractionally quantized displacement.

To further distinguish the different regimes of Thouless pumping, we analyze their band projections. We compare all four regimes, namely linear Thouless pumping, integer and fractionally quantized nonlinear Thouless pumping, and the trapped regime. Figure 5.4 shows the projection of the propagated wavefunction onto the band structure (i.e. the projection onto the instantaneous energy eigenstates.) In the linear case quantization occurs only for uniform band occupations. This can be achieved by exciting the system using a state with a uniform band projection (e.g. a Wannier state) and subsequently modulating the Thouless pump slowly enough, such that the adiabatic theorem applies and the band occupations stay constant, as shown in Fig. 5.4a. Distinctly different pictures emerge in the case of nonlinear pumping. For integer quantized pumping, the projection of the propagated soliton wavefunction onto the the bands shows maximal occupation

for the lowest state of the lowest band and decreasing occupations of energetically higher lying states (see Fig. 5.4b). This distribution becomes increasingly sharp for decreasing power when the soliton can be approximated by the lowest Bloch state multiplied with a wide hyperbolic secant envelope function. In the regime of fractional soliton pumping, we find significant occupations of the two lowest bands (see Fig. 5.4c). This is in agreement with our assessment that the fractionally pumped soliton follows the multi-band Wannier states of the lowest two bands. Furthermore, the band occupations are decisively non-uniform and varying during the pumping cycle, underlining that fractional soliton pumping has no linear analogue. As the soliton only comes back to itself after two periods, fractional pumping implies a ground state degeneracy, as indicated by the two dashed lines in Fig. 5.4c that represent the nonlinear eigenvalues of the two possible solitons at each z-slice. It is only after two periods, that the eigenvalue curves come back to themselves. Finally, the band projection of the trapped soliton shows occupation also of higher bands.

5.4 Experimental observation

We experimentally observed quantized fractional Thouless pumping in evanescently coupled waveguide arrays with Kerr nonlinearity. The waveguides were fabricated by means of femtosecond direct laser writing in borosilicate glass [76, 78]. Straight waveguides showed propagation losses of (0.33 ± 0.02) dB cm^{-1}, and we measured no additional nonlinear losses. To excite the system, we focused high-power laser pulses into the waveguides; these were temporally stretched to 2 ps and down-chirped [36]. This configuration minimizes the generation of new wavelengths via self-phase modulation while reaching the necessary degree of nonlinearity. Maintaining a narrow spectrum is essential, as the hopping constant is a function of wavelength. In our experiment, the spectrum at the position of the pumped soliton broadened to 14 nm for maximum input power and propagation distance [2]. Because the coupling constants between waveguides vary minimally over this range of wavelengths [36, 99], Eq. (5.1) describes our system well, provided we include unavoidable propagation losses. We measured a fractional pumping of $f = -1/2$, meaning that the soliton is pumped to the left by one unit cell after two periods. For our experiment, it is crucial to efficiently excite the soliton, whose wavefunction is mainly peaked on two sites for z=0, as shown in Fig. 5.3a. To facilitate this, our sample contained a 5-mm-long input region, in which only two waveguides per unit cell extend all the way to the input facet, together with one additional waveguide on

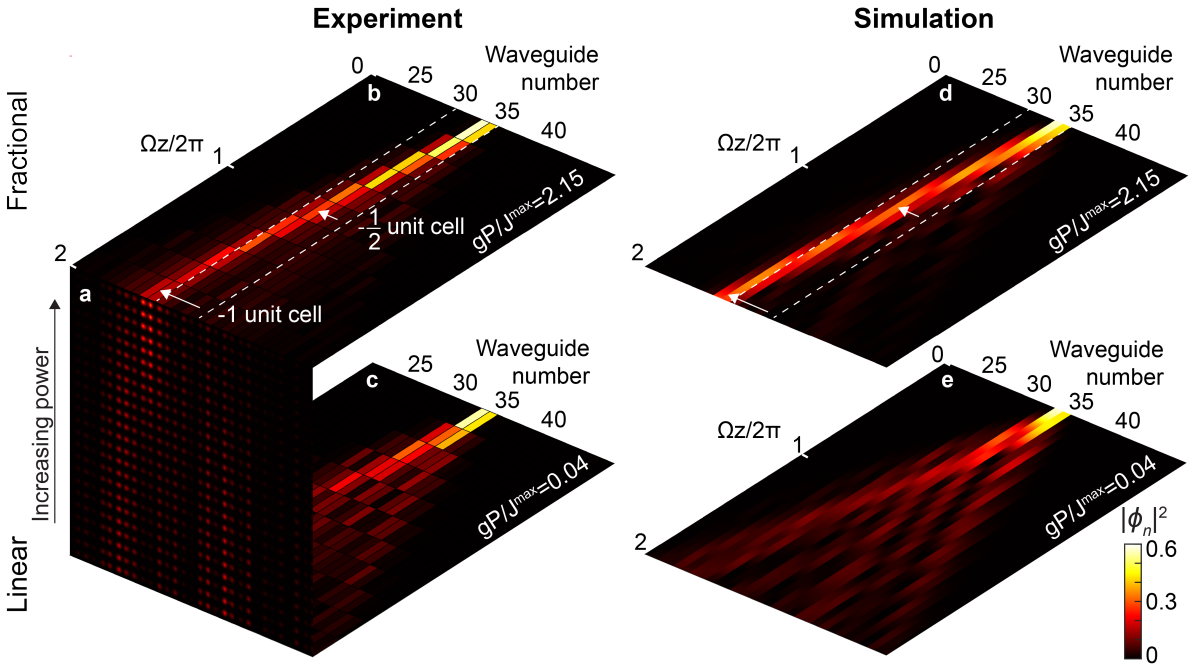

Figure 5.5. Experimental observation of an $f = -1/2$ fractionally pumped soliton. **a**, Stacked images of the output facet, showing the intensities in the waveguide modes after propagation for two periods. Each row was imaged separately at different input power. The bottom row shows the output facet for linear propagation ($gP/J^{\max}$=0.04). The next row was taken for $gP/J^{\max}$=0.09 and then for each row the power was increased in equal steps of $gP/J^{\max}\approx$0.09 until the top row, with a maximum input power of $gP/J^{\max}$=2.15. **b**,**c**, Normalized integrated intensities in each waveguide for different z-slices for an input power of $gP/J^{\max}$=0.04 (**c**) and $gP/J^{\max}$=2.15 (**b**). The white dashed lines mark one unit cell. After one period, the soliton is peaked on a single site, and its centre of mass has shifted by half a unit cell. After two periods, the soliton is peaked on two sites and displaced by -1 unit cell. **d**,**e**, Tight-binding propagation simulations corresponding to **b** and **a**, including propagation losses and using the measured initial two-site excitation. For direct comparison with the experiment, the plotted intensities are normalized for each z.

top (also Fig. 5.1a,b). This 'triple coupler' converts a single-site excitation of the upper waveguide into an effective two-site excitation of the lower waveguides.

We detected the fractional pumping behaviour of the soliton at high power by measuring the intensity distribution of the waveguide modes at the output facet as a function of the input power for a lattice with 12 unit cells. Figure 5.5a shows the normalized mode intensities at the output facet after two periods. Each row of modes corresponds to an individual measurement, and the input power increases from bottom to top. For the lowest input power ($gP/J^{\max}$=0.04; Fig. 5.5a, bottom row), the system behaves linearly, and the intensity diffracts widely in the waveguide array. For increasing

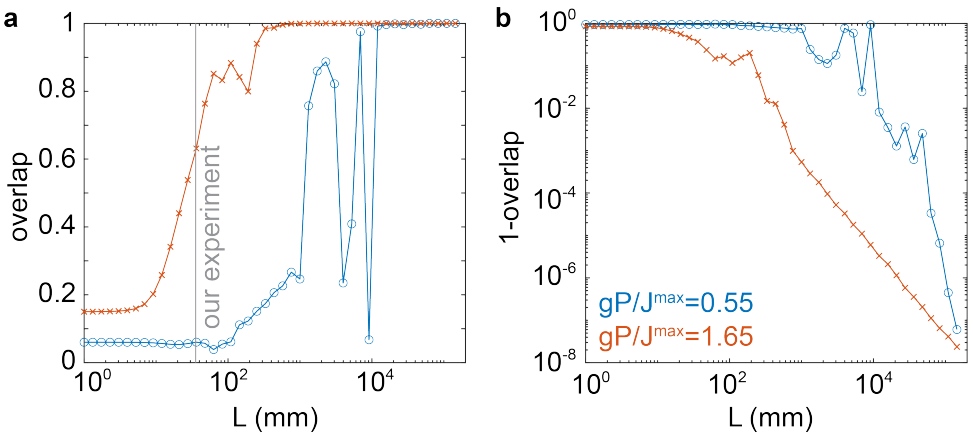

Figure 5.6. Adiabaticity of soliton propagation. **a**, Overlap of a numerically propagated soliton with the instantaneous soliton after one pump cycle with period L. **b**, Same data as **a**, but plotted as deviation from perfect overlap on a log-log scale confirming the existence of an adiabatic limit. The blue (orange) line depicts $gP/J^{\max} = 0.55$ ($gP/J^{\max} = 1.65$), which corresponds to the integer (fractionally) pumped soliton in the adiabatic limit.

input power, the nonlinearity counteracts the diffraction, and less spreading is visible. At the maximum input power of $gP/J^{\max}$=2.15 (Fig. 5.5a, top row), the intensity at the output facet is localized mainly to two waveguides, one unit cell away from the excited waveguides. This is the signature of the $f = -1/2$ fractionally pumped soliton after two periods. To further verify the fractional pumping behaviour, we mapped out the propagation of the soliton by repeatedly cutting the sample and imaging the output facet. The normalized integrated intensities per mode (which are equivalent to $|\phi_n|^2$) are shown over two periods in Fig. 5.5c for linear propagation ($gP/J^{\max}$=0.04) and in Fig. 5.5b nonlinear propagation ($gP/J^{\max}$=2.15). Corresponding numerical simulations using the experimentally measured mode intensities of the effective two-site excitation and including realistic losses are shown in Fig. 5.5e for the linear and Fig. 5.5d for the fractionally pumped case.

Imperfect adiabaticity leads to radiation from the soliton into linearly diffracting modes and our waveguide system does not behave perfectly adiabatically; it is sufficiently adiabatic to observe the fractionally pumped but not the integer-pumped soliton, which has weaker confinement. Fig. 5.6a shows the calculated overlap, $|\sum_n \phi_n^{*(\mathrm{S})}(L)\phi_n(L)|^2$, between the propagated wavefunction $\phi_n(L)$ and the instantaneous soliton $\phi_n^{(\mathrm{S})}(L)$ after one period. For perfect adiabaticity the overlap is one. The deviation from perfect overlap is shown in Fig. 5.6b on a log–log scale, which demonstrates the presence of an adiabatic limit. These results agree with the adiabatic time-evolution studies of nonlinear systems in Refs. [104, 105]. Fig. 5.6 clearly indicates that the lower-power

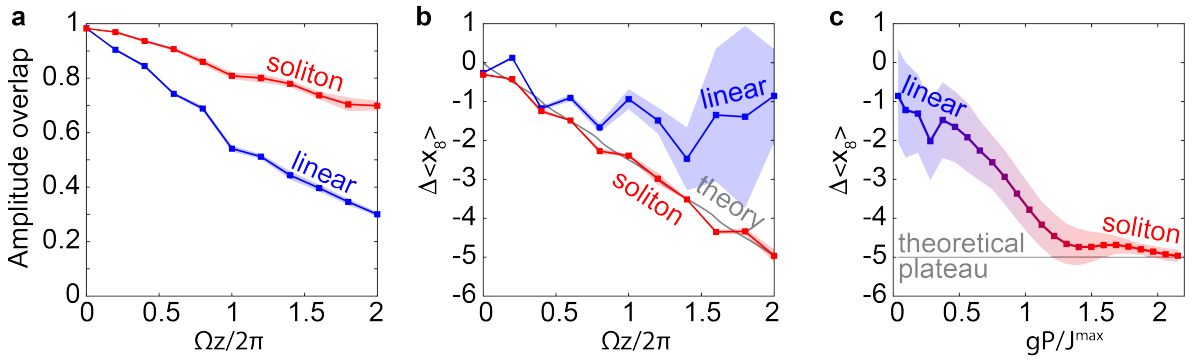

Figure 5.7. Verification of soliton's pumping behavior in the experiment. a, Amplitude overlap, $\sum_n |\phi_n^{(\mathrm{Exp.})}||\phi_n^{(\mathrm{S})}|$, between the measured output wavefunction, $\phi_n^{(\mathrm{Exp.})}$, and the numerically-calculated instantaneous soliton wavefunction, $\phi_n^{(\mathrm{S})}$, as a function of propagation length for linear propagation (gP/J^{max}=0.04; shown in blue) and soliton propagation (gP/J^{max}=2.15; shown in red). **b**, Center of mass displacement of the experimentally observed soliton and linear propagation (calculated using a higher order norm to suppress linear background effects; see text). Gray line indicates the numerically-calculated displacement of an instantaneous fractionally pumped soliton. **c**, Experimentally observed center of mass displacement after two periods for increasing input power showing a plateau at high input power. Gray line indicates the expected theoretical displacement of five sites (one unit cell) after two periods for the fractionally pumped soliton. Solid lines with squares show mean values, and shaded areas show one standard deviation for independently measured soliton propagation in eight different unit cells of the same lattice.

(integer-pumped) soliton needs slower driving frequencies compared to the higher-power (fractionally pumped) soliton to be similarly adiabatic and experimentally observable. Furthermore, Fig. 5.6a confirms that our experiment is sufficiently adiabatic to detect the signature of the fractionally pumped soliton. In the experiment, the contrast is further lowered by the tails of the laser pulses, which have lower intensity and thus behave more linearly. Nonetheless, our experiment (Fig. 5.5) clearly shows a soliton displaced to the left by one unit cell after two periods with the characteristic shape of being localized on two sites after two periods and localized on just one site after one period (see also the instantaneous soliton in the centre of Fig. 5.3a). We expect that the solitons that we observe here would also be formed under spatial modulation instability, starting from a broad input beam. The solitons that form spontaneously would then exhibit quantized motion in the course of the pump.

We quantify our observation of fractional Thouless pumping by calculating the amplitude overlap of the measured soliton with the instantaneous soliton of a perfectly adiabatic system. The results for eight measurements from different unit cells within the same lattice are shown in Fig. 5.7a. We found a decreasing overlap for linear propagation

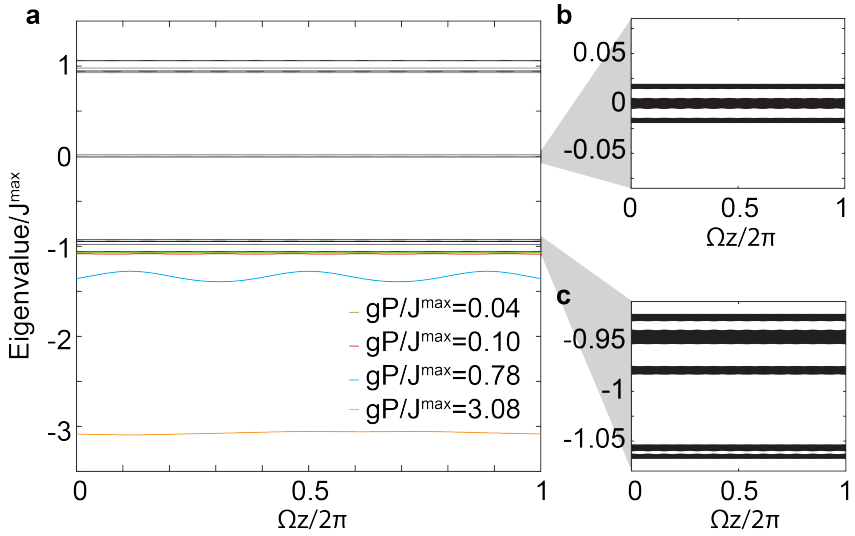

Figure 5.8. Band structure of a 13 site AAH model. a, Additionally to the 13 linear energy bands (black) the nonlinear eigenvalues of four pumped solitons with $gP/J^{\max} = 0.04$, 0.10, 0.78 and 3.08, which are part of the plateaux in Fig. 5.9 are shown in green, red, blue and yellow, respectively. **b**, Zoom-in onto the central group of three energy bands. **c**, Zoom-in onto the lowest group of five energy bands.

with a low overlap of about 30% after two periods, and an overlap of about 70% for the nonlinear propagation (see Fig. 5.7a). Deviations from perfect overlap mainly stem from losses and imperfect adiabaticity. We further quantify the soliton's center of mass displacement using a higher order norm:

$$\langle x_8 \rangle = \sum_n n|\phi_n|^8 / |\phi_n|^8 \tag{5.3}$$

This quantity reduces the influence of the experimentally unavoidable linearly propagating background in the calculation of the centre of mass. These results are shown in Fig. 5.7b: the experimentally observed wavefunction clearly follows the position of the numerically calculated instantaneous soliton. In contrast, the center of mass position of the linear propagation is non-quantized and individual measurements show strong deviations. Finally, we evaluate the center of mass displacement (using the higher order norm) as a function of input power, and observe clear features of a plateau of fractional displacement per period (see Fig. 5.7c).

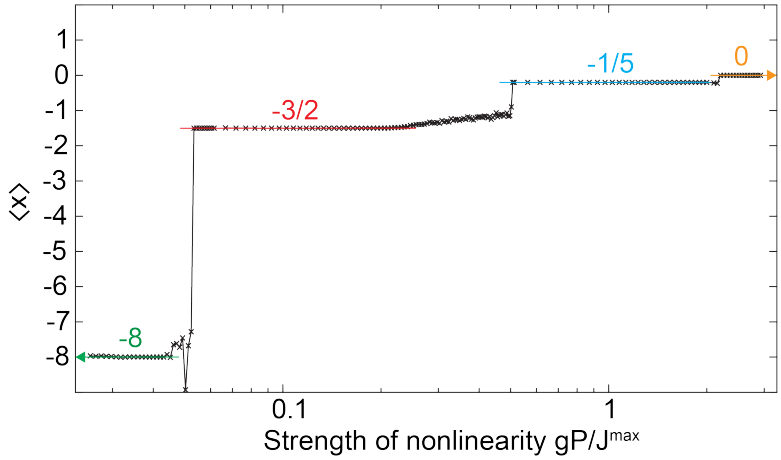

Figure 5.9. center of mass displacement. Average center of mass displacement per period, $\langle x \rangle$, calculated for an off-diagonal AAH model with 13 bands. For low power ($gP/J^{\max} < 0.04$), soliton motion is determined by the integer-quantized Chern number of the band from which the soliton bifurcates ($C = -8$). With increasing nonlinearity, plateaux of fractionally quantized displacement of -3/2 and -1/5 appear. For $gP/J^{\max} > 2.2$, the soliton is trapped and the average displacement is zero. Note that data points for $gP/J^{\max} < 0.06$ and $gP/J^{\max} > 0.06$ are calculated for different propagation lengths and periods to ensure adiabaticity (see also Supplementary Information in Ref. [2]).

5.5 Multiple fractional plateaux

Finally, we demonstrate numerically that multiple plateaux of integer and fractionally quantized pumping can occur within one Thouless pump model for increasing nonlinearity. We numerically solve Eq. (5.1) for an off-diagonal AAH model with 13 sites per unit cell using periodic boundary conditions and modulate the hoppings according to $J_n(z) = J + \delta\cos(\Omega z + 10\pi n/13 + 2\pi/13)$, and $\Delta/J = 0.95$. This model has 13 bands (see 5.8) that are distributed symmetrically around zero energy and which can be clustered into five bands at low energy (see 5.8c), three bands around zero energy (see 5.8b) and five high energy bands. The group of the lowest five bands has another subgroup of energetically close bands, consisting of the two lowest bands. The Chern numbers of the bands are: $C = \{$-8,5,5,- 8,5,5,-8,5,5,-8,5,5,-8$\}$ from bottom to top, respectively.

The initial excitation is chosen to be a power-dependent, instantaneous soliton that bifurcates from the lowest band. In Fig. 5.9 we plot the average center of mass displacement per period $\langle x \rangle$, showing four plateaux of quantized displacement. At low power the center of mass displacement is integer-quantized, as dictated by the Chern number of the band from which the soliton bifurcates: C=-8. With increasing nonlinearity, the two lowest bands participate in soliton pumping, resulting in a fractional

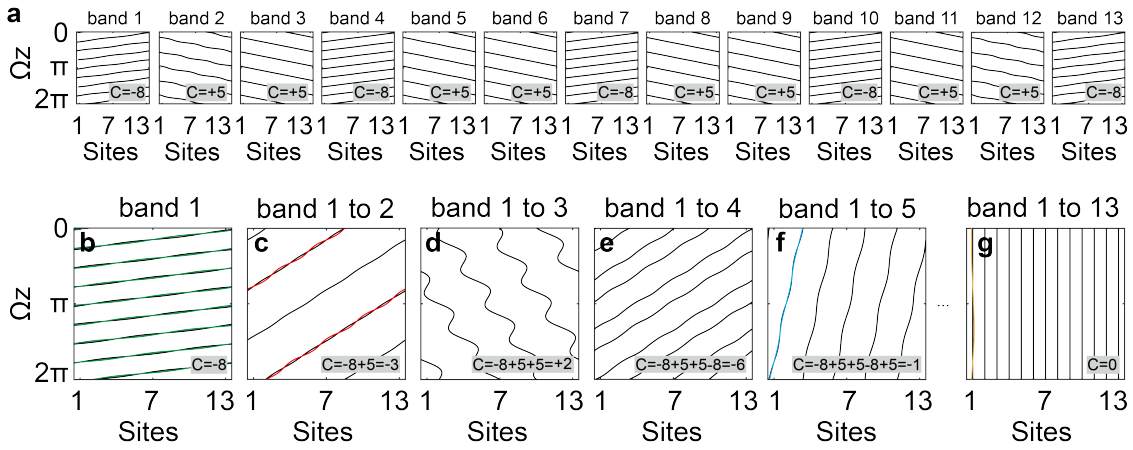

Figure 5.10. Wannier function positions of a 13 site AAH model. a, Center of mass position of single-band Wannier functions calculated for each of the 13 bands individually over one period and projected into a single unit cell. The number of windings is equal to the Chern number C of the corresponding band. **b-g**, similar to a but for multi-band Wannier functions in **c-g**, The position of pumped solitons from the plateaus of Fig. 5.9 at nonlinearities $gP/J^{\max} = 0.04$, 0.10, 0.78 and 3.08, are shown in green, red, blue and yellow, respectively.

pumping of $f = (-8+5)/2 = -3/2$. At even higher power, another fractionally pumped soliton emerges, which is described by the participation of the five lowest bands: $f = (-8+5+5-8+5)/5 = -1/5$. Finally, at very high power, the soliton is trapped as the strong nonlinearly induced on-site detuning effectively detaches the soliton from the lattice. Therefore, the soliton's displacement per period is zero [99]. In our framework this corresponds to the Chern number average of all bands, which is known to be zero in tight-binding models. We confirmed that, similar to Fig. 5.3b-d, all pumped solitons follow the center of mass positions of the respective maximally-localized multi-band Wannier functions (see Fig. 5.10).

5.6 Conclusion

In summary, we have theoretically predicted fractional pumping of solitons in nonlinear photonic Thouless pumps and experimentally observed a fractional f = -1/2 displacement. Furthermore, we have numerically shown the occurrence of a rich structure of multiple quantized plateaux of integer and fractional displacement. This is evocative of features of the fractional quantum Hall effect, which has recently been studied in similar but two-dimensional models with small bandgaps [131, 132]. The connection is particularly compelling in that both phenomena seem to require degenerate ground states (the solitons

residing below the lowest band are nonlinear ground states and their eigenvalues are degenerate at certain points within the pumping cycle). That said, our results here occur for effectively attractive bosons described by a localized mean-field single-particle wavefunction. This result implies that the fractionalization of transport in interacting topological systems is perhaps more general than was previously understood in the context of the fractional quantum Hall effect.

While finalizing the experiments of this chapter, we became aware of a related theoretical work [133].

Chapter 6
Fractional many-body Thouless pumping

This chapter describes fractional fermionic Thouless pumping with an integer filling fraction. Conventionally, in such Thouless pumps transport is dictated by the integer winding of single-band Wannier states. Although, multi-band Wannier states with fractional winding can be mathematically constructed, they cannot be adiabatically followed due to a varying band projection. Here, we show that repulsive interactions can stabilize a Mott insulator state in a Thouless pump at integer filling, such that only every second multi-band Wannier state per unit cell is occupied. Due to the fractional winding, the average pumped charge per period at intermediate adiabaticity is fractional and integer quantized only after multiple periods. We use exact diagonalization supplemented by density matrix renormalization group calculations to illustrate the concept in few-particle systems. This chapter is based on work that was done in collaboration with Jacob Steiner, Gil Refael, and Mikael C. Rechtsman.

6.1 Introduction

Thouless pumps [29] are dimensionally reduced versions of Chern insulators with analogue topology; they can be obtained from their two-dimensional counterpart by replacing one wavevector dimension with a time-periodic modulation. In Thouless pumps, topology manifests through a quantization of particles transport: per cycle, an integer number of particles are transported through any cross-section, dictated by the Chern number(s) of the occupied band(s). Being spatially one-dimensional systems, Thouless pumps can be advantageous to study experimentally, and have been observed in a variety of platforms [41], including fermionic and bosonic ultra-cold atoms in lattices [45, 46], as

well as in photonic waveguide arrays [44].

In Thouless pumps, transport is integer quantized for isolated filled bands, given an adiabatic modulation [29]. In electronic Thouless pumps integer quantization is protected even in the presence of substrate disorder and many-body interactions – as long as the (many-body) bandgap stays open [30]. Recent experimental studies have investigated the breakdown of quantization due to interactions [56] as well as interaction induced quantization [134]. For bosons, it has been suggested that quantization persists in the presence of interactions as long as the superfluid phase is avoided [54]. Similar to the fractional quantum Hall effect [32], interactions in combination with fractional fillings can lead to the emergence of fractionally quantized transport. Fractional pumping has been theoretically studied in the thin-torus limit of two-dimensional fermionic [135, 136] as well as bosonic [137] systems. In these studies, fractional fillings lead to the formation of degenerate charge density waves with periodicities of multiple lattice constants. One exception is the experimental observation of fractional Thouless pumping of solitons in waveguide arrays based on attractive bosons [2].

Here, we show fractionally quantized transport in interacting Thouless pumps with few particles at integer filling (and hence limited system size). Fractional quantization occurs at intermediate modulation frequencies, when the many-body wavefunction occupies every second multi-band Wannier state within a unit cell, whose windings are fractional. Fractional pumping occurs within a degenerate ground state manifold but without breaking translation symmetry in real space. We illustrate the concept numerically in few-particle systems using exact diagonalization simulations, supplemented by a density-matrix-renormalization group analysis.

6.2 The model

We demonstrate fractional Thouless pumping using an interacting, spinless, off-diagonal version of the Aubry-André-Harper (AAH) model [62, 63]. The Hamiltonian is given by $H(t) = H_0(t) + H_{\text{int}}$ with:

$$\begin{aligned} H_0(t) &= -\sum_n J_n(t)\hat{c}^\dagger_{n+1}\hat{c}_n + c.c. \\ H_{\text{int}} &= \sum_{n,i} U_i \hat{n}_n \hat{n}_{n+i}, \end{aligned} \tag{6.1}$$

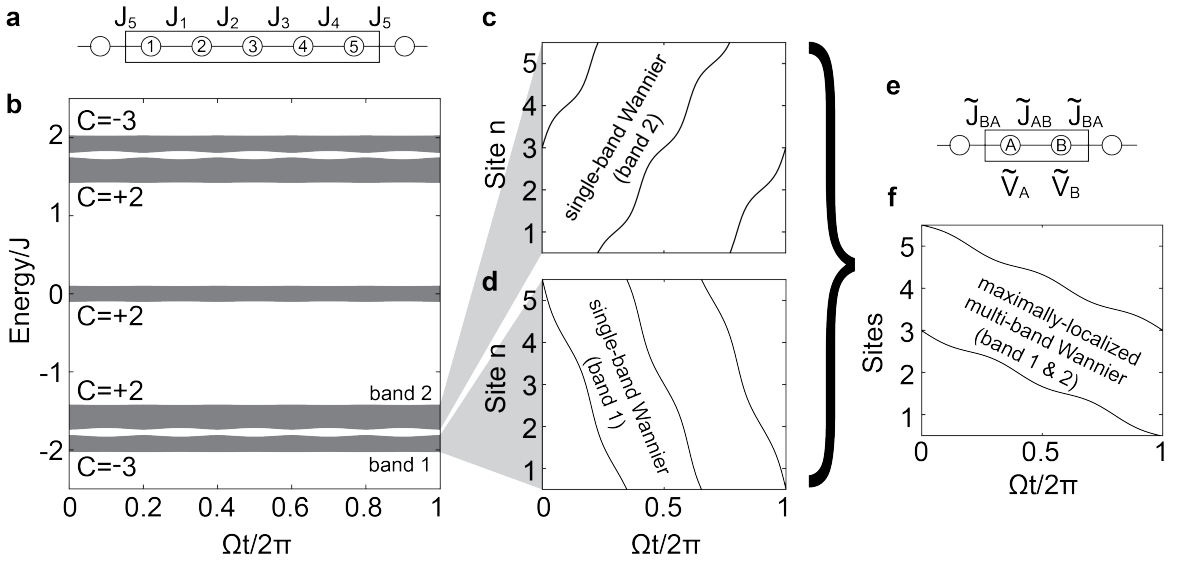

Figure 6.1. Properties of the noninteracting AAH-model. **a**, Schematic of the off-diagonal AAH-model with (time-periodic) nearest neighbor hoppings $J_n(t)$ and five sites per unit cell. **b**, Band structure of the noninteracting model showing five bands with Chern numbers $C = \{-3, +2, +2, +2, -3\}$. Band 1 and 2 are close in energy and well separated from all other bands. **c**,**d**, Center of mass of the single-band Wannier functions of band 1 (**d**) and band 2 (**c**) projected into a single unit cell. The number of windings is equal to the Chern number of the band. **e**, Schematic of the model in Wannier space with (time-periodic) nearest neighbor hoppings $\tilde{J}_{AB}$ and $\tilde{J}_{BA}$ and (time-periodic) on-site potentials $\tilde{V}_A$ and $\tilde{V}_B$. **f**, Center of mass of the maximally-localized multi-band Wannier states of the lowest two bands. Note the individual fractional winding, but the combined integer winding.

where *c.c.* denotes the complex conjugate, $\hat{c}_n^\dagger$ ($\hat{c}_n$) is the fermionic creation (annihilation) operator on site n, $\hat{n}_n$ is the particle number operator on site n and U_i describes the strength of interactions between fermions at nearest neighbor (i=1), next nearest neighbor (i=2) sites and so on. The noninteracting Hamiltonian, $H_0(t)$, describes a Thouless pump; we choose an AAH-model with five sites per unit cell and time-periodic nearest neighbor hopping strengths $J_n(t) = J + K\cos(\Omega t + 4\pi n/5)$. $\Omega = 2\pi/T$ defines the frequency of the periodic modulation with period T and goes to zero in the limit of adiabatic driving. A schematic of the noninteracting AAH model is shown in Fig. 6.1a. For definiteness, we choose $K/J = 0.7$ in the following unless otherwise stated and we will work with integer filling of $\nu = 1$, that is, the number of particles equals the number of unit cells.

In the adiabatic limit of slow driving the behavior of Thouless pumps can be conveniently analyzed using the instantaneous eigenstates. Before turning towards the interacting model, we discuss the simpler, noninteracting case ($U_i = 0$). The band structure of the off-diagonal AAH model is shown in Fig. 6.1b and consists of five bands.

We chose this model because the lowest two bands lie close together in energy, but are well separated from all higher energy bands. In the following, our focus lies on the lowest two bands. The topological quantization of transport in Thouless pumps is intimately related to the winding of Wannier states. In particular, the winding of the center of mass trajectory of the instantaneous single-band Wannier states projected into a single unit cell is equal to the Chern number and the transported charge per period – given a Fermi level in a bandgap. For single bands, there exists one Wannier state per unit cell and, in Fig. 6.1c,d, we show exemplary the winding of the Wannier states of the lowest two bands, with Chern numbers of $C = -3$ (band 1) and $C = +2$ (band 2). Importantly, the center of mass position of single-band Wannier states is gauge invariant and the projection of a Wannier state onto the respective band is uniform, such that single-band Wannier states can be adiabatically followed. Intuitively, given a filled band, one can think of each Wannier state in each unit cell being occupied and being displaced by the Chern number during one pumping cycle.

If multiple bands are filled (i.e. the Fermi level is in a higher bandgap), multi-band Wannier states are defined, whose number per unit cell is equal to the number of bands involved. In contrast to single-band Wannier states, their center of mass trajectories are gauge dependent. However, the sum of the windings is gauge invariant and equal to the sum of the Chern number of the bands involved. In Fig. 6.1f we show the trajectories for the maximally-localized multi-band Wannier states of the lowest two bands. Each individual multi-band Wannier state shows fractional winding of -1/2; when summed, this is equal to the sum of the Chern number of the lowest two bands $C_{1-2} = -3 + 2 = -1$. Importantly, this does not allow the observation of fractional quantization in noninteracting systems as multi-band Wannier states with a fractional winding have a varying band occupation over the pumping cycle and therefore cannot be followed adiabatically. We should intuitively always think about all multi-band Wannier states being occupied, once multi-band Wannier states play a descriptive role in non-interacting systems. Hence, integer quantization is recovered. Only recently, the fractional winding has been exploited to observe fractional soliton pumping in bosonic systems with attractive interactions using solitons [2] but its implication on Thouless pumping in interacting electronic systems is unclear.

6.3 Wannier picture

Famously, it has been shown by Niu and Thouless, that – starting from a system with integer filling – transport in Thouless pumps stays integer quantized as long as interactions do not close the bandgap [30]. Hence, fractionalization needs a novel concept. Previously, this has been achieved by fractional fillings that lead to the formation of charge density waves that break translation symmetry [135–137]. Here, we work in the regime, in which the interactions exceed the bandgap, e.g. the interactions close the bandgap between the lowest two bands, but not for higher bands and we will only focus on the lowest two bands in the following. Our goal is to take advantage of repulsive interactions to form a Mott insulator in Wannier space, such that only every second maximally-localized multi-band Wannier state within one unit cell is occupied (given $\nu = 1$). If such an occupation can be followed adiabatically, charge is transported according to the trajectory of the multi-band Wannier states, that is, fractionally quantized.

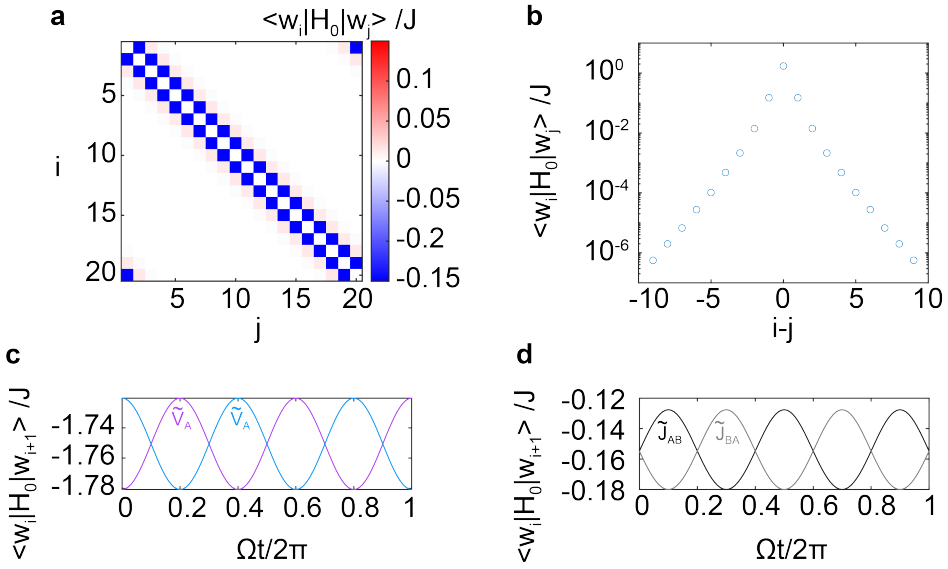

Figure 6.2. Wannier expansion coefficients. **a**, Expansion of $H_0(0)$ in the basis of instantaneous maximally-localized multi-band Wannier states of the lowest two bands. The labels i and j label the multi-band Wannier states in increasing order by their position in the lattice. Diagonal elements are not shown. **b**, Horizontal slice through **a**, that shows the exponential decay of the hopping strengths as a function of distance between Wannier states. **c**, On-site potential in Wannier space during one period. **d**, Nearest neighbor hopping in Wannier space during one period.

Assuming such interactions, we treat the lowest two bands as a composite energy band and write Eq. (6.1) in the basis of the respective maximally-localized multi-band Wannier

states. Importantly, this means that a static state within this basis is actually moving according to the fractionally winding trajectory. We show the expansion graphically in Fig. 6.2. Keeping only the dominant nearest neighbor hopping terms (longer-range hoppings fall off exponentially; see Fig. 6.2a,b), the noninteracting part of the Hamiltonian, restricted to the two lowest two bands, is given by

$$H_0 = \sum_{R,\alpha} \tilde{V}_\alpha \hat{w}^\dagger_{\alpha,R} \hat{w}_{\alpha,R} + \sum_{\substack{\text{Nearest} \\ \text{neighbor}}} \tilde{J}_{\alpha,\alpha'} \hat{w}^\dagger_{\alpha,R} \hat{w}_{\alpha',R'}, \tag{6.2}$$

where $\hat{w}^\dagger_{\alpha,R}$ ($\hat{w}^\dagger_{\alpha,R}$) creates (annihilates) a maximally-localized multi-band Wannier state. $\alpha \in \{A, B\}$ denote the two types of multi-band Wannier states per unit cell (which we will refer to as "flavors"), labelled by the lattice vector R. The summation in the second line is restricted to nearest neighbors and we omit to write the explicit time dependence of all terms. Equation (6.2) describes a Rice-Mele model [116] with a two-site unit cell, on-site potentials $\tilde{V}_\alpha$ and nearest neighbor hoppings $\tilde{J}_{\alpha,\alpha'}$. A schematic of this model is shown in Fig. 6.1e. Importantly, the sites are not physical sites, but represent the maximally-localized multi-band Wannier states, that can be localized over more than one site and are moving during the pumping cycle dictated by the fractional winding.

Expressing the interacting part of the Hamiltonian in the basis of multi-band Wannier states is more complicated, and to be able to proceed we make the following assumption: Due to the exponential localization of the Wannier states, we assume that the most dominant interaction occurs between nearest neighbor Wannier states. Furthermore, restricting ourselves to the two lowest bands, results in:

$$H_{\text{int}} = \sum_{\substack{\text{Nearest} \\ \text{neighbor}}} \tilde{U}\, \hat{n}_{\alpha,R} \hat{n}_{\alpha',R'} \tag{6.3}$$

with interaction strength $\tilde{U}$ between nearest neighbor Wannier states and $\hat{n}_{\alpha,R} = \hat{w}^\dagger_{\alpha,R} \hat{w}_{\alpha,R}$. In the following we analyze the properties of the simplified model in Wannier space (Eqs. (2) and (3)). Later, we will compare it with the results obtained via exact diagonalization of Eq. (6.1).

In the limit of strong interactions ($\tilde{U} \gg (\tilde{V}, \tilde{J})$), we can treat the noninteracting part H_0 as a perturbation to the interacting part H_{int} of the Hamiltonian. To zeroth order (neglecting H_0), there exists a degenerate ground state manifold of two states with zero energy, well separated from all other states, given by: $|\Psi_A\rangle = \prod_R \hat{w}^\dagger_{R,A} |\emptyset\rangle$ and $|\Psi_B\rangle = \prod_R \hat{w}^\dagger_{R,B} |\emptyset\rangle$, where $|\emptyset\rangle$ denotes the vacuum. Including first order corrections

from the on-site potential term in Eq. (6.2), the energies of the two ground states split into $E_A = N_p\tilde{V}_A$ and $E_B = N_p\tilde{V}_B$, where N_p is the number of particles, that equals the number of unit cells for $\nu = 1$. Despite their splitting, we will continue to refer to the two states as ground state manifold, as long as they are separated from higher energy states. For finite interaction strength the energy of the first excited state is (assuming $\tilde{V}_A < \tilde{V}_B$): $E_E = \tilde{V}_A \cdot (N-1) + \tilde{V}_B + \tilde{U}$. Thus, the energy gap, ΔE_E, between the ground state manifold (using $N_p \cdot E_B$) and the first excited state is linearly decreasing with N_p, as:

$$\Delta E_E = (\tilde{U} + \Delta) - \Delta \cdot N_p, \tag{6.4}$$

where we have defined $\Delta = (\tilde{V}_B - \tilde{V}_A)$.

Assuming that, during the pumping cycle, there is a point of $\Delta = 0$ and small but finite hopping, $\tilde{J} \ll \tilde{U}$ (see Fig. 6.2c,d), the two states in the ground state manifold hybridize through higher order hopping processes of order N_p, resulting in a gap, ΔE_G, that scales as

$$\log(\Delta E_G) \propto -N_p \tag{6.5}$$

We conclude that, in principal, this model fulfils the necessary requirements for fractional pumping: In the moving frame of multi-band Wannier states, there exist two degenerate Mott insulator type ground states, that are – for finite systems – gapped from excited states. In the following, we use exact diagonalization to verify these predictions and analyze the model exactly.

6.4 Exact diagonalization results

Using exact diagonalization we solve Eq. (6.1) for the eigenstates for an interacting, few-particle system and at integer filling of $\nu = 1$, that is, with as many particles as unit cells. The resulting many-body band structures for N_p=2,3,4 and 5 particles are shown in Fig. 6.3a-d, respectively. We find a ground state manifold of two states separated from higher energy states. As expected, each of the two many-body eigenstates in the ground state manifold shows substantial overlap with only one of the two instantaneous maximally-localized multi-band Wannier states. We quantify this by calculating the "Wannier contrast" between the projections onto the two multi-band Wannier states, defined as $(I_A - I_B)/(I_A + I_B)$, where $I_\alpha = \sum_R \langle\Psi| \hat{n}_{\alpha,R} |\Psi\rangle$, with $|\Psi\rangle$ being the respective many-body eigenstate. In Fig. 6.3a-d, blue (purple) color means that the state is made up by one flavor of Wannier states, while black has projections onto both flavors.

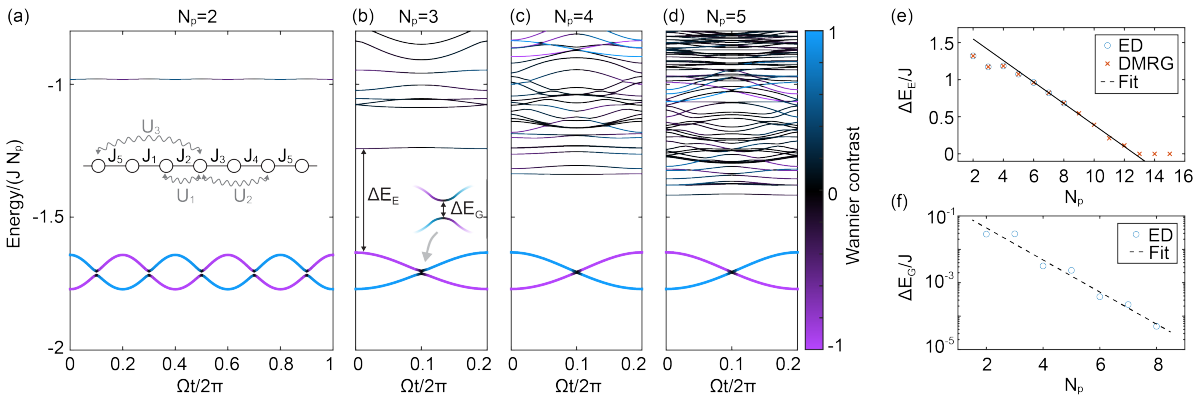

Figure 6.3. Many-body band structure of an interacting few-particle Thouless pump. a-d, Band structures for N_p=2,3,4 and 5 particles in a system with 2,3,4 and 5 unit cells, respectively. Each line represents the energy of an interacting many-body eigenstate as a function of the pump parameter. Color coding represents the projection strength of the many-body eigenstate onto the maximally-localized multi-band Wannier states. Note that **a** shows one full pumping cycle, while **b-d** only show one fifth of a pumping cycle. The inset in **a** shows a schematic of the AAH model with nearest neighbor hoppings J_n and interactions U_i. The inset in **b** defines the bandgap within the ground state manifold ΔE_G, and between the ground state manifold and the first excited state ΔE_E. **e**, bandgap between the ground state manifold and the first excited state as a function of particle number for $\Omega t/2\pi$=0. Circles represent exact diagonalization (ED) results and crosses represent DMRG calculations. The linear fit is based on N_p=6 to 12. **f**, bandgap within the ground state manifold as a function of particle number N_p for $\Omega t/2\pi = 0.1$. Here, $U_1/J = 40$, $U_2/J = 10$, $U_3/J = 3$ and $K/J = 0.7$. Note that, for better comparison, **a-d** show the energy per particle.

Importantly, note that, while the system comes back to itself after each period, the color coding does not, as the Wannier states are exchanged after each period due to their fractional winding.

With increasing particle number (and corresponding system size), the energy gap between the ground state manifold and the first excited state, ΔE_E, decreases (see Fig. 6.3f). We extend our calculations to larger particle numbers using DMRG (density matrix renormalization group) calculations and find that the energy gap decreases linearly before the bandgap eventually closes, as predicted by Eq. (6.4). Furthermore, we evaluate the energy splitting within the ground state manifold, ΔE_G, using exact diagonalization that shows an exponential decrease as a function of particle number/system size (agreeing with Eq. (6.5) and shown in Fig. 6.3e).

Having demonstrated that the instantaneous eigenstates are in agreement with our simplified model in Wannier space, we are left to show that those eigenstates can be adiabatically followed. The calculated band structure of the instantaneous many-body eigenstates supports the following crucial observation: There exist two adiabatic time

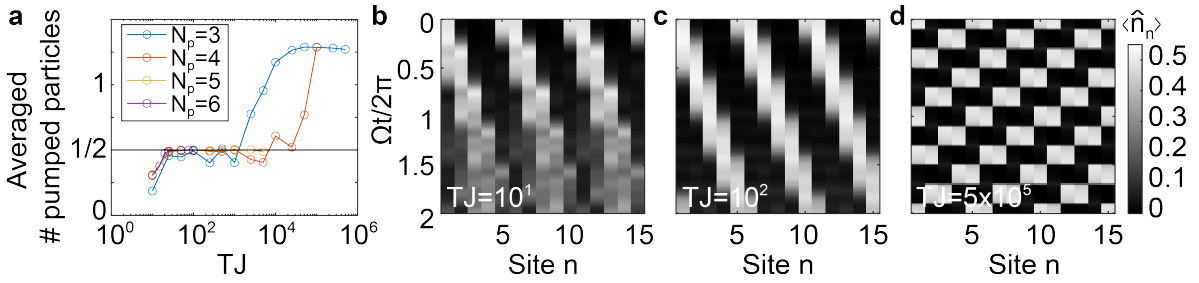

Figure 6.4. Integrated current. **a**, Number of pumped particles averaged over two periods for increasing system size but constant filling factor of one particle per unit cell ($\mu = 1$). **b-d**, One particle density matrix for three different driving regimes: fast driving (**b**) with excited state excitations; intermediate adiabaticity (**c**), where the bandgap in the ground state manifold can be crossed, but not the bandgap to the excited states; and adiabatic limit (**d**), where not even the bandgap within the ground state manifold can be crossed. Parameters are identical to Fig. 6.3.

scales: First, in the adiabatic limit ($T \to \infty$) a wavefunction initially prepared to be in the lowest energy eigenstates will rigorously follow the lowest energy eigenstate within the ground state manifold. Second, there exists an intermediate adiabatic regime, where the wavefunction can cross the (exponentially suppressed) bandgap within the ground state manifold, while excitations to any other states are negligible. In this regime, the wavefunction follows one of the multi-band Wannier states (i.e. the purple line). Importantly, this means that the the wavefunction needs two periods to come back to itself (as purple turns into blue and vice-versa after each period). This is because the multi-band Wannier states are only pumped by a fraction of a unit cell and end up in the other flavor after a single pumping cycle. Therefore, we expect fractional pumping after a single period and integer quantized pumping only after after two periods.

We confirm this behavior by numerically solving the time-dependent Schrödinger equation as a function of adiabaticity and particle number. We calculate the integrated current, $J(t)$, over two periods via $J(2T) = \int_0^{2T} dt\, i \langle \Psi(t)| J_n(t)\hat{c}_n^\dagger \hat{c}_{n+1} - J_n(t)\hat{c}_{n+1}^\dagger \hat{c}_n |\Psi(t)\rangle$. For a meaningful comparison with traditional Thouless pumps, we plot the averaged number of pumped particles per period in Fig. 6.4a. For fast and slow driving (small and large T), the integrated current is non-quantized. However, for intermediate driving speeds, the current forms a plateau at 1/2. With increasing particle number, this effect becomes more pronounced, as the bandgap within the ground state manifold becomes (exponentially) smaller and therefore easier to cross.

To gain further insight, we plot the density distribution of the propagated wavefunction for the three regimes over two pumping cycles: At fast driving, excitations to higher

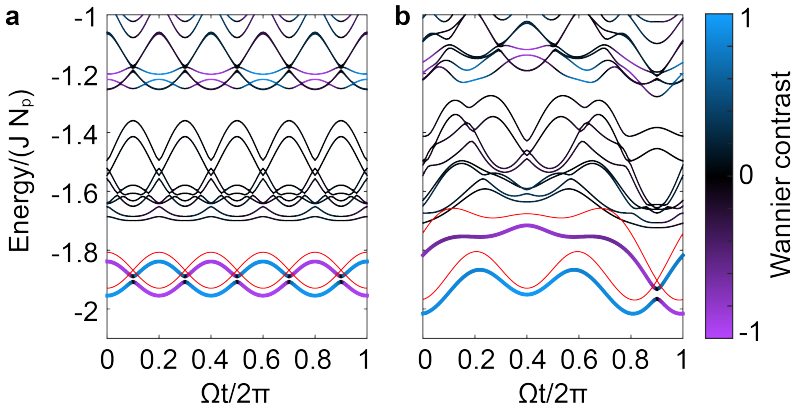

Figure 6.5. Analysis of the band crossings. **a**, Three particle band structure, similar to Fig. 6.3b. The red lines represents E_A and E_B. **b**, Same as **a**, but for slightly disturbed parameters ($J_1 \to J_1/1.5$ and $J_2 \to J_2/1.5$) that gap out two pairs of crossings. Here, $U_1/J = 10$, $U_2/J = 2.5$ and $K/J = 0.9$.

states occur, which is visible in the "smearing out" of the density in Fig. 6.4b. In the intermediate pumping regime, the wavefunction clearly shows a different density pattern after one cycle, and needs two periods to come back to itself (see Fig. 6.4c). Importantly, this is different from a typical charge density wave, as the integrated density per unit cell is uniform and translation symmetry is not broken. In the adiabatic limit, the wavefunction rigorously follows the lowest energy eigenstate, switching five times between the two flavors of Wannier states during one cycle (see Fig. 6.4d).

To observe fractional pumping, the wavefunction has to switch character after each period. Thus, there must be an odd number of crossings within the ground state manifold. To analyze the number of crossings within the ground state manifold, we show an exemplary many-body band structure in Fig. 6.5a (similar to Fig. 6.3a, but for $U_3 = 0$) with five crossings per period. By modifying $J_1(t) \to J_1(t)/1.5$ and $J_1.5(t) \to J_2(t)/2$, we deform the band structure, such that two pairs of crossings annihilate each other and we are left with only one crossing in Fig. 6.5b. This behavior can be understood from Eq. (6.2). In the Mott insulator state, the energies are dominated by the on-site energies E_A and E_B as shown by the red lines in Fig. 6.5a and b. It remains to be argued that at least one crossing must occur. Given a model where the multi-band Wannier states have fractional winding, we know that one state has to turn into the other after each period. Thus, at least one crossing must exist.

Furthermore, we suggest a way to extend our results into the thermodynamic limit: Although the system's bandgap closes for increasing system size at fixed interaction strengths, when fine-tuning the interactions such that interactions between Wannier

states of different flavors (and to all Wannier states of higher bands) are infinite, the bandgap will not close even in the thermodynamic limit. This situation is similar to the case of hard-core bosons (where the on-site interaction strength is infinite), which can be described as noninteracting fermions. Similarly, in our case, the interacting fermions turn into hard-core multi-band Wannier state crystals and follow their fractional winding. In this case, during the first cycle, the Wannier states of flavor $\alpha = A$ will be occupied and in the subsequent cycle Wannier states of flavor $\alpha = B$. Hence after two periods the projection onto the two lowest band will be uniform.

Finally, we comment on the relation of our work with the fractional quantum Hall effect. While noninteracting Thouless pumps have a well defined connection to their two-dimensional counterpart, the integer quantum Hall effect, via dimensional extension (the opposite of dimensional reduction), no such rigorous connection has been established for interacting Thouless pumps and the fractional quantum Hall effect. However, in the thin-torus limit of the fractional quantum Hall effect, the Laughlin state continuously transitions into the charge-density-wave-like Tao-Thouless state [138–140]. A pumped charge density wave can therefore be regarded as the interacting Thouless pumping analogue of the fractional quantum Hall effect. However, due to the effective 1/2 filling, we do not expect the described fermionic state to be adiabatically continuable into a two-dimensional fractional quantum Hall state. Instead, a different model with three energetically closely lying bands and effective 1/3 filling is necessary. This is supported by Ref. [132], that has shown the emergence of a fractional Chern insulator state in a two-dimensional Harper-Hofstadter model with integer filling but three closely almost degenerate bands and therefore effective 1/3 fractional filling. Similar results have also been reported in Ref. [131].

6.5 Summary & Outlook

In summary, we introduced fractional Thouless pumping at integer fillings. For suitable interactions exceeding the bandgap, only every second multi-band Wannier state per unit cell is occupied and, due to their fractional winding, transport is integer quantized only after multiple periods. We illustrated the concept in few-particle systems, using exact diagonalization calculations. Our work bridges the gap between the recently observed fractional Thouless pumping of solitons (attractive bosons) and fermionic systems with repulsive interactions and highlights intriguing physical consequences of the fractional winding of multi-band Wannier states.

Chapter 7
Towards deep-etched photonic structures in doped YAG

This chapter describes the experimental advances in the development of a fabrication technique for deep-etched photonic structures in doped YAG (yttrium aluminium garnet). We use femto-second laser writing to create a large etching sensitivity for a subsequent chemical wet-etching process, that in principle enables the fabrication of two-dimensional photonic crystals with large refractive index contrast. We analyze the effects of the most important fabrication parameters on the structures, show selected results and discuss future improvements.

7.1 Introduction

In the previous chapters, we used direct femto-second laser writing to create waveguide arrays in borosilicate glass: By translating the sample through the focal spot of a high-power laser beam, the local refractive index changes. When using suitable materials (like borosilicate glass), the refractive index increases and, due to index guiding, optical waveguides can be fabricated in the bulk with a large degree of customizability. However, this process only leads to relatively small (on the order of 10^{-3} to 10^{-2}) refractive index changes. Distinctly different physics emerges for large refractive index changes. For example, periodically varying the refractive index profile in one (two, three) dimensions allows to deliberately engineer the photonic density of states. For a pronounced effect, the lattice constant has to be smaller or equal to the wavelength. Furthermore, as a rule of thumb, the larger the index contrast, the more pronounced the effect. Such structures are called photonic crystals (in analogy to condensed matter crystals) and engineering the photonic density of states results in a variety of interesting physical effects, like photonic

bandgaps, Purcell enhancement, or defect modes [85]. Despite their theoretical promise, large two- and three-dimensional photonic crystals are challenging to fabricate. Amongst others, multi-photon stimulated photopolymerization has been shown [141, 142], but those methods are incompatible with common crystalline materials and new fabrication methods are highly sought after.

In this chapter, we use direct femto-second laser writing to create a large etching selectivity between the pristine and the photo-irradiated parts of a YAG crystal. In a subsequent wet-etching process, only the pristine material remains, resulting in photonic crystals with a refractive index contrasts of 1:1.83. The material of choice for this chapter is YAG ($Y_3Al_5O_{12}$), a synthetic crystal with high thermal and mechanical robustness. YAG has become increasingly popular over the last decades as solid-state gain material for lasers, when dopants are added, such as Nd (Neodymium), Tm (Thulium), Er (Erbium), Cr (Chromium), Yb (Ytterbium), or Ho (Holmium). Furthermore, a doping with Ce (Cerium), makes YAG:Ce a fast scintillator (decay constant 70 ns), that efficiently converts radiation (e.g X-rays) into photons in the visible regime (550 nm). While the surface of YAG:Ce has recently been patterned (using focused ion beam) to increase the out-coupled scintillation yield and resolution [143], the effect of volumetric patterning on scintillation is largely unexplored. Recently, a theoretical framework [144] and first experiments for one-dimensional photonic crystals have been reported [145].

For undoped YAG, femto-second laser writing has shown to create an etching selectivity of more than 10^{-5}, which means, that the photo-irradiated YAG crystal etches more than 10^5 times faster than pristine YAG [146]. This permits reasonable etching times for the irradiated YAG on the order of $\approx$100 μm per hour. In principle this allows to create large and arbitrary two-dimensional, as well three-dimensional photonic crystals. This is remarkable, as typical fabrication techniques, such as laser lithography, as used in the semiconductor industry, only pattern the surface of structures, and are incompatible with materials like YAG. In their work in Ref. [146], Ródenas and co-workers showed that etching of centimeter-long structures is possible, with feature sizes down to 100 nm (see also Ref. [147]). However, due to the chosen transverse writing configuration, large arrays were out of reach, and only index-guiding waveguides and gratings (which are surface effects) have been shown.

In the following, we will show how femto-second laser writing in the longitudinal configuration and subsequent wet-etching allows to fabricate large two-dimensional photonic crystals in doped YAG with sub-micron lattice constants, few-hundred nanometer feature sizes, and up to mm-long depth. We anticipate that our findings will enhance

the efficiency of scintillation in Cerium-doped YAG. Additionally, it could enable other materials such as Yb-doped YAG to improve their scintillation yield, making them potential choices for scintillators.

7.2 Fabrication and surface effects

We use femto-second laser writing in the longitudinal configuration, as illustrated in Fig. 7.1), and write parallel to the axis of the laser beam. While this configuration limits the length of the structures to the working distance (WD) of the objective (times the refractive index of the material), making it unsuitable for evanescently coupled waveguide arrays, it offers two main advantages: (1) The circular cross-section of the beam results in circular holes after etching. (2) It allows the fabrication of large arrays of identical waveguides. Both (1) and (2) are in stark contrast to the transverse writing configuration, where writing large, dense arrays of circularly shaped waveguides is challenging. In the previous chapters, we addressed this challenge using a slit, which improved the circularity of the cross-section at the expanse of a larger focal spot size. However, this is not a viable option here, as we are aiming for minimal cross-sections. Without the slit, Ródenas [146] demonstrated almost circular features using a high numerical aperture (NA=1.4) oil-immersion objective in combination with a laser power slightly above the modification threshold power. The downside is the need for an extremely fine-tuned power and the method's limited applicability within a small depth range, preventing the fabrication of large arrays.

When writing in the longitudinal configuration, the beam is initially focused onto the bottom of the sample. Subsequently, the sample is moved downward, causing the focal spot to move upward within the sample. We observed that this writing technique leads to the formation of craters (see Fig. 7.2) on the upper surface, a phenomenon known as laser ablation [148]. As these craters can impact the writing process of neighboring sites, we prevent their formation by reducing the laser power just before the laser focus reaches the upper surface. Initial tests using an external mechanical shutter, showed that the delay time between the command to close and the performed closing of the shutter required careful calibration for different speeds. Consequently, we moved to utilize the internal acousto-optic modulator (AOM) of the fabrication laser, which has a maximum modulation frequency of 80 MHz. This allows us to (essentially) instantaneously reduce the power fine-tune the laser power as a function of writing depth. Since the waveguides are buried within the bulk material and do not extend to the top surface, we manually

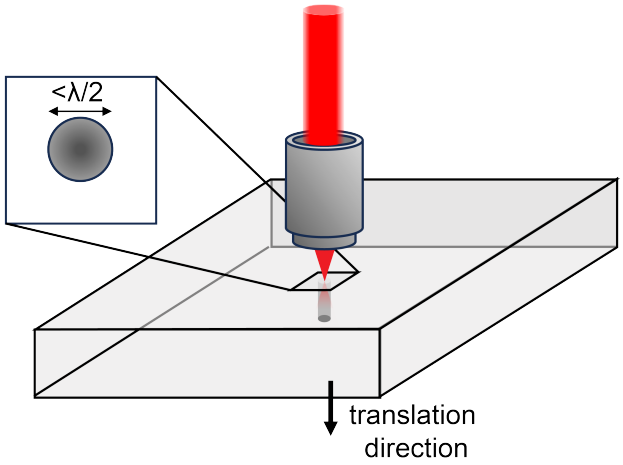

Figure 7.1. Direct femto-second laser writing in longitudinal configuration. The sample is translated parallel to the laser beam axis. Due to multi-photon processes, the material modification cross-section (as illustrated in the inset) can be below the linear diffraction limit.

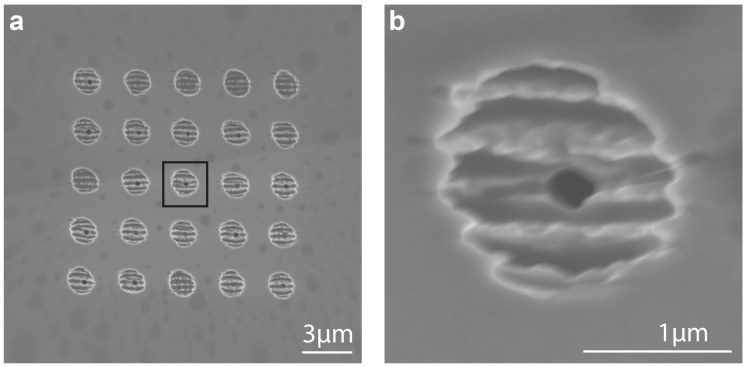

Figure 7.2. Formation of surface craters. **a**, SEM image of a 5x5 array after etching. **b**, Zoomed-in image of a single crater of diameter $>1\,\mu$m and corresponding hole (black) in the center.

expose them by grinding/polishing the crystal with diamond sanding paper. Once the surfaces are exposed, we etch the photonic structures using phosphoric acid in deionized water (44 wt% H_3PO_4) at 78°C. Additional details of the fabrication procedure can be found in Appendix D.

We examine the resulting photonic structures through both an optical microscope and via a scanning electron microscope (SEM). The latter is mostly used to analyze and measure hole dimensions. Due to the challenge of locating individually written features, we typically write arrays. Crater formation, if present, is clearly visible under the optical microscope and is used to calibrate the writing position. In the absence of craters, unetched arrays can be observed in transmission. After etching, the etched

structures become easily visible in both reflection and transmission. To assess the etching depth, we use a side view. The structures are written close to the sample edge, but not too close to avoid edge effects while writing. For clearer results, polishing of the sides may be necessary, which we perform either before or after the writing process.

7.3 Calibration of writing power and etching depth

Our objective is to fabricate large, mm-deep arrays with sub-wavelength feature sizes and small lattice constants, which is strongly influenced by the focusing lens/objective and the writing power.

First, we discuss the choice of the focusing lens/objective. In principle, higher numerical aperture (NA) lenses/objectives allow tighter focusing, resulting in smaller feature sizes. However, an increasing NA comes with a reduction in working distance (WD), ultimately limiting the depth to which structures can be written. For instance, objectives with NA=1.4, typically have a working distance of <0.2 mm. In air, spherical aberrations, caused by the refractive index difference between air and YAG, become more prominent for higher NA objectives. This challenge can be overcome by using oil-immersion objectives for which the refractive index contrast is significantly smaller, reducing the effects of spherical aberrations. While experimenting with an oil-immersion objective (Nikon Plan 50x; NA=0.9, WD=0.35 mm), we observed that seemingly random waveguides were not etched. We attribute this to the movement of the oil during the fabrication process, which could impact the writing. Based on those experiences, we opted for using a NA=0.68, WD=1.8 mm lens (Thorlabs C330TMD-B), as a suitable trade-off between high NA, a sufficiently large WD, and ease of use.

Second, we discuss the power requirements. Because femto-second laser writing is based on a multi-photon process, feature sizes are not given or limited by the diffraction limit. Instead, they are a strong function of power. Thus, the fabrication power has to be carefully calibrated for small feature sizes, that are etched through the whole crystal at reasonably fast etching speed. In order to calibrate the power we write arrays of 10 by 10 waveguides close to the sample edge, using a fixed power per array, but varying the power between arrays. Fig. 7.3a shows an optical side view (in transmission), after about one hour of etching. Notably, the threshold power for etched structures at the bottom is higher, due to internal absorption as well as increasing spherical aberrations with depth, resulting to a lower peak power. Figure 7.3b,c further presents optical images of arrays at the top surface (90 mW) and the bottom surface (175 mW) after etching, respectively.

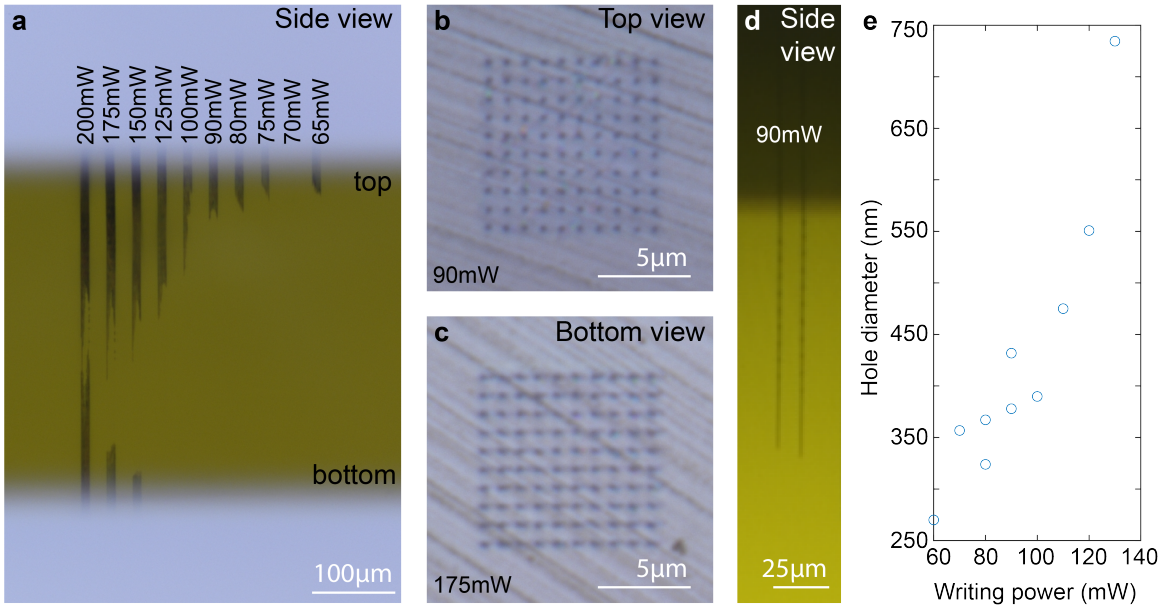

Figure 7.3. Calibration of writing power. **a**, Transmission microscopy side view image of 10x10 arrays written with constant power per array after about one hour etching. **b**, Optical microscopy image of the top surface showing an array written with 90 mW. **c**, Optical microscopy image of the bottom surface showing an array written with 175 mW. **d**, Optical microscopy side view image of two single waveguides written with 90 mW, showing a blob-like structure. **e**, Measured hole diameter as a function of writing power obtained from SEM images of the top surface.

Based on this measurement, we calibrate the fabrication power to be between 80 mW to 90 mW for the top surface and around 150 mW to 175 mW at the bottom surface and use a linear interpolation in between. All power measurements reported within this chapter are measured before the focusing lens.

We also analyze single waveguides at a typical writing power of 90 mW. We find that the etched structures exhibit a distinct recurring blob-like pattern, resembling pearls on a string (see Fig. 7.3d). This pattern seems to be dependent on the writing power, and while the exact reason for its occurrence is not known, our observations suggest that the writing parameter regime might require optimization. The parameter space is extensive, and possible adjustments include the writing speed, the laser repetition rate, the laser wavelength, and temporal pulse length. Using single waveguides, we calibrate the etched hole size as a function of writing power, revealing that our fabrication configuration allows sizes down to ≈ 270 nm for writing powers of 60 mW. For typical writing powers in the range of 80 mW to 90 mW, sizes of < 400 nm are possible.

Additional challenges arise when writing arrays. Figure 7.4 shows SEM images of

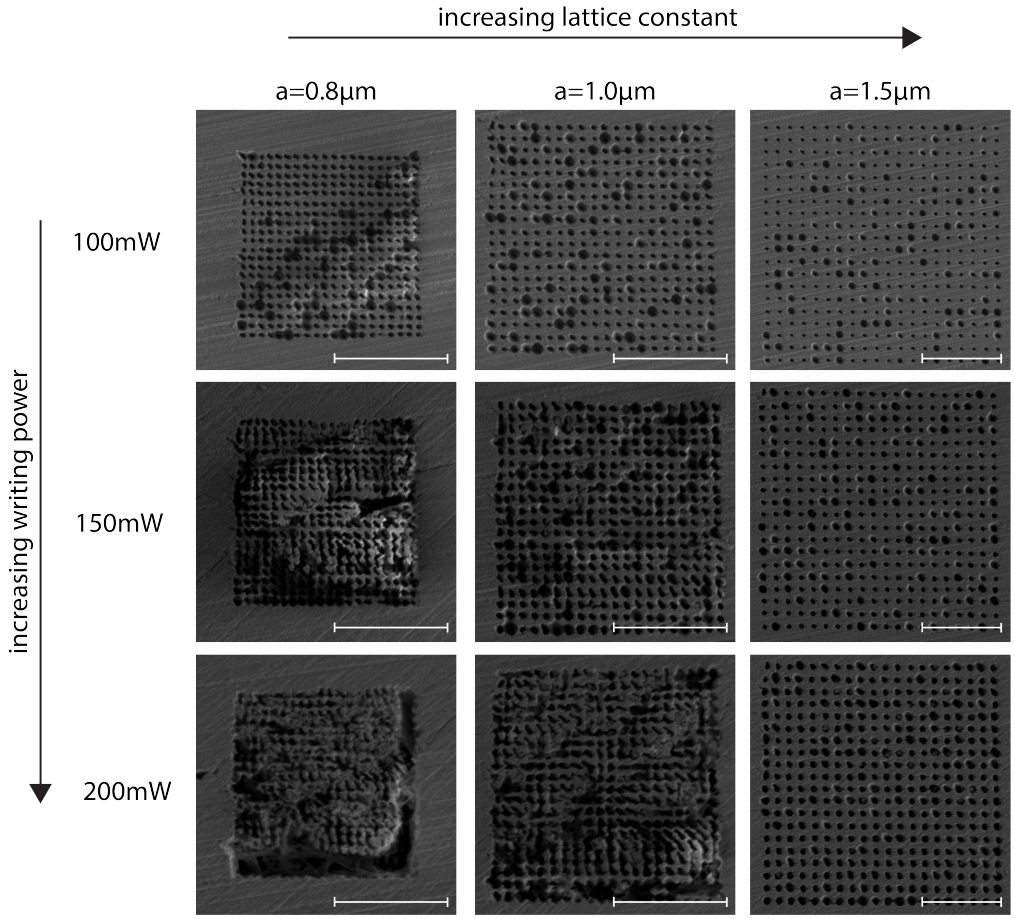

Figure 7.4. Influence of writing power and lattice constant. SEM images of arrays with lattice constant a=0.8 μm, 1.0 μm and 1.5 μm and writing powers of 100 mW, 150 mW and 200 mW. Clearly visible is the seemingly random size variation of the holes for 100 mW. The scale depicts 10 μm.

etched arrays at different lattice constants (a=0.8 μm, 1.0 μm and 1.5 μm) and writing powers (100 mW, 150 mW and 200 mW). We observe that is is necessary to use lower power for arrays with smaller lattice constant to maintain structural integrity. Furthermore, within one array, we note variations in hole sizes, consistent with our observation of the blob-like structure in single waveguides. Moreover, as the size of the arrays increases, the likelihood of creating cracks during writing also increases.

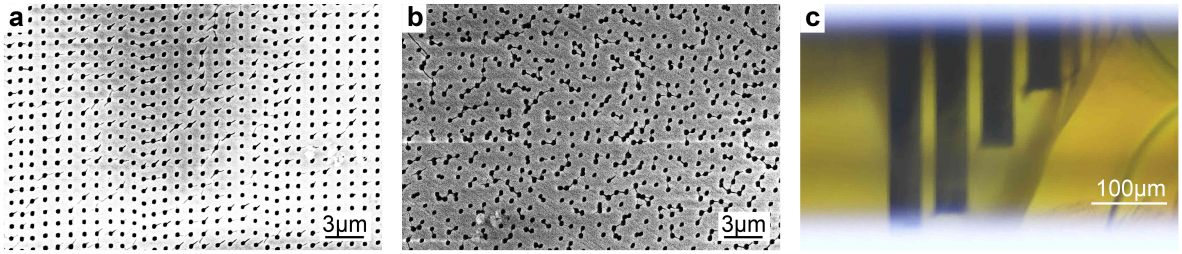

Figure 7.5. Selected etching results. a, SEM image of a part of a 150x150 square lattice array with lattice constant a=1 μm. Clearly visible is the fabrication disorder that stems from the large array size. Furthermore, micro-cracs between different holes are visible. **b**, Similar to **a**, but with strong random position disorder drawn from a random distribution [-0.4a,0.4a]. **c**, Optical microscope side view image of four arrays fabricated with depth-adjusted writing power and different starting depth.

7.4 Selected results

Finally, we present some obtained results that demonstrate the capability of the developed fabrication method to (1) write large arrays and (2) deterministically etch deep structures. In Fig. 7.5a,b we show parts of a 150 by 150 hole array (lattice constant 1 μm), arranged in a square lattice without and with nominal random disorder, respectively. The fabrication of the nominally disorder-free square lattice exhibits some fabrication disorder, which we attribute to imprecise stage movement and temperature changes, and becomes more pronounced with increasing array size. Additionally, micro-cracks between holes are visible. Both arrays in (7.5a,b are written with a fixed power of 85 mW. In Fig. 7.5c, we demonstrate that by adjusting the writing power as a function of the writing depth, and deterministically switching on/off the beam using the internal AOM, we are able to write arrays for different etching depths.

7.5 Conclusion and Outlook

In this chapter, we have presented experimental progress towards the fabrication of deep-etched photonic crystal structures in doped crystalline YAG. Femto-second laser writing was used to create a large etching sensitivity between pristine and the photo-irradiated YAG, that was exploited in a subsequent wet-etching step. We successfully etched large arrays of 300x300 sites, and established an experimental procedure to etch structures with varying etching depth. This capability may be crucial in future to test observables as a function of etching depth, confirming a volume effect. For example, we anticipate

increasing scintillation yield with etching depth in volumetrically patterned scintillators when the density of states of out-coupled modes is increased.

Apart from Cerium-doped YAG (from crytur), we also successfully etched Ytterbium-doped YAG (from optogama; doping: 15%). The change in the dopant leads to a change in the scintillation emission wavelength from approximately 550 nm (Cerium-doped YAG) to around 1030 nm (Ytterbium-doped YAG), respectively. Therefore, for the same feature sizes, the photonic crystal effects are expected to be stronger in Ytterbium-doped YAG. While not described in detail here, we have irradiated etched and unetched Cerium-doped YAG structures with x-rays and observed scintillation enhancement. These measurements were conducted in collaboration with Sachin Vaidya, Charles Roques-Carmes and Simo Pajovic at MIT. However, the increased scintillation could not be unequivocally attributed to a volume effect, as there was no significant dependence on etching depth.

In the future, a significant effort needs to be undertaken to analyze the quality of the fabricated photonic crystals. A first analysis should involve looking for Bragg peaks to determine the quality of the photonic crystal. Second, a reliable method should be developed to image the cross-section of the etched holes and investigate the wall straightness of the etched structures. One possible approach might be to fabricate large arrays and mechanically break the etched crystal, ensuring that the break line passes through the patterned array. The broken structure could then be imaged using SEM to gain insight into the cross-section and sidewall roughness. Furthermore, the writing parameters may need systematic optimization. This includes the laser repetition rate, writing power, writing speed, and the choice of the focusing lens/objective. Testing different dopants with varying concentrations and exploring other etching solutions or a fabrication laser at a lower wavelength are further avenues for potential improvement. It is worth noting that it might be worthwhile to test materials that, in their unpatterned state, are not considered good scintillators but could prove more effective after patterning. We envision that our results will finally lead to the observation of volumetrically enhanced bulk scintillation.

Chapter 8
Summary

In this dissertation, we presented four studies examining interacting/nonlinear Thouless pumps and one study presenting advances in the fabrication of deep-etched photonic crystals.

We theoretically predicted and experimentally observed integer and fractionally quantized Thouless pumping of solitons. In both cases, the wavefunction's projection onto the band structure is decidedly non-uniform. This is in stark contrast to non-interacting systems, that require a strictly uniform band occupation for quantization. Hence, we have shown the emergence of quantization due to a new mechanism: Quantization occurs as the soliton solutions at the beginning and end of each period are identical – apart from translation invariance. Consequently, when a soliton comes back to itself after each period – modulo an integer number of unit cells – its displacement is integer quantized. For low power, we showed analytically that the movement of solitons tracks the trajectory of single-band Wannier states, whose winding is – by definition – integer quantized by the Chern number. At higher power, and when the interactions exceed the relevant bandgap, the soliton follows the trajectory of maximally-localized multi-band Wannier states, whose winding is fractional. In this case, the soliton comes back to itself only after multiple periods. Using evanescently coupled waveguides and high-power laser pulses, we observed integer soliton pumping by one unit cell with a transition to a trapped soliton at higher power due to symmetry breaking nonlinear bifurcations. In a separate experiment, we observed fractional soliton pumping by -1/2 unit cells after one period and -1 unit cell after two periods. We furthermore extended the concept of fractional Thouless pumping from the nonlinear bosonic platforms into the strongly-interacting regime and showed fractional pumping also in fermionic few-particle systems at integer filling, when only every second multi-band Wannier state, with fractional winding, is occupied.

Our results show the emergence of quantization in bosonic topological systems through

interactions. They demonstrate that the Chern number remains a meaningful topological invariant also in the presence of nonlinearities. Additionally, our findings underscore the significance and impact of the fractional winding of multi-band Wannier states in interacting systems. Future research directions include investigating the effect of disorder on the quantization of Thouless pumping. While soliton transport may not be quantized after each period, we anticipate that quantization will be restored in the average displacement over many periods, as long as the disorder does not cause nonlinear bifurcations that split the contiguous trajectory of the soliton. Furthermore, it would be interesting to explore the effects of nonlinearities in the synthetic pumping dimension.

Finally, we presented advances in the fabrication of deep-etched photonic crystals in crystalline YAG. Despite the well-understood theory of photonic crystals, only few fabrication techniques are available and novel fabrication approaches are highly sought after, especially for technologically relevant crystals like YAG. Our results demonstrate the feasibility of deep-etched structures of large arrays, sub-micrometer lattice constants, and millimeter-deep, varying etching depth. These advancements pave the way for volumetrically enhanced scintillation or lasing in doped YAG. Moving forward, immediate research efforts should focus on investigating and improving the quality of the etched structures. In the long term, the fabrication of three-dimensional photonic crystals is conceivable, and exploring the interaction between two dimensional crystals and free electron radiation, notably Cerenkov radiation, holds promise for further studies.

Appendix A
Additional Properties of Bloch and Wannier basis

A.1 Definition and Normalization of the Bloch basis

In this section, we define the Bloch basis and show its normalization properties. We restrict ourselves to spatially one-dimensional systems. According to Bloch's theorem, the eigenstates in a translationally invariant system with lattice vector R are given by Bloch wavefunctions, which we define as $B_{\alpha,k}(r) = \frac{1}{\sqrt{N}} e^{ikr} u_{\alpha,k}(r)$ with a cell-periodic part $u_{\alpha,k}(r+R) = u_{\alpha,k}(r)$. Here, k denotes the wavevector, α the band index, r the position, and N the number of unit cells. We use the definition that $u_{\alpha,k}(r)$ is normalized to one over one unit cell: $\int_{UC} dr\, u_{\alpha,k}(r)^* u_{\beta,k}(r) = \delta_{\alpha,\beta}$.

Using this definition, the normalization of the Bloch wavefunction is

$$\begin{aligned}
\langle B_{\alpha,k} | B_{\beta,q} \rangle &= \frac{1}{N} \int_V dr e^{-ikr} u^*_{\alpha,k}(r) e^{iqr} u_{\beta,q}(r) \\
&= \frac{1}{N} \sum_R \int_{UC} dr e^{-i(k-q)(r-R)} u^*_{\alpha,k}(r-R) u_{\beta,q}(r-R) \\
&= \frac{1}{N} \sum_R e^{i(k-q)R} \int_{UC} dr e^{-i(k-q)r} u^*_{\alpha,k}(r) u_{\beta,q}(r) \\
&= \delta_{k,q} \int_{UC} dr u^*_{\alpha,k}(r) u_{\beta,q}(r) \\
&= \delta_{k,q} \delta_{\alpha,\beta},
\end{aligned} \tag{A.1}$$

where V denotes the volume of the system.

A.2 Further information of Wannier states

Here, we show the orthonormality of Wannier states using the discrete formulation, based on the definition in 2.20:

$$\begin{aligned}\langle w_{R,\alpha}|w_{S,\beta}\rangle &= \frac{1}{N}\sum_{k,q} e^{ikR}e^{-iqS}\langle B_{\alpha,k}|B_{\beta,q}\rangle \\ &= \frac{1}{N}\sum_{k,q} e^{ikR}e^{-iqS}\delta_{k,q}\delta_{\alpha,\beta} \\ &= \frac{1}{N}\sum_{k} e^{ik(R-S)}\delta_{\alpha,\beta} \\ &= \delta_{R,S}\delta_{\alpha,\beta}, \end{aligned} \tag{A.2}$$

where we have used the results from Eq. A.1 for the second line.

Furthermore, we show that Wannier states are translational copies of each other:

$$\begin{aligned} w_{R,\alpha}(r) &= \frac{1}{\sqrt{N}}\sum_{k} e^{-ikR}B_{\alpha,k}(r) \\ &= \frac{1}{N}\sum_{k} e^{ik(r-R)}u_{\alpha,k}(r) \\ &= \frac{1}{N}\sum_{k} e^{ik(r-R)}u_{\alpha,k}(r-R) \\ &= \frac{1}{\sqrt{N}}\sum_{k} B_{\alpha,k}(r-R) \\ &= w_{0,\alpha}(r-R). \end{aligned} \tag{A.3}$$

Third, we show that the Wannier functions span the same subspace as the Bloch functions:

$$\begin{aligned}\sum_{R}|w_{\alpha,R}\rangle\langle w_{\alpha,R}| &= \sum_{R}\sum_{k,k'}|B_{\alpha,k}\rangle\langle B_{\alpha,k}|w_{\alpha,R}\rangle\langle w_{\alpha,R}|B_{\alpha,k'}\rangle\langle B_{\alpha,k'}| \\ &= \frac{1}{N}\sum_{R}\sum_{k,k'}|B_{\alpha,k}\rangle\langle B_{\alpha,k'}|\, e^{-i(k-k')R} \\ &= \sum_{k}|B_{\alpha,k}\rangle\langle B_{\alpha,k}|. \end{aligned} \tag{A.4}$$

Appendix B
Further information on solitons

In this appendix, we give further information on the bifurcation of solitons, how to numerically find solitons, and how to determine their stability.

B.1 Soliton bifurcations

In this section, we will show the bifurcation of solitons from their respective bands at low power. Fig. B.1a shows the nonlinear eigenvalue as a function of strength of nonlinearity. At low nonlinearity, the soliton eigenvalue is close to the bottom of a band and can therefore be uniquely identified with a single band. With increasing power, the soliton becomes more localized (see Fig. B.1b), and the eigenvalue diverges from the band into the respective lower bandgap. The projection of the soliton that bifurcates from the lowest band is shown in Fig. B.1c, and confirms the identification of the soliton with a single band for lower power. At extremely low power, a discrete soliton is well described by the energetically lowest Bloch state of a given band multiplied with a wide hyperbolic secant envelope function.

B.2 Numerical methods to find solitons

In this dissertation we use two methods to find solitons: (1) A self-consistent method and (2) a Newton iteration scheme. We found that the self-consistent method is computationally faster, but often converges only to few dominant solitons, while Newton iteration is computationally slower but allows to find more solitons.

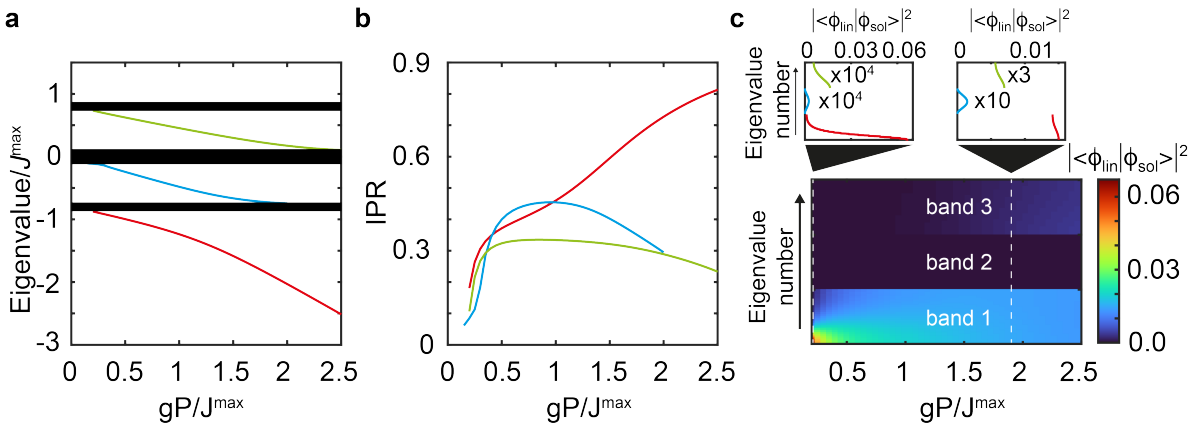

Figure B.1. Analysis of soliton bifurcation. **a**, Energy eigenvalues for the linear eigenstates at z=0 (black) (from Chapter 3) showing three bands. Nonlinear eigenvalues for solitons bifurcating from the upper (middle, lower) band are shown in green (blue, red) and are decreasing with increasing power. **b**, Degree of soliton localization as measured by the Inverse Participation Ratio IPR $= \sum_n |\phi_n|^4/(\sum_n |\phi_n|^2)^2$ for the solitons shown in **a**. **c**, Spectral overlap coefficients between the soliton bifurcating from the lowest band and the linear energy eigenstates are a strong function of power. The two upper panels show the occupation at $gP/J^{\max} = 0.2$ and 1.9. Note the non-uniform occupation of the lowest band (from which the soliton bifurcates), which is particularly pronounced at low power.

B.2.1 Self-consistency algorithm

The self-consistency algorithm described in the following is a simple and computationally extremely efficient way to find solitons. Convergence depends critically on the starting guess. We have made the experience, that the algorithm tends to converge to stable solitons and often to solitons that are strongly localized. Typical initial guesses with a high success rate are single-site excitations and the maximally-localized Wannier state of the band from which the soliton is intended to bifurcate.

The self-consistent algorithm converges exponentially using the following iterative steps:

1. Choose an initial guess, $\psi^{(i)}$, for the wave function.
2. Calculate the full Hamiltonian, which includes the linear Hamiltonian and the nonlinearly-induced potential: $H = H_{\text{lin}} - g|\psi|^2$
3. Calculate the eigenvectors of H and choose the eigenvector with the largest overlap with $\psi^{(i)}$ as the initial guess for the next iteration.
4. Iterate steps 2 and 3 until the desired convergence is achieved.

B.2.2 Newton-Iteration

We use Newton's method to find low-power and inter-site solitons. To be specific, we solve the set of N (with N being the number of sites) equations describing the stationary discrete nonlinear Schrödinger equation for a given degree of nonlinearity g, while simultaneously constraining the power of the wave function.

$$0 = \sum_m H_{n,m}\phi_m - g|\phi_n|^2\phi_n - \lambda\phi_n \qquad \forall n \in \{1, 2..., N\} \tag{B.1}$$

$$0 = \sum_n |\phi_n|^2 - P \tag{B.2}$$

Here, H_{nm} is the tight-binding real space Hamiltonian and the algorithm solves for the amplitudes of the wave function, ϕ_n, and the nonlinear eigenvalue λ. A similar set of equations (that follows straightforwardly from Eq. (4.12) is used when solving for the soliton in simplified Wannier space. We use Mathematica's FindRoot [106] to solve the set of $N+1$ equations. Especially for low power, successful convergence critically depends on the initial guess.

The solitons shown in Fig. 4.3 and 4.4 of chapter 4, are first solved for in Wannier space using the following starting guess derived from the continuum approximation:

$$c^{(0)}_{R,\alpha,n} = -\text{sign}[\epsilon_{R_1,\alpha}]^n \sqrt{\frac{2\tilde{E}|\epsilon_{R_1,\alpha}|}{gW}} \text{sech}(\sqrt{\tilde{E}}(n - n_0)) \tag{B.3}$$

where $\epsilon_{R_1,\alpha}$ is the first Fourier coefficient of the band structure for band α, describing the nearest-neighbor hoppings, n_0 is the center of the soliton, which can be chosen on-site or inter-site, $W \equiv W^{\alpha,\alpha,\alpha,\alpha}_{R,R,R,R}$ is the overlap integral as defined in Eq. (4.8), and $\tilde{E} = \left(\frac{PgW}{4|\epsilon_{R_1,\alpha}|^2}\right)^2$ is the energy difference between the (linear) band minimum and the energy of a continuum approximated soliton. The solitons found in Wannier space (shown in black in Fig. 4.3 and Fig. 4.4) are then transformed into real space and subsequently used as seeds to calculate the solitons in real space (shown in red in Fig. 4.3 and Fig. 4.4). When calculating solitons for a full pumping cycle, we use the soliton of each time step as the starting guess for the next time step.

B.3 Linear stability analysis

Assuming a static (for example, z-independent) Hamiltonian, a system prepared in an unstable nonlinear eigenstate does not guarantee a static evolution of the system, because

small fluctuations (even those caused by the limits of numerical precision) can amplify, and thus the soliton has a finite lifetime. We test the stability of solitons using linear stability analysis, which indicates when solitons are linearly unstable. We follow Ref. [88] and start with a nonlinear eigenstate $\phi^{(0)}(z) = e^{-i\Lambda z}\phi^{(0)}$ for the nonlinear Schrödinger equation $i\partial_z\phi = H\phi - g|\phi|^2\phi$, where H is the linear tight-binding Hamiltonian of the system, the parameter g describes the strength of the nonlinearity, ϕ is the (discrete) wavefunction and Λ describes the eigenvalue of the eigenstate $\phi^{(0)}$. We have dropped the subscripts, but it is clear that this equation should be understood as a tight-binding matrix equation. To test for stability, we take the following ansatz for a small perturbation around the solution: $\phi = e^{i\Lambda z}[\phi^{(0)} + \epsilon(v(z) + iw(z))]$. Plugging this ansatz into the nonlinear Schrödinger equation and using the fact that $\phi(z)$ solves the equation, we arrive (after some algebra) to first order in ϵ at the following two equations for the real and the imaginary parts of the perturbation

$$\frac{d}{dz}v = \left(-\Lambda + H - 2g|\phi^{(0)}|^2 + g(\phi^{(0)})^2\right) w \equiv L_- w \tag{B.4}$$

$$\frac{d}{dz}w = -\left(-\Lambda + H - 2g|\phi^{(0)}|^2 - g(\phi^{(0)})^2\right) v \equiv -L_+ w v \tag{B.5}$$

These coupled equations are solved by separating the z-dependence via $v = e^{\kappa z}\bar{v}$ and $w = e^{\kappa z}\bar{w}$, which leads to $\kappa\bar{w} = -L_+\bar{v}$ and $\kappa\bar{v} = L_-\bar{w}$. The values of κ^2 can now be calculated as eigenvalues of the matrix $-L_-L_+$. If κ^2 is positive, then κ is real and the perturbations can build up exponentially. In contrast, if κ^2 is negative, then κ is imaginary and the perturbations are oscillating waves that do not grow exponentially. In the latter case the soliton is linearly stable. In the main text, we identify solitons as stable if $\kappa^2 < 10^{-15}$

Appendix C
Additional details on the experiments

C.1 Experimental setups

In this section, we describe the two main experimental setups used for the fabrication and characterization of evanescently coupled waveguide arrays.

C.1.1 Fabrication setup

The fabrication setup is based on a higher-power pulsed laser pulse that is focused into a borosilicate glass sample that is mounted onto a high-precision computer-controlled xyz-translation stage (Aerotech ANT 130). Figure C.1 shows a schematic of the setup. The laser (Menlo Blucut) emits ≈260 fs laser pulses with a (tunable) repetition rate of 500 kHz and central wavelength of 1030nm. We use a system of a half-wave plate (WP1) and a polarization beam splitter (PBS) to adjust the power. With a second set of half-wave (WP2) and quarter-wave plate (WP3), we enable to set all possible polarization outputs. For waveguide fabrication we typically use circular polarization. The laser beam then passes through a mechanical slit (typically set to 1.8 mm) for beam-shaping and is focused into the sample via an aspheric lens (Thorlabs A110TM-B, f=6.24 mm, NA=0.4). We use an additional flip mirror before the slit to measure the power, defined as writing power. A 90:10 beam splitter (Thorlabs BSX11) allows to image the back-reflected light from the sample onto a camera, which is used to calibrate the position of the upper sample surface.

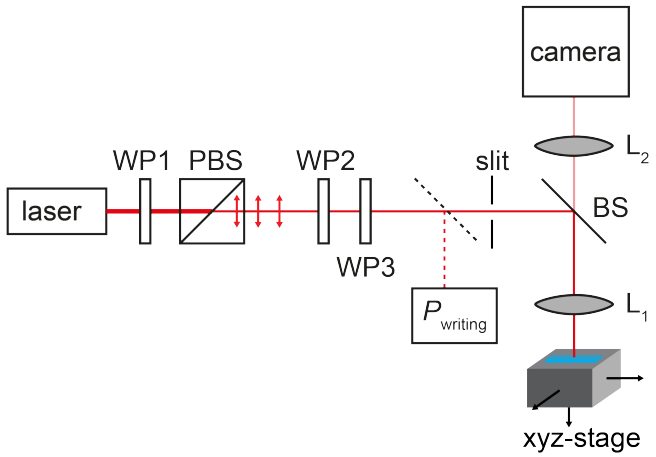

Figure C.1. Fabrication setup. The laser power is adjusted using a wave plate (WP1) and a polarization beam splitter (PBS) and turned into circular polarization using WP2 and WP3. After passing through a mechanical slit, the beam is focused using lens L_1 onto the borosilicate glass sample mounted on a computer-controlled high-precision xyz-stage. Reflected power is passed through a 90:10 beamsplitter (BS) and focused via lens L_2 onto a camera. The writing power is typically measured before the slit using a flip mirror.

C.1.2 Nonlinear experiments

We perform the nonlinear experiments with the same laser (Menlo Bluecut) as used for fabrication. A schematic of the setup is shown in Fig. C.2. As short laser pulses lead to significant self-phase modulation, we stretch the pulses using two gratings G_1 and G_2 (Thorlabs GR25-0610). The beam is focused into the waveguide array using lens L_1 (Thorlabs LB1761-B-ML) and imaged onto a camera using lens L_2 (Thorlabs AC127-030-B-ML or LB1811-B-ML). The incoupling power P_{in} is measured before L_1 and the outcoupled power P_{out} is measured after L_2. A beam splitter (BS) is used to send some part of the out-coupled light into a fiber-coupled optical spectrum analyzer (OSA).

C.2 Spectral measurements

Self-phase modulation leads to the generation of new wavelengths for high power laser pulses. As the hopping between waveguides is a function of the wavelength, maintaining a narrow spectrum is important. We measure the spectrum of the laser after passing through a single waveguide as a function of input power (see Fig. C.3). For increasing input power, the width of the spectrum broadens from initially 7 nm to 20 nm (calculated

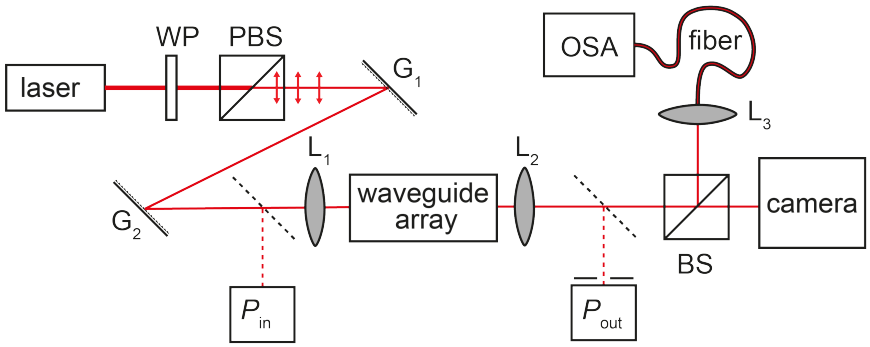

Figure C.2. Experimental setup for nonlinear waveguide characterization. After adjusting the laser power using a half-wave plate (WP) and a polarization beam splitter (PBS), the laser pulses are temporally stretched to about 2 ps using gratings G_1 and G_2. Lenses L_1 and L_2 couple the beam into the waveguide array and image it onto a camera, respectively. Using flip mirrors, we measure the in-coupled power P_{in} and the out-coupled power P_{out}. A beam splitter (BS) allows the simultaneous analysis of the out-coupled light via a fiber coupled optical spectrum analyzer (OSA).

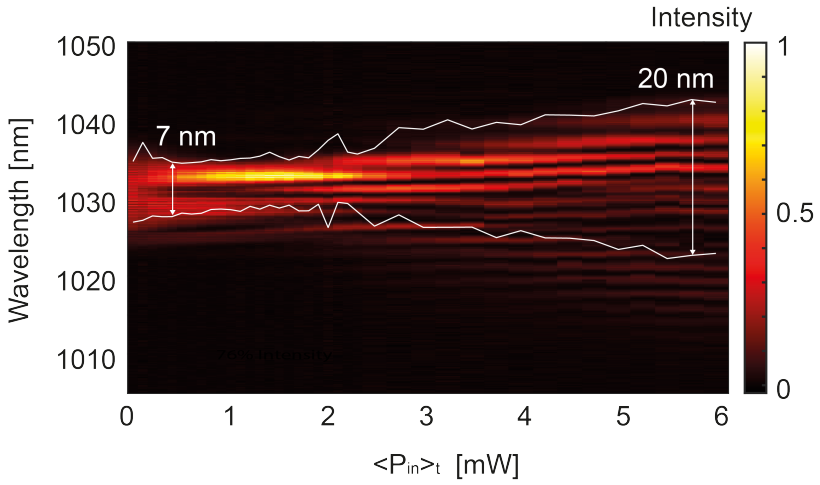

Figure C.3. Nonlinear output spectrum. Optical spectrum for temporally stretched pulses (about 2 ps) after propagation through a 7.6 cm-long waveguide. Due to self-phase modulation the spectrum broadens from initially 7 nm to around 20 nm for the highest input power used in the experiments.

as the spectral width that contains 76% of the intensity). Within this range the change of the hopping is on the order of the uncertainty of the on-site potential due to fabrication. We can therefore neglect its effects and simulate the propagation using a mono-chromatic nonlinear Schrödinger equation.

Appendix D
Deep-etching recipe

In this appendix, we describe the fabrication process of deep-etched structures, consisting of three parts:

Part 1: Direct femto-second laser writing.

We write the structures in longitudinal writing configuration. Furthermore, we note the following:

- No slit is used (equivalently, the slit is fully open) to allow for the smallest focus.
- Good results have been obtained with an NA=0.68 objective, that is a good trade-off between high numerical aperture, large working distance and manageable spherical aberrations.
- We start writing at the bottom of the sample and write towards the top by moving the sample downwards. We switch off the laser (using the internal acousto-optic modulator) before the laser reaches the top surface to avoid laser ablation (the formation of craters) at the top surface.
- Typical fabrication parameters are: laser repetition rate: 500 kHz; temporal pulse width: ≈ 270 fs; time-averaged power: 90 mW (175 mW) at the top (bottom) surface; writing speed: 1 mm/s.

Optional: For a good side-view, the side facet should be polished either before or after the writing step.

Part 2: Grinding & Polishing

In this step, both surfaces are mechanically grinded and polished to expose the waveguides. A typical grinding/polishing process is first applied to the bottom surface and finally to the top surface. We use a precision polisher (Allied Hightech Multiprep) with the following steps:

- We glue the sample to the holder and measure the sample height. We are careful to use only small amounts of glue that is evenly spread to avoid breaking the sample when pressure is applied during the grinding process.
- Optional: To thin the sample by hundreds of microns, we use the 30 μm diamond sanding paper and 100 rpm to grind down the crystal.
- We use the 10 μm diamond sanding paper and 100 rpm to sand down about 30-50μm.
- We use the 3 μm diamond polishing paper and 100 rpm to polish down about 10μm.

During the changes of the sanding/polishing paper, the remaining height of the sample can be measured to compare the nominal change in height to the actual change.

Part 3: Chemical wet-etching

- We clean the sample using Acetone in an ultrasonic bath (5 mins), Isopropanol in an ultrasonic bath (5 mins), and finally rinse the sample with deionised (DI) water.
- We wet-etch the resulting structures in 44 wt% Phosphoric acid. As the cleanroom at Penn State only stocks 85% Phosphoric acid, we measure 178 g of DI water and add 200 g of Phosphoric Acid 85%. We heat the solution to 78 degree Celsius while using a magnetic stirrer on a heat plate covered with an hourglass.
- We repeat the cleaning procedure after etching.

Bibliography

[1] Mukherjee, S. *Experimental Simulation of Solid-State Phenomena Using Photonic Lattices*. Ph.D. thesis, Heriot-Watt University (2016).

[2] Jürgensen, M., Mukherjee, S., Jörg, C. & Rechtsman, M. C. Quantized fractional Thouless pumping of solitons. *Nature Physics* **19**, 420–426 (2023).

[3] v Klitzing, K., Dorda, G. & Pepper, M. New Method for High-Accuracy Determination of the Fine-Structure Constant Based on Quantized Hall Resistance. *Physical Review Letters* **45**, 494–497 (1980).

[4] von Klitzing, K. Metrology in 2019. *Nature Physics* **13**, 198–198 (2017).

[5] Laughlin, R. B. Quantized Hall conductivity in two dimensions. *Physical Review B* **23**, 5632 (1981).

[6] Thouless, D. J., Kohmoto, M., Nightingale, M. P. & den Nijs, M. Quantized Hall conductance in a two-dimensional periodic potential. *Physical Review Letters* **49**, 405 (1982).

[7] Haldane, F. D. M. Model for a Quantum Hall Effect without Landau Levels: Condensed-Matter Realization of the "Parity Anomaly". *Physical Review Letters* **61**, 2015–2018 (1988).

[8] Raghu, S. & Haldane, F. D. M. Analogs of quantum-Hall-effect edge states in photonic crystals. *Physical Review A* **78**, 033834 (2008).

[9] Haldane, F. D. M. & Raghu, S. Possible Realization of Directional Optical Waveguides in Photonic Crystals with Broken Time-Reversal Symmetry. *Physical Review Letters* **100**, 013904 (2008).

[10] Wang, Z., Chong, Y., Joannopoulos, J. D. & Soljačić, M. Observation of unidirectional backscattering-immune topological electromagnetic states. *Nature* **461**, 772–775 (2009).

[11] He, C. *et al.* Acoustic topological insulator and robust one-way sound transport. *Nature Physics* **12**, 1124–1129 (2016).

[12] Rechtsman, M. C. *et al.* Photonic Floquet topological insulators. *Nature* **496**, 196 (2013).

[13] Hafezi, M., Mittal, S., Fan, J., Migdall, A. & Taylor, J. M. Imaging topological edge states in silicon photonics. *Nature Photonics* **7**, 1001 (2013).

[14] Schine, N., Ryou, A., Gromov, A., Sommer, A. & Simon, J. Synthetic Landau levels for photons. *Nature* **534**, 671–675 (2016).

[15] Jotzu, G. *et al.* Experimental realization of the topological Haldane model with ultracold fermions. *Nature* **515**, 237–240 (2014).

[16] Aidelsburger, M. *et al.* Measuring the Chern number of Hofstadter bands with ultracold bosonic atoms. *Nature Physics* **11**, 162–166 (2015).

[17] Süsstrunk, R. & Huber, S. D. Observation of phononic helical edge states in a mechanical topological insulator. *Science* **349**, 47–50 (2015).

[18] Klembt, S. *et al.* Exciton-polariton topological insulator. *Nature* **562**, 552–556 (2018).

[19] Ningyuan, J., Owens, C., Sommer, A., Schuster, D. & Simon, J. Time- and Site-Resolved Dynamics in a Topological Circuit. *Physical Review X* **5**, 021031 (2015).

[20] Ozawa, T. *et al.* Topological photonics. *Reviews of Modern Physics* **91**, 015006 (2019).

[21] Goldman, N., Juzeliūnas, G., Öhberg, P. & Spielman, I. B. Light-induced gauge fields for ultracold atoms. *Reports on Progress in Physics* **77**, 126401 (2014).

[22] Abo-Shaeer, J. R., Raman, C., Vogels, J. M. & Ketterle, W. Observation of Vortex Lattices in Bose-Einstein Condensates. *Science* **292**, 476–479 (2001).

[23] Fletcher, R. J. *et al.* Geometric squeezing into the lowest Landau level. *Science* **372**, 1318–1322 (2021).

[24] Rechtsman, M. C. *et al.* Strain-induced pseudomagnetic field and photonic Landau levels in dielectric structures. *Nature Photonics* **7**, 153 (2012).

[25] Guglielmon, J., Rechtsman, M. C. & Weinstein, M. I. Landau levels in strained two-dimensional photonic crystals. *Physical Review A* **103**, 013505 (2021).

[26] Barczyk, R., Kuipers, L. & Verhagen, E. Observation of Landau levels and topological edge states in photonic crystals through pseudomagnetic fields induced by synthetic strain. *arxiv preprint arXiv:2306.03860* (2023). 2306.03860.

[27] Barsukova, M. *et al.* Direct Observation of Landau Levels in Silicon Photonic Crystals. *arxiv preprint arXiv:2306.04011* (2023). 2306.04011.

[28] Jin, J. *et al.* Observation of Floquet Chern insulators of light. *arxiv preprint arXiv:2304.09385* (2023). 2304.09385.

[29] Thouless, D. J. Quantization of particle transport. *Physical Review B* **27**, 6083–6087 (1983).

[30] Niu, Q. & Thouless, D. J. Quantised adiabatic charge transport in the presence of substrate disorder and many-body interaction. *Journal of Physics A: Mathematical and General* **17**, 2453 (1984).

[31] Niu, Q., Thouless, D. J. & Wu, Y.-S. Quantized Hall conductance as a topological invariant. *Physical Review B* **31**, 3372–3377 (1985).

[32] Tsui, D. C., Stormer, H. L. & Gossard, A. C. Two-Dimensional Magnetotransport in the Extreme Quantum Limit. *Physical Review Letters* **48**, 1559–1562 (1982).

[33] Freedman, M., Kitaev, A., Larsen, M. & Wang, Z. Topological quantum computation. *Bulletin of the American Mathematical Society* **40**, 31–38 (2003).

[34] Mittal, S., Goldschmidt, E. A. & Hafezi, M. A topological source of quantum light. *Nature* **561**, 502–506 (2018).

[35] Maczewsky, L. J. *et al.* Nonlinearity-induced photonic topological insulator. *Science* **370**, 701–704 (2020).

[36] Mukherjee, S. & Rechtsman, M. C. Observation of Floquet solitons in a topological bandgap. *Science* **368**, 856–859 (2020).

[37] Mukherjee, S. & Rechtsman, M. C. Period-doubled Floquet solitons. *Optica* **10**, 1310 (2023).

[38] Mukherjee, S. & Rechtsman, M. C. Observation of Unidirectional Solitonlike Edge States in Nonlinear Floquet Topological Insulators. *Physical Review X* **11**, 041057 (2021).

[39] Bandres, M. A. *et al.* Topological insulator laser: Experiments. *Science* **359** (2018).

[40] Mittal, S., Moille, G., Srinivasan, K., Chembo, Y. K. & Hafezi, M. Topological frequency combs and nested temporal solitons. *Nature Physics* **17**, 1169–1176 (2021).

[41] Citro, R. & Aidelsburger, M. Thouless pumping and topology. *Nature Reviews Physics* **5**, 87–101 (2023).

[42] Ke, Y. *et al.* Topological pumping assisted by Bloch oscillations. *Physical Review Research* **2**, 033143 (2020).

[43] Leykam, D. & Smirnova, D. A. Probing bulk topological invariants using leaky photonic lattices. *Nature Physics* **17**, 632–638 (2021).

[44] Kraus, Y. E., Lahini, Y., Ringel, Z., Verbin, M. & Zilberberg, O. Topological States and Adiabatic Pumping in Quasicrystals. *Physical Review Letters* **109**, 106402 (2012).

[45] Lohse, M., Schweizer, C., Zilberberg, O., Aidelsburger, M. & Bloch, I. A Thouless quantum pump with ultracold bosonic atoms in an optical superlattice. *Nature Physics* **12**, 350–354 (2016).

[46] Nakajima, S. *et al.* Topological Thouless pumping of ultracold fermions. *Nature Physics* **12**, 296–300 (2016).

[47] Fedorova, Z., Qiu, H., Linden, S. & Kroha, J. Observation of topological transport quantization by dissipation in fast Thouless pumps. *Nature Communications* **11**, 3758 (2020).

[48] Lohse, M., Schweizer, C., Price, H. M., Zilberberg, O. & Bloch, I. Exploring 4D quantum Hall physics with a 2D topological charge pump. *Nature* **553**, 55–58 (2018).

[49] Zilberberg, O. *et al.* Photonic topological boundary pumping as a probe of 4D quantum Hall physics. *Nature* **553**, 59–62 (2018).

[50] Kudo, K., Watanabe, H., Kariyado, T. & Hatsugai, Y. Many-Body Chern Number without Integration. *Physical Review Letters* **122**, 146601 (2019).

[51] Cerjan, A., Wang, M., Huang, S., Chen, K. P. & Rechtsman, M. C. Thouless pumping in disordered photonic systems. *Light: Science & Applications* **9**, 178 (2020).

[52] Tangpanitanon, J. *et al.* Topological Pumping of Photons in Nonlinear Resonator Arrays. *Physical Review Letters* **117**, 213603 (2016).

[53] Ke, Y., Qin, X., Kivshar, Y. S. & Lee, C. Multiparticle Wannier states and Thouless pumping of interacting bosons. *Physical Review A* **95**, 063630 (2017).

[54] Hayward, A., Schweizer, C., Lohse, M., Aidelsburger, M. & Heidrich-Meisner, F. Topological charge pumping in the interacting bosonic Rice-Mele model. *Physical Review B* **98**, 245148 (2018).

[55] Nakajima, S. *et al.* Competition and interplay between topology and quasi-periodic disorder in Thouless pumping of ultracold atoms. *Nature Physics* **17**, 844–849 (2021).

[56] Walter, A.-S. *et al.* Quantization and its breakdown in a Hubbard–Thouless pump. *Nature Physics* 1–5 (2023).

[57] Xiao, D., Chang, M.-C. & Niu, Q. Berry phase effects on electronic properties. *Reviews of Modern Physics* **82**, 1959–2007 (2010).

[58] Asbóth, J. K., Oroszlány, L. & Pályi, A. *A Short Course on Topological Insulators*, vol. 919 (Springer, 2016).

[59] Born, M. & Fock, V. Beweis des Adiabatensatzes. *Zeitschrift für Physik* **51**, 165–180 (1928).

[60] Berry, M. V. Quantal phase factors accompanying adiabatic changes. *Proceedings of the Royal Society of London. A. Mathematical and Physical Sciences* **392**, 45–57 (1984).

[61] Cohen, E. *et al.* Geometric phase from Aharonov–Bohm to Pancharatnam–Berry and beyond. *Nature Reviews Physics* **1**, 437–449 (2019).

[62] Harper, P. G. Single band motion of conduction electrons in a uniform magnetic field. *Proceedings of the Physical Society. Section A* **68**, 874 (1955).

[63] Aubry, S. & André, G. Analyticity breaking and Anderson localization in incommensurate lattices. *Ann. Israel Phys. Soc* **3**, 18 (1980).

[64] Ke, Y. *et al.* Topological phase transitions and Thouless pumping of light in photonic waveguide arrays. *Laser & Photonics Reviews* **10**, 995–1001 (2016).

[65] Vanderbilt, D. *Berry Phases in Electronic Structure Theory: Electric Polarization, Orbital Magnetization and Topological Insulators* (Cambridge University Press, 2018).

[66] Wannier, G. H. The Structure of Electronic Excitation Levels in Insulating Crystals. *Physical Review* **52**, 191–197 (1937).

[67] Kohn, W. Analytic Properties of Bloch Waves and Wannier Functions. *Physical Review* **115**, 809–821 (1959).

[68] Cloizeaux, J. D. Analytical Properties of n -Dimensional Energy Bands and Wannier Functions. *Physical Review* **135**, A698–A707 (1964).

[69] Marzari, N., Mostofi, A. A., Yates, J. R., Souza, I. & Vanderbilt, D. Maximally localized Wannier functions: Theory and applications. *Reviews of Modern Physics* **84**, 1419–1475 (2012).

[70] Marzari, N. & Vanderbilt, D. Maximally localized generalized Wannier functions for composite energy bands. *Physical Review B* **56**, 12847–12865 (1997).

[71] Kivelson, S. Wannier functions in one-dimensional disordered systems: Application to fractionally charged solitons. *Physical Review B* **26**, 4269–4277 (1982).

[72] Resta, R. Quantum-Mechanical Position Operator in Extended Systems. *Physical Review Letters* **80**, 1800–1803 (1998).

[73] Zak, J. Berry's phase for energy bands in solids. *Physical Review Letters* **62**, 2747–2750 (1989).

[74] King-Smith, R. D. & Vanderbilt, D. Theory of polarization of crystalline solids. *Physical Review B* **47**, 1651–1654 (1993).

[75] Resta, R. Macroscopic polarization in crystalline dielectrics: The geometric phase approach. *Reviews of Modern Physics* **66**, 899–915 (1994).

[76] Davis, K. M., Miura, K., Sugimoto, N. & Hirao, K. Writing waveguides in glass with a femtosecond laser. *Optics Letters* **21**, 1729–1731 (1996).

[77] Miura, K., Qiu, J., Inouye, H., Mitsuyu, T. & Hirao, K. Photowritten optical waveguides in various glasses with ultrashort pulse laser. *Applied Physics Letters* **71**, 3329–3331 (1997).

[78] Szameit, A. & Nolte, S. Discrete optics in femtosecond-laser-written photonic structures. *Journal of Physics B: Atomic, Molecular and Optical Physics* **43**, 163001 (2010).

[79] Pertsch, T. *et al.* Discrete diffraction in two-dimensional arrays of coupled waveguides in silica. *Optics Letters* **29**, 468 (2004).

[80] Itoh, K., Watanabe, W., Nolte, S. & Schaffer, C. B. Ultrafast Processes for Bulk Modification of Transparent Materials. *MRS Bulletin* **31**, 620–625 (2006).

[81] Jia, Y., Wang, S. & Chen, F. Femtosecond laser direct writing of flexibly configured waveguide geometries in optical crystals: Fabrication and application. *Opto-Electronic Advances* **3**, 190042–190042 (2020).

[82] Osellame, R. *et al.* Lasing in femtosecond laser written optical waveguides. *Applied Physics A* **93**, 17–26 (2008).

[83] Ams, M., Marshall, G. D., Spence, D. J. & Withford, M. J. Slit beam shaping method for femtosecond laser direct-write fabrication of symmetric waveguides in bulk glasses. *Optics Express* **13**, 5676–5681 (2005).

[84] Kawano, K. & Kitoh, T. *Introduction to Optical Waveguide Analysis: Solving Maxwell's Equation and the Schrödinger Equation* (John wiley & sons, 2004).

[85] Joannopoulos, J. D., Johnson, S. G., Winn, J. N. & Meade, R. D. *Photonic Crystals. Molding the Flow of Light.* (Princeton University Press, 2008), 2nd edn.

[86] Bloembergen, N. *Nonlinear Optics* (World Scientific, 1996).

[87] Boyd, R. W. *Nonlinear Optics* (Academic Press, Inc., USA, 2008), 3rd edn.

[88] Kevrekidis, P. G. *The Discrete Nonlinear Schrödinger Equation: Mathematical Analysis, Numerical Computations and Physical Perspectives*, vol. 232 (Springer Science & Business Media, 2009).

[89] Pitaevskii, L. & Stringari, S. *Bose-Einstein Condensation and Superfluidity*, vol. 164 (Oxford University Press, 2016).

[90] Christodoulides, D. N., Lederer, F. & Silberberg, Y. Discretizing light behaviour in linear and nonlinear waveguide lattices. *Nature* **424**, 817–823 (2003).

[91] Lederer, F. *et al.* Discrete solitons in optics. *Physics Reports* **463**, 1–126 (2008).

[92] Christodoulides, D. N. & Joseph, R. I. Discrete self-focusing in nonlinear arrays of coupled waveguides. *Optics Letters* **13**, 794–796 (1988).

[93] Eisenberg, H. S., Silberberg, Y., Morandotti, R., Boyd, A. R. & Aitchison, J. S. Discrete spatial optical solitons in waveguide arrays. *Physical Review Letters* **81**, 3383 (1998).

[94] Fleischer, J. W., Segev, M., Efremidis, N. K. & Christodoulides, D. N. Observation of two-dimensional discrete solitons in optically induced nonlinear photonic lattices. *Nature* **422**, 147–150 (2003).

[95] Kivshar, Y. S. & Campbell, D. K. Peierls-Nabarro potential barrier for highly localized nonlinear modes. *Physical Review E* **48**, 3077–3081 (1993).

[96] Aceves, A. B. *et al.* Discrete self-trapping, soliton interactions, and beam steering in nonlinear waveguide arrays. *Physical Review E* **53**, 1172–1189 (1996).

[97] Morandotti, R., Peschel, U., Aitchison, J. S., Eisenberg, H. S. & Silberberg, Y. Dynamics of Discrete Solitons in Optical Waveguide Arrays. *Physical Review Letters* **83** (1999).

[98] Yariv, A. Coupled-mode theory for guided-wave optics. *IEEE Journal of Quantum Electronics* **9**, 919–933 (1973).

[99] Jürgensen, M., Mukherjee, S. & Rechtsman, M. C. Quantized nonlinear Thouless pumping. *Nature* **596**, 63–67 (2021).

[100] Ryu, S., Schnyder, A. P., Furusaki, A. & Ludwig, A. W. W. Topological insulators and superconductors: Tenfold way and dimensional hierarchy. *New Journal of Physics* **12**, 065010 (2010).

[101] Benalcazar, W. A., Bernevig, B. A. & Hughes, T. L. Quantized electric multipole insulators. *Science* **357**, 61–66 (2017).

[102] Schindler, F. *et al.* Higher-order topological insulators. *Science Advances* **4**, eaat0346 (2018).

[103] Rosiek, C. A. *et al.* Observation of strong backscattering in valley-Hall photonic topological interface modes. *Nature Photonics* **17**, 386–392 (2023).

[104] Pu, H., Maenner, P., Zhang, W. & Ling, H. Y. Adiabatic Condition for Nonlinear Systems. *Physical Review Letters* **98**, 050406 (2007).

[105] Liu, J., Wu, B. & Niu, Q. Nonlinear Evolution of Quantum States in the Adiabatic Regime. *Physical Review Letters* **90**, 170404 (2003).

[106] Wolfram Research, I. Mathematica, Version 12.0 (2019).

[107] Wiggins, S. *Introduction to Applied Nonlinear Dynamical Systems and Chaos*, vol. 2 (Springer Science & Business Media, 2003).

[108] Fukui, T., Hatsugai, Y. & Suzuki, H. Chern Numbers in Discretized Brillouin Zone: Efficient Method of Computing (Spin) Hall Conductances. *Journal of the Physical Society of Japan* **74**, 1674–1677 (2005).

[109] Jürgensen, M. & Rechtsman, M. C. Chern Number Governs Soliton Motion in Nonlinear Thouless Pumps. *Physical Review Letters* **128**, 113901 (2022).

[110] Kivshar, Y. S. & Agrawal, G. P. *Optical Solitons: From Fibers to Photonic Crystals* (Academic press, 2003).

[111] Dalfovo, F., Giorgini, S., Pitaevskii, L. P. & Stringari, S. Theory of Bose-Einstein condensation in trapped gases. *Reviews of Modern Physics* **71**, 463–512 (1999).

[112] Deng, H., Weihs, G., Santori, C., Bloch, J. & Yamamoto, Y. Condensation of Semiconductor Microcavity Exciton Polaritons. *Science* **298**, 199–202 (2002).

[113] Kasprzak, J. *et al.* Bose–Einstein condensation of exciton polaritons. *Nature* **443**, 409–414 (2006).

[114] Balili, R., Hartwell, V., Snoke, D., Pfeiffer, L. & West, K. Bose-Einstein Condensation of Microcavity Polaritons in a Trap. *Science* **316**, 1007–1010 (2007).

[115] Alfimov, G. L., Kevrekidis, P. G., Konotop, V. V. & Salerno, M. Wannier functions analysis of the nonlinear Schrödinger equation with a periodic potential. *Physical Review E* **66**, 046608 (2002).

[116] Rice, M. J. & Mele, E. J. Elementary excitations of a linearly conjugated diatomic polymer. *Physical Review Letters* **49**, 1455 (1982).

[117] Mostaan, N., Grusdt, F. & Goldman, N. Quantized topological pumping of solitons in nonlinear photonics and ultracold atomic mixtures. *Nature Communications* **13**, 5997 (2022).

[118] Simon, B. Holonomy, the Quantum Adiabatic Theorem, and Berry's Phase. *Physical Review Letters* **51**, 2167–2170 (1983).

[119] Laughlin, R. B. Anomalous Quantum Hall Effect: An Incompressible Quantum Fluid with Fractionally Charged Excitations. *Physical Review Letters* **50**, 1395–1398 (1983).

[120] Jain, J. K. Composite-fermion approach for the fractional quantum Hall effect. *Physical Review Letters* **63**, 199–202 (1989).

[121] Jain, J. K. *Composite Fermions* (Cambridge University Press, 2007).

[122] Clark, L. W., Schine, N., Baum, C., Jia, N. & Simon, J. Observation of Laughlin states made of light. *Nature* **582**, 41–45 (2020).

[123] Léonard, J. *et al.* Realization of a fractional quantum Hall state with ultracold atoms. *Nature* **619**, 495–499 (2023).

[124] Pernet, N. *et al.* Gap solitons in a one-dimensional driven-dissipative topological lattice. *Nature Physics* **18**, 678–684 (2022).

[125] Xia, S. *et al.* Nonlinear tuning of PT symmetry and non-Hermitian topological states. *Science* **372**, 72–76 (2021).

[126] Donley, E. A. *et al.* Dynamics of collapsing and exploding Bose–Einstein condensates. *Nature* **412**, 295–299 (2001).

[127] Askaryan, G. A. Effect of the gradient of a strong electromagnetic ray on electrons and atoms. *Zhur. Eksptl'. i Teoret. Fiz.* **42**, 1567–1570 (1962).

[128] Chiao, R. Y., Garmire, E. & Townes, C. H. Self-Trapping of Optical Beams. *Physical Review Letters* **13**, 479–482 (1964).

[129] Ablowitz, M. J. & Segur, H. *Solitons and the Inverse Scattering Transform* (SIAM, 1981).

[130] Stegeman, G. I. & Segev, M. Optical Spatial Solitons and Their Interactions: Universality and Diversity. *Science* **286**, 1518–1523 (1999).

[131] Luo, W.-W., He, A.-L., Wang, Y.-F., Zhou, Y. & Gong, C.-D. Bosonic fractional Chern insulating state at integer fillings in a multiband system. *Physical Review B* **104**, 115126 (2021).

[132] Schoonderwoerd, L., Pollmann, F. & Möller, G. Interaction-driven plateau transition between integer and fractional Chern Insulators. *arXiv preprint arXiv:1908.00988v2* (2022). 1908.00988v2.

[133] Fu, Q., Wang, P., Kartashov, Y. V., Konotop, V. V. & Ye, F. Nonlinear Thouless Pumping: Solitons and Transport Breakdown. *Physical Review Letters* **128**, 154101 (2022).

[134] Viebahn, K. *et al.* Interaction-induced charge pumping in a topological many-body system. *arXiv preprint arXiv:2308.03756* (2023). 2308.03756.

[135] Grusdt, F. & Höning, M. Realization of fractional Chern insulators in the thin-torus limit with ultracold bosons. *Physical Review A* **90**, 053623 (2014).

[136] Taddia, L. *et al.* Topological Fractional Pumping with Alkaline-Earth-Like Atoms in Synthetic Lattices. *Physical Review Letters* **118**, 230402 (2017).

[137] Zeng, T.-S., Zhu, W. & Sheng, D. N. Fractional charge pumping of interacting bosons in one-dimensional superlattice. *Physical Review B* **94**, 235139 (2016).

[138] Tao, R. & Thouless, D. J. Fractional quantization of Hall conductance. *Physical Review B* **28**, 1142–1144 (1983).

[139] Rezayi, E. H. & Haldane, F. D. M. Laughlin state on stretched and squeezed cylinders and edge excitations in the quantum Hall effect. *Physical Review B* **50**, 17199–17207 (1994).

[140] Bergholtz, E. J. & Karlhede, A. Quantum Hall system in Tao-Thouless limit. *Physical Review B* **77**, 155308 (2008).

[141] Maruo, S., Nakamura, O. & Kawata, S. Three-dimensional microfabrication with two-photon-absorbed photopolymerization. *Optics letters* **22**, 132–134 (1997).

[142] Deubel, M. *et al.* Direct laser writing of three-dimensional photonic-crystal templates for telecommunications. *Nature Materials* **3**, 444–447 (2004).

[143] Roques-Carmes, C. *et al.* A framework for scintillation in nanophotonics. *Science* **375**, eabm9293 (2022).

[144] Kurman, Y., Shultzman, A., Segal, O., Pick, A. & Kaminer, I. Photonic-Crystal Scintillators: Molding the Flow of Light to Enhance X-Ray and γ -Ray Detection. *Physical Review Letters* **125**, 040801 (2020).

[145] Kurman, Y. *et al.* Purcell-enhanced X-ray scintillation. *arXiv preprint arXiv:2302.01300* (2023). 2302.01300.

[146] Ródenas, A. *et al.* Three-dimensional femtosecond laser nanolithography of crystals. *Nature Photonics* **13**, 105–109 (2019).

[147] Paz-Buclatin, F. *et al.* Circularly symmetric nanopores in 3D femtosecond laser nanolithography with burst control and the role of energy dose. *Nanophotonics* **12**, 1511–1525 (2023).

[148] Stafe, M., Marcu, A. & Puscas, N. N. *Pulsed Laser Ablation of Solids: Basics, Theory and Applications*, vol. 53 (Springer Science & Business Media, 2013).

Vita

Marius Jürgensen

Education:

- Ph.D. in Physics (expected), Pennsylvania State University, 2019-2024
- M.Sc. in Condensed Matter Physics, Technical University of Munich, 2016-2018
- B.Sc. in Physics, University of Münster, 2012-2015

Publications:

- **M. Jürgensen**, S. Mukherjee, C. Jörg and M.C. Rechtsman, 'Quantized fractional Thouless pumping of solitons,' *Nature Physics*, **19**(3) 2023.
- **M. Jürgensen**, M.C. Rechtsman, 'Chern Number Governs Soliton Motion in Nonlinear Thouless Pumps,' *Phys. Rev. Lett.*, **128**(11) 2022.
- **M. Jürgensen**, S. Mukherjee, and M.C. Rechtsman, 'Quantized Nonlinear Thouless Pumping,' *Nature*, **596**(7870) 2021.
- A. Cerjan, **M. Jürgensen**, W.A. Benalcazar, S. Mukherjee and M.C. Rechtsman, Observation of a higher-order topological bound state in the continuum,' *Phys. Rev. Lett.*, **125**(21) 2020.
- M. Blauth, **M. Jürgensen**, G. Vest, O. Hartwig, M. Prechtl, J. Cerne, J.J. Finley and M. Kaniber, 'Coupling Single Photons from Discrete Quantum Emitters in WSe_2 to Lithographically Defined Plasmonic Slot Waveguides,' *Nano Letters*, **18**(11), 2018.
- M. Blauth, G. Vest, S.L. Rosemary, M. Prechtl, O. Hartwig, **M. Jürgensen**, M. Kaniber, A.V. Stier and J.J. Finley, 'Ultracompact Photodetection in Atomically Thin $MoSe_2$,' *ACS Photonics*, **6**(8), 2019.
- T. Stiehm, J. Kern, **M. Jürgensen**, S.M de Vasconcellos and R. Bratschitsch, 'Nanoantenna-controlled radiation pattern of the third-harmonic emission,' *Applied Physics B*, **122**, 1-6 2016.

Selected Awards:

- Physics Department Peter Eklund Award for Scientific Communication, Pennsylvania State University, 2023
- W. Donald Miller (2023, 2024), David C. Duncan (2022, 2023, 2024) and Downsbrough (2022, 2023, 2024) Graduate Fellowship, Pennsylvania State University
- Verne M. Willaman Distinguished Graduate Fellowship, Pennsylvania State University, 2019